Lasing effect in femtosecond filaments in air

Pengji Ding

NNT : 201XSACLS053

Thèse de doctorat de l'Université Paris-Saclay préparée L'École Polytechnique

Ecole doctorale n°572
École Doctorale Ondes et Matière
Spécialité de doctorat: Physique

par

M. Pengji Ding

Effet Laser dans Filaments Femtoseconde dans l'Air

Thèse présentée et soutenue à Le Laboratoire d'Optique Appliquée, le 13 Septembre 2016.

Composition du Jury :

M.	Arnaud COUAIRON	Prof. École Polytechnique	(Président du jury)
Mme.	Olga KOSAREVA	Prof. Moscow State University	(Rapporteur)
M.	Milutin KOVACEV	Prof. Leibniz Universitat Hannover	(Rapporteur)
M.	Cord ARNOLD	Conférencier Lund University	(Examinateur)
M.	Andre MYSYROWICZ	Prof. ENSTA-ParisTech	(Co-directeur de thèse)
M.	Yi LIU	Directeur de rechercher CNRS	(Directeur de thèse)

Acknowledgement

I am really grateful at this very moment when I realize that three years' study as a doctoral student is about to end. It has been a great experience to be a doctoral student of the famous Ecole Polytechnique and do research in the Laser-Matter Interaction (ILM) group in Laboratoire d'Optique Appliquée (LOA). I would like to sincerely thank everyone who help me in some way to this work, and in advance I apologize for anyone I might have forgotten to mention.

More than anyone, I owe all my gratitude to my supervisor Dr. Yi Liu, for providing me the opportunity to come over here and for numerous support in any kinds of measure throughout the past years. Since the very first day, you are very nice and always available to help me deal with personal things like titre de séjoure, housing, inscription and many paper works, only for example. You are very kind of sharing your vast experience and knowledge with me in discussion and teaching me many experimental skills from the beginning, which definitely can help me move forward after the PhD. I have learned lots of thing from you, not only the knowledge of optics and the ways how to do research, but also the importance of being realistic optimistic. Few time I have lost confidence on the experiment, but your patience and insistence makes it finally successful. This work would definitely haven't been possible without you. I deeply thank the China Scholarship Council (CSC) who has provided the funding for three years, supporting me to finish PhD without worries about expense.

I deeply thank my co-supervisor André Mysyrowicz, for many times' discussion on the experimental results and also on the manuscript writing of my thesis. Also, for few times your suggestions makes my presentation better in the rehearsal. I would also like to specially thanks to the director of the group, Dr. Aurélien Houard, for at first accepting me into the group and supporting my study in many ways afterwards. I thank sincerely to all the present members of the ILM group: Bernard Prade, Yves-Bernard André, Jérôme Carbonnel, Leonid Arantchouk, Vytautas Jukna, Chen Shiyou, and Chen Shihua. You have helped me in different ways, and it is a real pleasure to be with you all.

I also thank to all the previous members of the group: Sergey Mitryukovskiy, Guillaume Point, Amélie Jarnac, Johann Brelet. I miss you all !

I also thank deeply our collaborators who supports our progress in research. Arnaud Couairon, Eduardo Oliva and Vladimir Tikhonchuk, thank you for consistent support on numerical simulations regarding on explaining the experiment results, which was indispensable to the complete of our work and publications. I would also like to extend a special thanks to the merbers of Attosecond Physics Group in Lund University, particulatly: Samuel Bengtsson, Neven Ibrakovič, Cord Arnold, Anne L'Huillier, for their comprehensive support on experiment conduction and fruitful discussion.

Special thanks to my two referees Prof. Milutin Kovacev and Prof. Olga Kosareva, who have taken precious time to examine the manuscript of thesis and promised to come to the defense. I also warmly thank Cord Arnold and Arnaud Couairon for accepting the invitation of being the members of the jury in my defense.

In the laboratory, many people helped me in different ways. I thank Antoine Rousse, the director of LOA, and the secretaries for the great assistance on paper works, refunding and administration issues.

I am grateful to all the friends who I have met in past three years, particularly Yu Chao, Li Lu, Yang Renjun, and Li Zhujie. With you, the spare time after work becomes wonderful, especially I tasted a lots of delicious food. Particularly I appreciate my close friend Chao for the time we spent together, and I wish you got everything right on the way to being a doctor !

Finally, all my love goes to my dad and mom, my brother and sisters. I love you, and I miss you so much !

Abstract

Femtosecond laser filamentation in air is a phenomenon that involves a rich family of nonlinear optic effects. Lasing effect from filaments has emerged as a new phenomenon in 2011. It has been actively studied in recent 5 years not only because of its potential applications in remote sensing techniques but also the fruitful physics involved. This thesis is devoted to the study of two types of lasing effect from filament plasma generated by 800 nm femtosecond laser pulses in air or pure nitrogen. The first is the bidirectional amplified spontaneous emission at 337 nm wavelength of neutral nitrogen molecules, only enabled by circularly-polarized pulses. The population inversion mechanism is attributed to inelastic electron-molecule collisions between energetic electrons and neutral nitrogen molecules on the ground state. Full characterization of both forward and backward 337 nm lasing pulse is conducted. Particularly the temporal profile measurements is compared to numerical simulations based on one-dimensional Maxwell-Bloch equation, which turns out to be in good agreement.

Another type of lasing effect is related to excited nitrogen ion N_2^+, emitting at 391 nm and 428 nm wavelengths. This type of lasing effect can only be observed with linearly-polarized pump laser. It is systematically characterized in spatial, temporal and spectral domains. The temporal profile results prove that ionic lasing emission is fundamentally superradiance. A new mechanism, namely the electron recollision excitation process, is proposed for the achievement of population distribution in the upper level of transition. It is supported by two experimental measurements consisting of pump ellipticity dependence and pump wavelength dependence of 391 nm lasing intensity. Numerical simulations give good agreement with the experimental observation.

Keywords: filamentation, filament plasma, lasing effect, nitrogen molecule

Résumé court

La filamentation laser femtoseconde dans l'air est un phénomène qui implique un grand nombre d'effets optiques non linéaires. L'effet laser dans les filaments a émergé comme un phénomène nouveau en 2011. Il a été activement étudié au cours des cinq dernières années, non seulement en raison de ses applications potentielles dans les techniques de télédétection mais aussi pour la riche physique à son origine. Cette thèse est consacrée principalement à l'étude de deux types d'effets laser à partir du plasma filamentaire généré dans l'air ou l'azote par des impulsions laser femtoseconde à 800 nm. Le premier est l'émission spontanée amplifiée des molécules d'azote neutre à la longueur d'onde de 337 nm, qui est bidirectionnelle et activée uniquement par des impulsions polarisées circulairement. Le mécanisme d'inversion de population est attribué aux collisions inélastiques électrons-molécules entre les électrons énergiques et les molécules d'azote neutre dans l'état fondamental. La caractérisation complète de l'impulsion laser à 337 nm émise vers l'avant et vers l'arrière est réalisée. En particulier, les mesures de profil temporel sont comparées à des simulations numériques basées sur l'équation de Maxwell-Bloch à une dimension, qui se révèlent être en bon accord.

Un autre type d'effet laser est lié aux ions azote N_2^+, émettant à 391 nm et 428 nm. Ce type d'effet laser est observé avec une pompe laser polarisée linéairement. Il est caractérisé systématiquement dans le domaine spatial, temporel et spectral. Les mesures du profil temporel prouvent que l'émission laser ionique est un mécanisme de superradiance. Un nouveau mécanisme, à savoir le processus d'excitation par recollision d'électrons, est proposé pour expliquer la distribution de population dans le niveau supérieur de la transition. Il est conforté par deux mesures expérimentales consistant en la dépendance de l'émission laser à 391 nm à l'ellipticité et la dépendance à longueur d'onde du laser de pompe. Des simulations numériques sont en bon accord avec les observations expérimentales.

Mots clefs: filamentation, plasma filamentaire, effet laser, molécule d'azote

Résumé long

La filamentation laser femtoseconde est un phénomène d'optique non-linéaire fascinant. Elle se produit lorsqu'un faisceau laser femtoseconde intense se propage dans un milieu transparent et que sa puissance crête dépasse une valeur critique (environ 5 Gigawatts dans l'air). A une telle puissance, le faisceau laser s'auto-focalise et s'effondre sur lui-même en raison de l'effet Kerr optique jusqu'à ce qu'il soit arrêté par l'ionisation multiphotonique. La compétition dynamique entre ces deux effets lors de la propagation du faisceau donne finalement naissance à une longue colonne de plasma très mince que l'on appelle filament. La première partie de cette thèse présente brièvement les mécanismes physiques responsables de la filamentation laser dans les gaz au Chapitre 1 et plusieurs effets non-linéaires remarquables liés à la filamentation, tels que l'élargissement spectral, l'émission conique, l'alignement moléculaire induit par l'effet Raman-Kerr et l'effet laser. L'effet laser dans la filamentation laser femtoseconde est un phénomène fascinant, non seulement en raison de ses applications potentielles dans le domaine de la télédétection, mais aussi pour la riche physique à son origine. Il a été intensément étudié au cours des cinq dernières années, depuis qu'il a été observé que la colonne de plasma filamentaire pouvait donner lieu à une émission stimulée. Cette thèse se consacre à l'étude expérimentale et théorique de deux types d'effets laser liés à l'azote moléculaire dans le filament femtoseconde.

1. 337 nm effet laser des molécules neutres d'azote dans les filaments femtoseconde

Le premier type d'effet de laser est l'émission laser à 337 nm des molécules d'azote neutres excitées dans la seconde bande négative, $C^3\Pi_u^+(v' = 0) \rightarrow B^3\Pi_g^+(v = 0)$, où v désigne le niveau vibratoire de chaque état électronique. Il est décrit dans la deuxième partie de cette thèse, du Chapitre 2 au Chapitre 4. L'effet laser à 337 nm a été observé pour la première fois dans notre laboratoire en 2014. Dans les expériences, les impulsions laser infrarouge (800 nm, 45 fs) ont été focalisées dans l'azote pour créer un filament

de plasma de quelques centimètres de long, et un photomultiplicateur combiné avec un monochromateur ont été utilisés pour détecter l'émission vers l'arrière. Nous avons utilisé une lame quart d'onde pour changer l'état de polarisation de l'impulsion laser de pompe. Avec des impulsions laser de pompage linéairement polarisées, nous avons détecté les raies de fluorescence typiques de la seconde bande négative de la molécule d'azote neutre. Lorsque l'état de polarisation a été changé de linéaire à circulaire, l'intensité d'émission à 337 nm longueur d'onde a augmenté de façon spectaculaire, par un facteur 10. Cet effet d'émission à 337 nm des molécules neutres d'azote se produit simultanément dans les directions avant et arrière mais la propagation de l'excitation avec l'impulsion laser de pompage induit une émission de rayonnement laser beaucoup plus forte dans la direction avant que dans la direction arrière.

Nous avons effectué des caractérisations systématiques de l'émission laser en mesurant le spectre, le profil spatial, la forme temporelle de l'onde, la divergence du faisceau laser, la polarisation, la dépendance à l'énergie de la pompe, à la pression d'azote et à la polarisation du laser de pompe. L'une des caractéristiques principales de l'émission de laser à 337 nm est que l'intensité de l'effet laser dans la direction avant est 3 ordres de grandeur plus importante que vers l'arrière. Le spectre de l'émission laser à 337 nm montre une largeur de raie plus étroite que la fluorescence. Le faisceau laser à 337 nm vers l'avant présente un profil en anneau, mais vers l'arrière, il présente une distribution avec un maximum au centre. Les deux ont une faible divergence d'environ 10 mrad. La mesure de la polarisation de l'émission laser montre qu'elle est non polarisée, ce qui indique que ce type d'émission stimulée est de type ASE. Pour les ASE avant et arrière à 337 nm, on mesure un seuil sur l'énergie de la pompe d'environ 4 mJ avec une longueur focale de 1 m. Il est intéressant de mentionner que l'intensité du laser augmente avec la pression de gaz d'azote entre 0.4 bar et notre pression maximum de 2.0 bars. On peut donc s'attendre à une intensité laser plus importante avec une pression plus élevée. Le profil temporel de l'impulsion ASE vers l'avant a été mesuré par une méthode de corrélation croisée tandis que celui de l'émission vers l'arrière a été estimé façon indirecte, par une méthode d'interférométrie. L'ASE vers l'avant à 337 nm a une durée d'impulsion (FWHM) d'environ 10 ps tandis que l'ASE vers arrière a une durée beaucoup plus longue de presque 85 ps avec une pression d'azote de 1 bar et une énergie laser de pompe de 10 mJ.

L'émission laser vers l'arrière à 337 nm est particulièrement intéressante en raison de son application potentielle dans la télédétection atmosphérique. Malheureusement, l'effet d'attachement sur les molécules d'oxygène conduit à une émission laser à 377 nm beaucoup plus faible dans l'air que dans l'azote pur, d'un facteur 200. Ainsi, dans l'air ambiant l'émission laser vers l'arrière à 337 nm n'a pas encore été observée. Pour obtenir

une source d'émission cohérente à 337 nm dans l'air atmosphérique, il est alors nécessaire d'avoir une densité d'inversion de population plus élevée pour surmonter l'effet des molécules d'oxygène. Une approche possible pour atteindre cet objectif est d'utiliser un puissant laser de pompe avec une grande longueur d'onde. Une autre approche consiste à utiliser d'abord un puissant laser de pompe de durée nanoseconde pour dissocier les molécules d'oxygène, puis d'envoyer une seconde impulsion laser à 800 nm polarisée circulairement pour générer une émission laser à 337 nm vers l'arrière.

On peut obtenir une émission laser à 337 nm amplifiée de façon spectaculaire en utilisant à la fois une impulsion d'injection de faible énergie et un gain optique. Cet effet laser injecté est présenté au Chapitre 3. Pour les profils spatiaux, le faisceau laser à 337 nm injecté vers l'avant a une forme en anneau semblable à celui de l'ASE vers l'avant alors que le faisceau laser émis vers l'arrière présente un maximum central. Concernant sa polarisation, l'émission laser à 337 nm l'hérite de l'impulsion injectée. En injectant une impulsion de faible énergie dont on fait varier le retard par rapport à l'impulsion pompe nous avons étudié la dynamique du gain à 337 nm à différentes pressions d'azote. On observe une croissance du gain ultra-rapide et une décroissance relativement lente. Le temps de montée du gain est d'environ 4 ps et le temps de décroissance d'environ 20 ps pour une pression de 1 bar. Le temps de montée du gain diminue lorsqu'on augmente la pression du gaz, indiquant qu'une excitation de type collisionnelle est à l'origine de l'inversion de population. A partir de la durée de vie de gain, nous avons calculé la longueur de gain effective, qui est en fait beaucoup plus courte que la longueur géométrique du plasma de filament. Pour une pression de gaz d'azote de 1 bar avec une focale de 1 m, la durée de vie du gain est de 15 ps ce qui correspond à une longueur de gain effective de 4,5 mm tandis que le plasma du filament mesure 6 cm de long. A partir de la longueur d'amplification de 4,5 mm et du facteur d'amplification, on peut calculer le coefficient de gain qui vaut alors 11,8 par centimètre dans le régime de gain à faible signal.

Le profil temporel de l'émission laser à 337 nm injectée se compose de l'injection et d'une impulsion de sillage, qui présente structures périodiques que l'on attribue à des effets de battements quantiques. Leur période est d'environ 11 ps. De manière surprenante, l'impulsion de sillage de l'impulsion laser à 337 nm injectée vers l'arrière présente une modulation temporelle plus importante que dans le cas de l'émission injectée vers l'avant. En outre, elle dure plus de 100 ps. L'injection d'une impulsion externe consiste seulement à polariser le milieu de gain, créant une polarisation macroscopique, ce qui conduit à une impulsion de sillage suivant l'impulsion injectée. Concernant les structures périodiques, il a été montré dans le cas du laser traditionnel à azote pompé par décharge que la raie laser à 337 nm est composée de trois branches finement séparées en raison de l'interaction entre les moments angulaires orbitaux et le spin. Le processus

d'excitation rapide par collision amène les molécules d'azote dans une superposition cohérente des trois branches. Ainsi, une modulation d'intensité dans le domaine temporel est alors produite en raison d'un phénomène de battements quantiques entre ces branches. La séparation entre ces fines branches est de 0.033 nm, correspondant à une période de battement de 11.5 ps. Elle est donc en bon accord avec nos observations expérimentales.

Le mécanisme sous-jacent d'inversion de population pour l'émission stimulée à 337 nm des molécules d'azote neutres dans le plasma filamentaire peut être attribué au processus inélastique d'excitation par collision électron-molécule car l'ellipticité du laser de pompe joue un rôle clé. Il a été montré dans la littérature que la répartition des énergies cinétiques des électrons nés dans le champ laser intense dépend fortement de la polarisation du laser de pompage. Avec un laser de pompe à polarisation linéaire, les électrons libres sont accélérés de haut en bas le long de la direction de polarisation du laser à chaque cycle optique. Ainsi, à la fin de l'impulsion la plupart ont une faible énergie cinétique, dont la distribution ne s'étendant que jusqu'à quelques eV. Pour le laser de pompe à polarisation circulaire, les électrons sont constamment accélérés loin du noyau ionique. La distribution électronique finale est alors presque mono-cinétique avec un pic correspondant à deux fois l'énergie ponderomotrice U_p. Ces observations nous guident vers un autre mécanisme pour expliquer la transition d'excitation de l'état fondamental à l'état $C^3\Pi_u^+$ supérieur via le processus de collision inélastique électron-molécule $N_2(X^1\Sigma_g^+) + e = N_2(C^3\Pi_u^+) + e$. Il explique naturellement l'observation expérimentale de la dépendance à la pression de la dynamique du gain. C'est en fait la principale réaction responsable de l'inversion de population dans un laser à azote traditionnel, où les électrons sont accélérés pour obtenir une énergie suffisante par le champ électrique de décharge. La section efficace de cette réaction dépend fortement de l'énergie cinétique de l'électron incident. Elle est proche de zéro pour les énergies électroniques inférieures à l'énergie cinétique de seuil (12 eV), présente un pic de résonance autour de 14.5 eV, puis décroît progressivement pour les énergies supérieures. Pour confirmer ce mécanisme, des simulations numériques ont été réalisées pour simuler la distribution en énergie des électrons dans le plasma filamentaire, en tenant compte de nos conditions expérimentales. Les résultats montrent que c'est avec une polarisation laser circulaire que le plus grand nombre d'électrons avec une énergie cinétique approchant le double de l'énergie ponderomotrice sont produits.

Pour comprendre cet effet laser à l'intérieur du plasma de filaments, des simulations numériques de la dynamique temporelle de l'effet laser à 337 nm ont été réalisées sur la base d'un modèle de Maxwell-Bloch à une dimension et dépendant du temps. Avec ce modèle, on peut simuler numériquement la dynamique des gains optiques, ce qui correspond bien à l'observation expérimentale. L'ASE vers l'avant démarre à partir d'une émission spontanée produite pendant toute la durée de gain, en raison de la longue durée

de vie du niveau supérieur de la transition. Les effets d'amplification et de saturation raccourcissent sa durée. Après avoir traversé le plasma filamentaire, l'impulsion ASE a une durée (FWHM) de 44 ps, ce qui est en accord avec nos observations. Dans le cas de l'injection externe, l'évolution de la structure temporelle de l'impulsion injectée est principalement due à son profil spectral initial, lié à sa durée et à la largeur spectrale de la transition, dominée par les collisions. Le décalage entre la largeur spectrale de l'impulsion injectée et celle de la transition déclenche la création pendant le premier centimètre et l'amplification subséquente d'une impulsion de sillage retardée. Lorsque le sillage est suffisamment intense, les effets de saturation réduisent sa durée jusqu'à ce qu'il atteigne la valeur de 4.5 ps (FWHM) après la propagation à travers un plasma de 3 cm de long, en accord avec les résultats de l'expérience. Concernant l'évolution temporelle de l'impulsion descendante injectée, la simulation prédit une impulsion injectée modérément amplifiée, suivie d'un rayonnement de sillage durant plus de 60 ps, en bon accord avec nos observations expérimentales. L'émission ASE arrière à 337 nm est beaucoup plus faible que dans le cas vers l'avant. Ceci est dû à la géométrie particulière du pompage longitudinal. Lorsque les photons d'émission spontanée se propagent dans la même direction que le faisceau de la pompe IR, ils interagissent en continu avec une inversion de population nouvellement créée. Au contraire, dans le cas de l'ASE vers l'arrière, où l'ASE se propage dans la direction inverse de la pompe infrarouge, l'inversion de population rencontrée par le photon d'émission spontanée est épuisée progressivement par l'ASE avant qui suit l'impulsion de la pompe IR. La durée d'impulsion simulée de l'ASE arrière est de 77 ps, en bon accord avec la mesure d'autocorrélation. Pour conclure, les simulations numériques basées sur l'équation de Maxwell-Bloch non adiabatique concordent bien avec les résultats expérimentaux. Ils révèlent que la différence entre l'émission avant et arrière provient du schéma d'excitation itinérante du laser de pompage et de la durée de vie limitée du gain optique. Ces résultats fournissent des informations temporelles précieuses concernant le rayonnement à 337 nm du plasma d'azote gazeux pompé par des impulsions laser femtoseconde à 800 nm à polarisation circulaire, qui peuvent trouver d'importantes applications de spectroscopie laser à distance dans l'atmosphère.

2. Superradiation des ions azote dans les filaments femtoseconde dans l'air

Un autre type d'effet laser est lié aux molécules d'azote ionisées une fois dans les filaments femtoseconde. Dans le Chapitre 5 au Chapitre 6, les émissions d'ions ioniques aux longueurs d'onde de 391 nm et de 428 nm seront présentées. Ces deux émissions correspondent aux transitions $B^2\Sigma_u^+(\nu = 0) \rightarrow X^2\Sigma_g^+(\nu' = 0, 1)$ de la première bande négative de la molécule d'azote ionisée, où ν et ν' désigne le niveau vibratoire de chaque

état électronique. On mettra l'accent sur l'étude de l'émission laser de 391 nm car, sous de nombreux aspects, l'émission laser de 428 nm possède des caractéristiques tout à fait semblables à l'émission de laser à 391 nm. Les émissions laser à 391 nm ont été expérimentalement caractérisées par la mesure des spectres, du profil spatial et de la divergence, du profil temporel, du seuil d'énergie de la pompe, de la dépendance à la pression gazeuse et de la dépendance à l'ellipticité du laser pompe. L'émission laser à 391 nm est normalement générée à basse pression de gaz, dans une plage qui dépend de l'énergie de l'impulsion de la pompe et de la géométrie de focalisation. Son spectre est composé de deux branches, la branche R et la branche P. Le seuil d'énergie de la pompe à 391 nm pour l'émission laser a été mesuré à 1 mJ dans le cas d'une impulsion laser de pompe à 800 nm et de 45 fs de durée d'impulsion. Concernant le profil spatial, le faisceau laser à 391 nm présente un mode annulaire avec un maximum central alors que le faisceau laser à 428 nm présente un mode annulaire pur. La mesure des deux émissions laser en fonction de l'ellipticité du laser de pompe montre une forte dépendance à l'ellipticité, très similaire à la génération d'harmoniques d'ordre élevé.

Dans les deux sens avant et arrière, l'injection d'une impulsion externe peut générer une forte émission laser à 391 nm. Comparé à celui vers l'avant, le rayonnement à 391 nm émis vers l'arrière est plus faible et nécessite une énergie de pompage plus élevée. La direction de polarisation de l'émission laser émise à 391 nm est comprise entre les directions de polarisation des impulsions d'injection et de pompage au fur et à mesure que l'impulsion injectée est changée de parallèle à perpendiculaire à l'impulsion de pompage. Dans la configuration d'injection externe, nous avons mesuré la dynamique de gain de l'émission laser à 391 nm. Elle montre un temps de montée du gain ultra-rapide d'environ 300 fs, qui est indépendant de l'intensité de l'injection, de la pression du gaz et de l'énergie de l'impulsion de pompe. Pour le processus de décroissance du gain, cela dépend de la pression dans le sens que des pressions plus élevées conduisent à une décroissance plus rapide.

Dans la gamme de pressions allant de très basse pression à la pression optimale pour l'effet laser, les mesures d'évolution temporelle de l'impulsion laser à 391 nm avec une pression croissante rappellent les caractéristiques de la superradiance. Pour chaque résultat obtenu à une certaine pression, l'intensité du pic, la largeur d'impulsion et le retard relatif sont extraits et représentés graphiquement en fonction de la pression d'azote. Le résultat correspond bien à la prédiction d'un mécanisme de superradiance. En effet, le temps de décroissance et la largeur d'impulsion de l'impulsion laser sont inversement proportionnels à la pression d'azote alors que son intensité de pic est proportionnelle au carré de la pression d'azote. Par conséquent, cette impulsion à 391 nm est fondamentalement un effet de superradiance. En outre, il a été rapporté dans la littérature que la largeur de l'impulsion laser à 391 nm était inversement proportionnelle à la longueur du filament,

ce qui est également en accord avec la superradiance. Un autre indice de superradiance a été obtenu dans la configuration d'injection externe. On mesure l'intensité d'émission à 391 nm en fonction du retard entre deux impulsions d'injection successives. Le retard relatif entre les deux impulsions injectées est d'environ 2 ps et il a été varié autour de cette valeur avec une précision de 40 attosecondes. Le signal final à 391 nm montre une forte oscillation avec une période de 1.3 fs, ce qui correspond à la période d'émission à 391 nm. Ce résultat peut seulement être bien expliqué dans le cadre de la superradiance. L'impulsion laser pompe à 800 nm crée le plasma filamentaire et prépare le milieu de gain. L'injection de la première impulsion d'injection a déclenché l'accumulation de polarisation macroscopique dans le milieu de gain, conduisant à une superradiance. Ensuite, l'interaction entre la polarisation macroscopique et la seconde impulsion injectée retardée doit être un processus dépendant de la phase. En conséquence, on peut s'attendre à une augmentation ou une réduction de l'émission à 391 nm dépendant de la phase. En se basant sur les trois preuves précédemment décrites, on peut raisonnablement conclure que l'émission laser à 391 nm est le fruit d'un mécanisme de superradiance.

La superradiance est généralement décrite comme la décroissance spontanée et coopérative d'un ensemble d'atomes ou de molécules inversés, et qu'elle nécessite donc habituellement une inversion de population. Par conséquent, il est nécessaire et important de clarifier l'origine du gain optique pour la superradiance à 391 nm. Naturellement, plusieurs publications ont proposé qu'il existe une inversion de population entre l'état fondamental et l'état excité. Il a été rapporté que l'inversion de population peut être construite à travers l'échange de population entre l'état $X^2\Sigma_g^+$ de l'état fondamental et les états $A^2\Pi_u$ et $B^2\Sigma_u^+$ excités. Dans cette considération théorique, la population se répartit principalement dans l'état fondamental après l'ionisation. Les champs laser suivants provoquent un transfert de population entre l'état fondamental et les deux états excités par un processus d'oscillation de Rabi. A la fin du champ laser, la population dans l'état $A^2\Pi_u$ est significativement augmentée tandis que celle dans l'état $X^2\Sigma_g^+$ est fortement diminuée. En conséquence, la population finale dans l'état $B^2\Sigma_u^+$ peut devenir plus grande que celle dans l'état $X^2\Sigma_g^+$ du niveau fondamental. Cependant, un rapport de conférence très récent utilisant la technologie fs-CARS montre qu'il n'y a pas de répartition observable de la population dans l'état $A^2\Pi_u$ alors que dans les états $X^2\Sigma_g^+$ et $B^2\Sigma_u^+$ sont observés. Ce résultat met en cause l'existence de l'inversion de population.

Une autre explication a été proposée récemment concernant le mécanisme de gain de l'émission ionique laser, en termes d'alignement rotationnel transitoire du sol et d'états excités menant au gain optique en l'absence d'inversion de population. Cependant, cette explication ne permet pas d'expliquer la caractéristique principale de la mesure de la dynamique du gain de l'émission laser à 391 nm pompée par des impulsions laser à 800 nm. La dynamique de gain mesurée montre une accumulation ultra-rapide et une

décroissance relativement lente sur des dizaines de picosecondes qui dépend des conditions expérimentales. Cependant, l'hypothèse ci-dessus ne prévoyait qu'une série de fenêtre temporelle étroite (<1 ps) pour le gain optique. Par ailleurs, il faut souligner que l'alignement moléculaire joue un rôle significatif pour ce laser à 391 nm, puisque la signature de l'alignement des molécules est observée à la fois dans la dynamique des gains et dans le profil temporel de l'émission. Cependant, ce n'est pas le facteur essentiel permettant le gain optique. En ce moment, l'explication de l'origine du gain optique reste très controversée.

Suite au fait que l'émission laser à 391 nm montre une dépendance à l'ellipticité de l'impulsion laser de pompage similaire à une génération harmonique d'ordre élevé, un nouveau mécanisme a été proposé dans cette thèse pour la répartition de la population au niveau supérieur. La génération d'harmoniques d'ordre élevé a été bien comprise avec le modèle de recollision semi-classique. En appliquant le même modèle semi-classique à l'effet de laser à 391 nm, la dépendance à l'ellipticité de l'émission laser est interprétée comme étant due à un transfert non radiatif de la population d'ions de l'état $X^2\Sigma_g^+$ à l'état $B^2\Sigma_u^+$ par recollision électronique induite par le laser. Ce modèle peut être brièvement abordé comme suit: Lors de chaque événement élémentaire, un électron en présence du laser de pompe intense est retiré de l'orbite externe de la molécule d'azote neutre, accéléré, puis repoussé par le champ laser vers l'ion parent où il entre en collision inélastique avec un électron orbital interne. Au cours de cet événement, si l'électron d'impact a une énergie suffisante au-dessus de l'énergie d'excitation, il ya une probabilité de transférer l'électron orbital interne à l'orbite externe de l'ion moléculaire. Un électron libre et un ion moléculaire excité sont laissés après l'événement.

Sur la base du modèle ci-dessus, des calculs quantitatifs ont été effectués sur la dépendance de la probabilité d'excitation totale de 391 nm de transition laser à la longueur d'onde du laser de pompage. Tout d'abord, la probabilité d'excitation totale à la longueur d'onde de résonance à 782 nm (deux fois 391 nm) est nulle. Ceci est attendu puisque les probabilités d'excitation par des événements de recollision des côtés opposés s'annulent exactement dans le cas de la longueur d'onde de résonance. Ce résultat est analogue au fait qu'on ne peut pas produire d'harmoniques paires dans un milieu gazeux. Plus important encore, la probabilité d'excitation totale montre une dépendance périodique à la longueur d'onde de la pompe, et cette période dépend de la durée. Afin de confirmer expérimentalement les résultats de simulation et donc le mécanisme d'excitation de recollision, une campagne expérimentale a été menée à l'Université de Lund pour étudier la dépendance de l'émission laser à 391 nm à la longueur d'onde du laser de pompage. Les résultats de l'expérience sont en bon accord avec les résultats de la simulation. Tout d'abord, il est clairement noté qu'aucune émission laser à 391 nm ne peut être détectée lorsque la longueur d'onde centrale est autour de 782 nm, ce qui

concorde remarquablement avec la prédiction théorique. Deuxièmement, l'émission laser à 391 nm montre une dépendance périodique à la longueur d'onde centrale de l'impulsion laser de pompage. Avec une longueur d'onde centrale plus grande, la période devient plus courte. En conclusion, l'expérience et les résultats de la simulation confirment bien que le processus d'excitation par recollision fournit la distribution de la population de molécules d'azote au niveau supérieur de la transition à 391 nm, qui est essentielle à l'ionisation ionique d'azote dans les filaments femtoseconde.

Cependant, le niveau attendu d'excitation est relativement faible, de l'ordre de 1%, ce qui est insuffisant pour l'inversion de population. Pour avoir une explication complète de l'origine de la superradiance à 391 nm, nous avons proposé un effet de laser sans inversion de population (LWI) basé sur le modèle de recollision électronique. A savoir, la transition $A^2\Pi_u \rightarrow X^2\Sigma_g^+$, qui correspond à la longueur d'onde proche de la longueur d'onde du laser de pompage, est excitée de façon radiative par l'impulsion laser de pompe. En présence d'une faible quantité de molécules d'azote dans l'état supérieur obtenue par un processus de recollision électronique, l'interférence quantique entre les transitions $B^2\Sigma_u^+ \rightarrow X^2\Sigma_g^+$ et $A^2\Pi_u \rightarrow X^2\Sigma_g^+$ conduit à la génération d'un effet laser à 391 nm. Pour valider cette théorie, des études expérimentales et des simulations numériques seront nécessaires.

Preface

Femtosecond laser filamentation is an interesting nonlinear optical phenomenon. It occurs when an intense femtosecond laser beam propagates in a transparent medium and its peak power exceeds a critical value, approximately 5 Gigawatts in air for example. At such high power, the laser beam self-focuses and collapses due to the optical Kerr effect until arrested by multiphoton ionization that leads to a defocusing plasma. The dynamic competition between these two counterpart effects along the propagation of the laser beam finally gives rise to a very thin and long plasma column or filament as we call it afterwards. The first part of this thesis is dedicated to briefly introduce the basic principles regarding on laser filamentation in gas medium in Chapter 1, and several nonlinear effects that are related to the main part of this thesis, such as spectral broadening, conical emission, molecular alignment induced by Raman-Kerr effect and lasing effect. Lasing effect from femtosecond laser filamentation is a fascinating phenomenon, not only because of its potential applications in remote sensing techniques but also fruitful physics to discover. It has been intensively studied in recent few years since it was observed that the filamentary plasma column in gas medium can give rise to stimulated emission.

The author's work was mainly devoted to the nitrogen lasing effect from femtosecond laser filamentation in pure nitrogen or air. It has been categorized to two types. The first type of lasing effect is 337 nm lasing effect of the excited neutral nitrogen molecules in second negative band, from $C^3\Pi_u^+(\upsilon' = 0)$ to $B^3\Pi_g^+(\upsilon = 0)$, where υ denotes the vibrational level at each electronic state. It consists of second part of this thesis, from Chapter 2 to Chapter 4. The 337 nm lasing emission was first observed in our laboratory at one fortunate night in 2014. In experiments, the infrared laser pulses (800 nm, 45 fs) were focused into nitrogen to create a few-centimeters-long filament plasma, and a photon multiplier tube (PMT) combined with a monochromator was used to detect backward emission. When the polarization state of the pump pulse was changed from linear to circular, the 337 nm signal increased dramatically by tens of times. Afterwards, the forward 337 nm lasing emission was also found, and the lasing intensities in both directions were optimized further by different means. The backward lasing is particularly interesting because of its potentials for atmospheric remote sensing techniques. In

Chapter 2, the research background, including the study history of lasing effect from filament plasma and the idea that how can the backward lasing be employed in remote sensing, will be first introduced. The full characterization of both the forward and backward 337 nm lasing pulse will be shown in details, which includes the measurements of spectra, spatial profile, temporal waveform, beam divergence, polarization state, and also its dependences on pump energy, nitrogen pressure and pump pulse polarization, and etc.

The studies of 337 nm lasing effect in the external-seeding configuration will be shown in Chapter 3. By injecting a week seed pulse centered at 337 nm wavelength, the 337 nm lasing intensity can be significantly enhanced in both directions. The gain dynamics of 337 nm lasing is also studied, from which the effective gain length and therefore the gain coefficient can be calculated. The temporal profile measurements of seeded 337 nm lasing pulse gives an interesting result, i.e. it consists of the seed and a following wake pulse that composes of periodic structures due to quantum beats effect.

In Chapter 4, the physics explanation why the 337 nm lasing is possible will be given. We attribute the population inversion in corresponding transition, which results in 337 nm lasing emission, to inelastic collisions between the electrons liberated by the circular pump pulse and surrounding neutral nitrogen molecules on the ground state. Regarding particularly on the temporal evolution of 337 nm lasing emission, numerical simulations based on one-dimensional non-adiabatic Maxwell-Bloch equation will be presented, which turns out to be in good agreement with the experiment results.

Another type of lasing effect is related to excited nitrogen ion N_2^+. In Chapter 5, the ionic lasing emissions at 391 nm and 428 nm wavelengths in filament plasma will be presented. These two emissions belongs to the transition $B^2\Sigma_u^+(\nu = 0) \rightarrow X^2\Sigma_g^+(\nu' = 0, 1)$ of the first negative band of singly ionized nitrogen molecule. The emphasize will be put on studying the 391 nm lasing emission because in many aspects the 428 nm lasing emission possesses quite similar features with 391 nm lasing emission. The properties of 391 nm lasing emission will be shown through measuring its spectra, spatial profile, divergence, temporal waveforms and so on, like what have been done for 337 nm lasing effect. For instance, the 391 nm lasing emission is normally generated at very low gas pressure under our experimental conditions while 428 nm lasing emission is generated at rather high gas pressure. The gain dynamics shows a ultrafast gain buildup time less than 300 fs, which is independent of the seed intensity, gas pressure and also pump pulse energy. This type of lasing effect can only be observed with linearly-polarized pump laser, resulting from a sensitive dependence on pump ellipticity similar to high-order harmonic generation (HHG).

The interpretation and discussion on the origin of ionic lasing emissions will be given in Chapter 6. A new mechanism, namely the electron recollision excitation process, will be proposed for the achievement of population distribution in the upper level of transition. It is supported by two experimental measurements consisting of pump ellipticity dependence and pump wavelength dependence of 391 nm lasing intensity. Numerical simulations give good agreement with the experimental observation. In this chapter, ionic lasing emission is fundamentally superradiance which will be confirmed through three independent experiments, indicating that there exists macroscopic polarization of the aforementioned transition. Superradiance requires the presence of optical gain, which is normally achieved by population inversion. However, the recollision process seems not enough providing the gain for superradiance. Hence, another additional mechanism, i.e., lasing without inversion (LWI), will be proposed and discussed based on several experimental observations. To further solidify it, there needs more evidences and efforts in both experiment and theory.

Contents

Abbreviations

ASE	**A**mplified **S**pontaneous **E**mission
CPA	**C**hirped **P**ulse **A**mplification
CSC	**C**hina **S**cholarship **C**ouncil
EUV	**E**xtreme **U**ltra**v**iolet
FFT	**F**ast **F**ourier **T**ransformation
fs-CARS	femtosecond time-resolved **C**oherent **A**nti-Stoke **R**aman **S**cattering
FWHM	**F**ull **W**idth at **H**alf **M**aximum
FWM	**F**our-**W**ave **M**ixing
HHG	**H**igh-order **H**armonic **G**eneration
HWP	**H**alf **W**ave **P**late
iCCD	**i**ntensified **C**harge **C**oupled **C**amera
IR	**I**n**f**rared
LIDAR	**Li**ght **D**etection **A**nd **R**anging
LWI	**L**asing **W**ithout **I**nversion
MO-ADK	Tunnel ionization model for **Mo**lecule proposed by **A**mmosov M. V., **D**elone N. B., and **K**rainov V. P.
NSDI	**N**on-**S**equential **D**ouble **I**onization
PMT	**P**hoto**m**ultiplier **T**ube
MO-PPT	Photoionization model for **Mo**lecule proposed by **P**opov, **P**erelomov, and **T**erent'ev
SF	**S**uper**f**luorescence
SFG	**S**um **F**requency **G**eneration
SI	The **I**nternational **S**ystem of Units
SPM	**S**elf-**P**hase **M**odulation
SR	**S**uper**r**adiance
TEM	**T**ransverse **E**lectromagnetic **M**odes
TDL	**T**ime **D**elay **L**ine
TW	**T**era**W**att (10^{12} watts)
UV	**U**ltra**v**iolet
XPM	**C**ross-**P**hase **M**odulation
XUV	**X**-ray **U**ltra**v**iolet

Part I

Femtosecond Laser Filamentation In Gas Medium

Chapter 1

Femtosecond Laser Filamentation In Gas Medium

Contents

1.1 A brief introduction of femtosecond laser filamentation

This chapter aims to briefly introduce the fundamental physics and several important aspects of femtosecond laser filamentation in transparent nonlinear and dispersive media, particularly in gas medium. In biology, the term "filamentation" is the anomalous growth of certain bacteria in which cells continue to elongate but do not divide. In nonlinear optics, however, it refers to a dynamic process of nonlinear propagation of a laser pulse, in which an intense core of high intensity extends over distance much longer than the typical Rayleigh length. The laser intensity inside the core can reach $10^{13} - 10^{14}\ W/cm^2$ that is sufficient to ionize the molecules or atoms of the medium. The term "*filament*" is then used to describe a column of weakly ionized plasma in the wake of propagation of the laser pulse.

Femtosecond laser filamentation has became an intensive research field in past 20 years, as presented in the review papers by A. Couairon and A. Mysyrowicz [1] and others [2]. It was previously believed that intense ultrashort laser pulses can not propagate for a long range in atmosphere due to the combined effect of beam diffraction and group velocity dispersion. In 1995, however, Braun *et al.* performed a propagation experiment by using an intense infrared (IR) femtosecond pulse and found that the pulse intensity increased instead of decreasing [3] after tens of meters. This type of nonlinear propagation was termed filamentation or self-guided propagation. Sooner, femtosecond laser filamentation in air was demonstrated to reach more than 50 m in Laboratoire d'Optique Appliquée [4] (see Fig. 1.1) and then over hundreds of meters [5]. The distance was further extended to longer than 2 km in experiments performed by our group in École Polytechnique in 2003 [6]. Experiments of powerful femtosecond laser filamentation in the sky reported even longer distances of more than 20 km using a 2-m imaging astronomical telescope [7].

The formation of filaments can be mainly ascribed to two nonlinear effects: the optical Kerr effect and defocusing effect of the generated plasma. The former acts against diffraction and tends to focus the beam on itself. On contrary, the ensuing ionization-induced plasma reduces the local refractive index of the medium and therefore leads to beam defocusing. In the following, these two effects will be briefly introduced as well as other physical effects that play a role in femtosecond laser filamentation in gas medium.

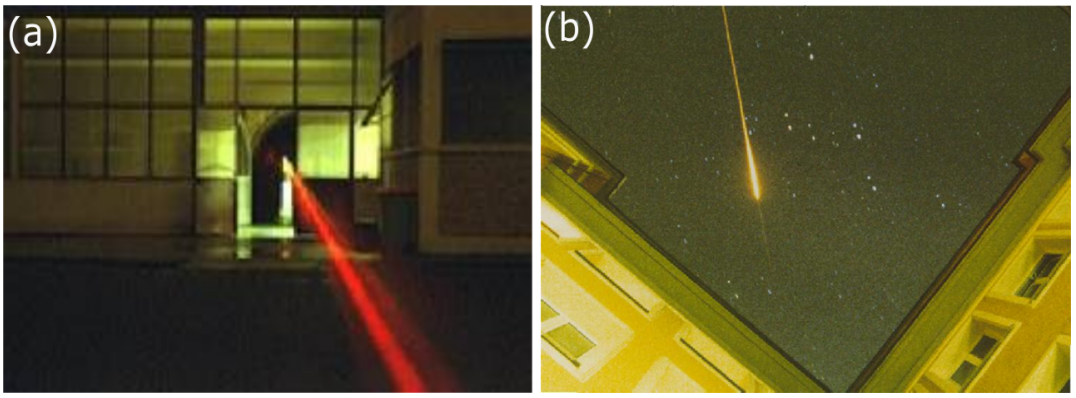

Figure 1.1: (a) Propagation of an 800 nm laser beam in atmosphere in the Laboratoire d'Optique Appliquée (École Polytechnique, Palaiseau). (b) Self-guided propagation the Teramobile laser beam in the sky. Courtesy to the Teramobile project (see the official website of Teramobile project).

1.2 Principle of femtosecond laser filamentation

1.2.1 Self-focusing of intense laser beam

The refractive index of a medium in the presence of an intense optical field can be described as

$$n = n_0 + n_2 I, \tag{1.1}$$

where n_0 represents the linear refractive index, n_2 represents the second-order index of refraction and I denotes the time-averaged intensity of the optical field. The change in refractive index described by above equation is normally called the optical Kerr effect, an analogy with the traditional Kerr electro-optic effect, in which the refractive index of a material changes quadratically with the strength of an applied static electric field. In this circumstance, n_2 is called the coefficient of the nonlinear Kerr index. The coefficient n_2 is related to the third order susceptibility $\chi^{(3)}$ through $n_2 = 3\chi^{(3)}/4n_0^2\epsilon_0 c$ where ϵ_0 denotes the permittivity of vacuum. The coefficient n_2 is usually positive, and thus leads to an increase of the refractive index in the presence of intense laser field. Usually, most laser beam has a spatial intensity profile with a maximum on propagation axis. As a result, the laser beam induces a refractive index variation within the medium with a larger refractive index at the center of the beam than at its periphery. The nonlinear medium acts like a positive lens to focus the beam within it. This cumulative process gives rise to increasing laser intensity and thus stronger focusing along the propagation of laser beam. The self-action phenomena is termed self-focusing, illustrated in Fig. 1.2(a).

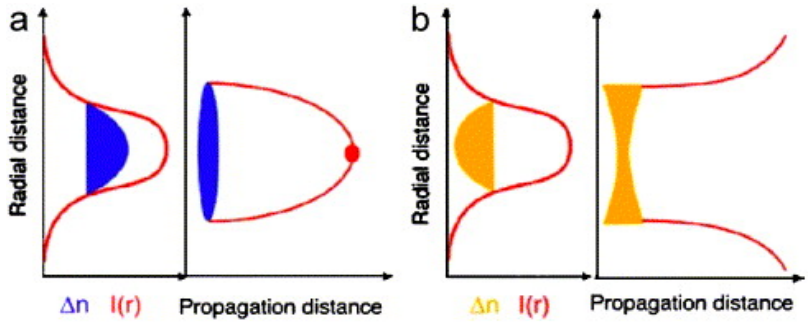

Figure 1.2: (a) Schematic illustration of the self-focusing of a laser beam. The varying refractive index of the medium with the strength distribution of laser beam converges the initially collimated beam, acting as a positive lens. (b) Plasma defocusing of the laser beam. The ionization of the medium initially takes place along the axis, where the laser intensity is maximal. The weakly ionized plasma decreases the local refractive index and therefore causes beam defocusing. Courtesy to the ref. [1].

Self-focusing process overcomes diffraction and results in collapse only if the peak power carried by the beam exceeds the so-called critical power [8]

$$P_{cr} \equiv \frac{3.77\lambda_0^2}{8\pi n_0 n_2}, \tag{1.2}$$

where a Gaussian beam is considered and λ_0 denotes the central wavelength of laser beam. In atmospheric air, P_{cr} is estimated as 3.2 GW for 800 nm Gaussian laser beam. The propagation length of self-focusing beam until collapse L_c can be well estimated by a semi-empirical formula of Dawes and Marburger [9, 10]

$$L_c = \frac{0.367 L_R}{\sqrt{[(P_0/P_{cr})^{1/2} - 0.852]^2 - 0.0219}}, \tag{1.3}$$

where $L_R = \pi\omega_0^2/\lambda_0$ is the Rayleigh length which is the characteristic length of diffraction of Gaussian beam. ω_0 denotes the beam waist in linear focusing geometry. Eq. (1.3) is valid for moderate input power. To have an impression, L_c is approximately 15.6 m for a collimated 800 nm laser beam having a initial power $P_0 = 10P_{cr}$ and a waist of $w_0 = 5\ mm$. In most experiments regarding femtosecond laser filamentation, a lens is used to focus the laser beam to create filaments. In this external focusing geometry, the propagation length until collapse position $L_{c'}$ moves before the linear focus position according to

$$\frac{1}{L_{c'}} = \frac{1}{L_c} + \frac{1}{f} \tag{1.4}$$

where f denotes the focal length of the lens.

In Eq. 1.1, the laser intensity I usually varies in time, leading to a temporal variation of the refractive index as $n(t) = n_0 + n_2 I(t)$. This variation in turn produces new

frequencies in the spectrum of the laser pulse, termed as self-phase modulation (SPM). It plays a dominating role in the generation of supercontinuum covering a large wavelength range. Another effect resulting from the intensity-dependent refractive index is self-steepening. When a laser pulse travels in a medium with positive n_2, its velocity decreases with increasing laser intensity. So the velocity of the peak of the pulse should be smaller than that of the trailing part of the pulse, leading to a steep edge in the trailing part. This effect speeds up the self-focusing of the trailing part of the pulse and generates new blue frequencies [11]. In addition, this self-steepening effect can lead to splitting of the pulse [12].

1.2.2 Plasma defocusing

As mentioned above, the laser pulse self-focuses when its peak power exceeds the critical power P_{cr}. Without other opposite processes to overwhelm it, the self-focusing laser pulse eventually collapses to an optical singularity. In fact, there exists several physical processes acting to arrest the collapse of laser pulse. With modest input laser power, few times P_{cr}, the group velocity dispersion of laser pulse along the propagation axis can prevent the collapse of the self-focusing laser pulse. With higher input laser power, the molecules or atoms will be ionized through multiphoton or tunnel ionization while the laser intensity increases up close to or beyond the photoionization threshold. In this regime, the laser-indcued plasma dominates as a defocusing effect.

The generation of a plasma reduces the local refractive index according to the law

$$n \simeq n_0 - \frac{\rho}{2\rho_c}, \tag{1.5}$$

where ρ is the density of free electrons and ρ_c denotes the critical plasma density, above which the plasma becomes opaque [1]. For 800 nm laser pulse, $\rho_c \sim 1.7 \times 10^{21}\ cm^{-3}$. The reduction of the refractive index because of the plasma generation acts as a divergent lens, preventing the collapse of the self-focusing laser pulse on itself. This effect is schematically depicted in Fig. 1.2(b).

1.2.3 Formation of filament

The combined action of the self-focusing of laser pulse due to the optical Kerr effect and the defocusing due to the plasma generation primarily results in several focusing-defocusing cycles and therefore the formation of filament, even though other effects, such as diffraction, group velocity dispersion, SPM and XPM, self-steepening etc, are also involved in the filament formation. The process of the filament formation is depicted

in Fig. 1.3. In air, the combined action leads to an average filament diameter of about 100 μm over long distance.

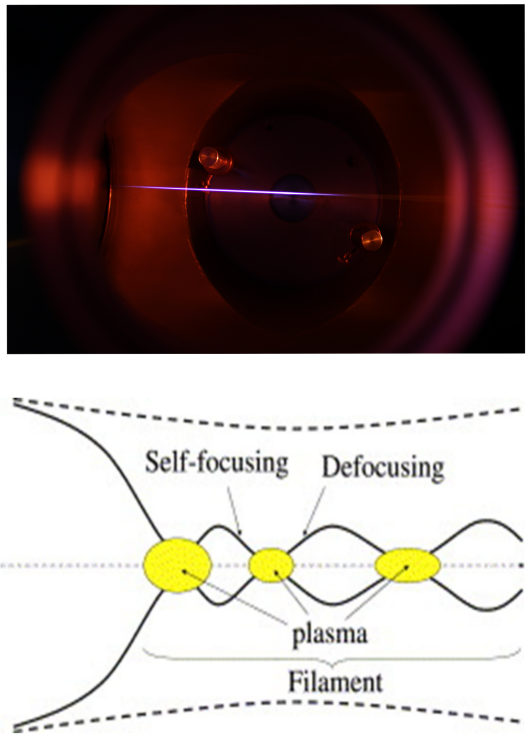

Figure 1.3: (upper panel) A 10-cm-long filament created by focusing 10 mJ 800 nm laser pulse in 1 bar nitrogen gas. (lower panel) Schematic illustratrion of the focusing-defocusing cycles undergone by the laser pulse along the propagation axis. Courtesy to the ref. [1].

1.3 Nonlinear effects during filamentation

Following the previous section, we are about to present several nonlinear effects during femtosecond laser filamentation in gas medium. These effects are directly related to the lasing effect of filament plasma, which is the main topic of this thesis.

1.3.1 Spectral broadening

During laser filamentation, the pump laser pulse experiences strong spectral broadening due to combined effect of self-phase modulation, self-steepening and the ionization of atoms or molecules. The self-phase modulation shifts the trailing edge of laser pulse to higher frequency, and the leading edge of laser pulse to lower frequency, i.e., red shift. The red shift of spectrum was reported as up to 4.5 μm by propagating 2-TW femtosecond laser pulses at 800 nm wavelength in air [13]. On the other hand, the self-steepening

effect as well as ionization preferentially create new frequencies on the high frequency side of the spectrum, i.e., blue shift. Thus, the initial laser pulse partially converts into a continuum extending gradually to the blue side of spectrum.

1.3.2 Conical emission of white light

The white light generation or supercontinuum during laser filamentation generally shows a conical distribution with a white central part surrounded by a rainbow-like emission, as shown in Fig. 1.4. The radial order of the spectral components shows bluer frequencies appearing on the outside rings, which is inverse of diffraction pattern. This phenomena makes it as a signature of laser filamentation. To explain it, several mechanisms have been proposed such as Cerenkov radiation, self-modulation, four-wave mixing and X-waves. A review on this point can be found in this reference paper [1].

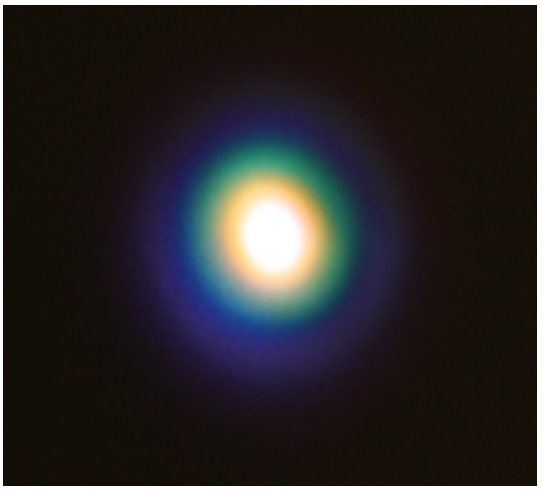

Figure 1.4: Photograph of the conical emission by femtosecond laser filamentation in air.

1.3.3 Raman-Kerr effect and molecular alignment

In Eq.(1.1), only the instantaneous response of bound electrons (< 1 fs) is considered for the optical Kerr response. In fact, in gas medium of molecules, there is another much slow ($\sim$ ps) response contributing to the total optical Kerr response due to the rotation of molecules in the laser field. Basically, the molecule tends to become aligned with the field polarization direction, and the laser pulse then experiences a modified local refractive index because the average polarization per molecule has been changed due to molecular alignment. Since the rotational motions takes place in well-defined states, it has to be treated quantum-mechanically.

The broad bandwidth of femtosecond laser pulses collectively excites the molecule to an ensemble of rotational molecular states, which is an off-resonant impulsive excitation. It leads to a delayed contribution to the local refractive index, causing spectral red shift of pump pulse after propagation in gas. This delayed contribution to the change of local refractive index is given by [14]

$$n(t) = n_0 + n_2 I(t) + \int_0^\infty R(t')I(t-t')dt' \tag{1.6}$$

where $R(t')$ is the time-dependent Raman response function. As can be seen in Eq. (1.6), the contribution from the delay Raman response to the variation of local refractive index is the convolution of the delayed temporal profile of the pump laser intensity with $R(t')$. $R(t')$ was described by the following response function

$$R(t') = n_{2,rot} \sum_{J=0}^{\infty} F_J \sin(-\omega_J t') \tag{1.7}$$

where $n_{2,rot}$ is the overall magnitude of this effect and is given by

$$n_{2,rot} = \frac{32\pi^2 N}{hcn_0}\beta^2(\omega) \tag{1.8}$$

with $\omega = 2\pi\nu$, N is the gas density. $\beta(\omega)$ the anisotropy of the molecular polarizability defined as

$$\beta(\omega) = \alpha_{\parallel}(\omega) - \alpha_{\perp}(\omega), \tag{1.9}$$

where $\alpha_{\parallel}(\omega)$ refers to the polarizability along the symmetry axis of the molecules and $\alpha_{\perp}(\omega)$ the polarizability along any directions perpendicular to the the symmetry axis. In Eq. 1.7, the coefficient F_J represents the contribution importance from each rotation state, given by

$$F_J = [\rho_{J+2} - \rho_J] Z_J \frac{(J+2)(J+1)}{2J+3} \tag{1.10}$$

where J, $J+1$ and $J+2$ represent the rotational level, and ρ_J denotes the molecule population in the rotational level J, and Z_J is the weighting factor describing the multiplicity of each level. For N_2 molecule, transitions from even J rotational levels are twice more intense than those from odd ones, i.e., $Z_J = 1$ for odd J while $Z_J = 2$ for even J. The population ρ_J is determined by the following Boltzmann's statistics given by

$$\rho_J = \frac{\exp[-hcBJ(J+1)/k_BT]}{\sum_{J=0}^{\infty}\exp[-hcBJ(J+1)/k_BT]} \tag{1.11}$$

where B is the rotational constant of the molecule, k_B the Boltzmann's constant and T the absolute temperature. In Eq. 1.7, the last parameter ω_J is the angular frequency difference between the coupled rotational levels

$$\omega_J = 4\pi Bc(2J+3). \tag{1.12}$$

Because of the rotation of molecules in the laser field, we can expect the Raman response function should have a periodic revival structure. Using Eq. 1.7, the revival of the Raman response function for various molecular gases can be calculated. For N_2 molecules, the rotational constant B is 1.99, and its polarizability anisotropy $\beta(\omega)$ is around 1.0×10^{-40} C^2m^2/J [14]. With the conditions of 40 fs laser pulse at 800 nm wavelength, the nonlinear Raman response function of N_2 molecule is calculated as a function of time, as shown in Fig. 1.5. We can see that the revival period of Raman response function of N_2 molecule is around 8.4 ps, and half-period about 4.2 ps. In this thesis, we will see that this delayed nonlinear response due to molecular alignment contributes to the lasing effect, leading to revival structures in gain dynamics and temporal profiles of lasing pulse.

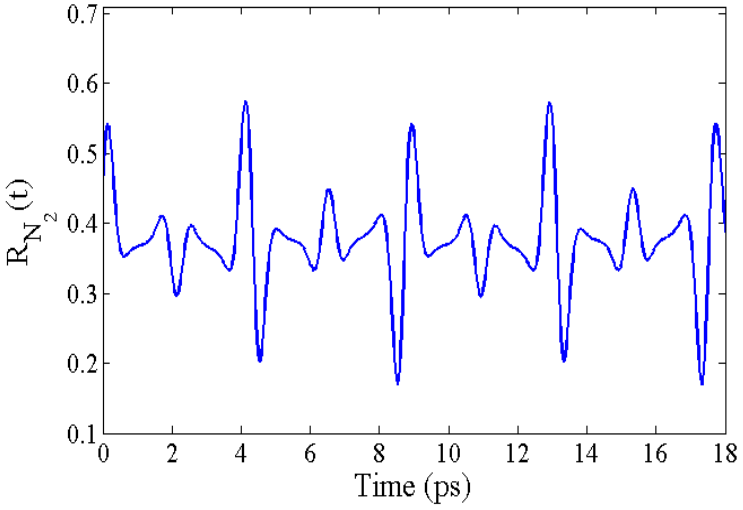

Figure 1.5: Calculated Raman response function of N_2 molecule as a function of time.

1.3.4 Lasing effect in filament plasma

In recent 5 years, it was discovered that filamentary plasma can give rise to stimulated emission. The pencil-shaped filament plasma channel gives a favorable geometry for optical gain, associated with nitrogen molecule, nitrogen ion, oxygen atom, nitrogen atom, as well as noble gas argon. Lasing effect related to nitrogen molecule can be categorized to two types. The first type of lasing effect is the lasing action of the second

negative band of neutral nitrogen molecules, corresponding to the transition from $C^3\Pi_u^+$ to $B^3\Pi_g^+(\upsilon = 0, 1)$ state [15–19]. The pioneering research work about it was published in 2003 [15], where the backward lasing was suggested. The backward lasing is particularly interesting because of its potentials for atmospheric remote sensing applications. We have generated strong 337 nm lasing pulse by using 800 nm circularly polarized laser pulses, illustrated in Fig. 1.6. Our experiment results prove that the lasing action of neutral nitrogen molecules can be possible only with circularly polarized femtosecond pump laser at 800 nm. In this thesis, the lasing action at 337 nm wavelength of neutral nitrogen molecules in filament plasma will be presented in Chapter 2-4.

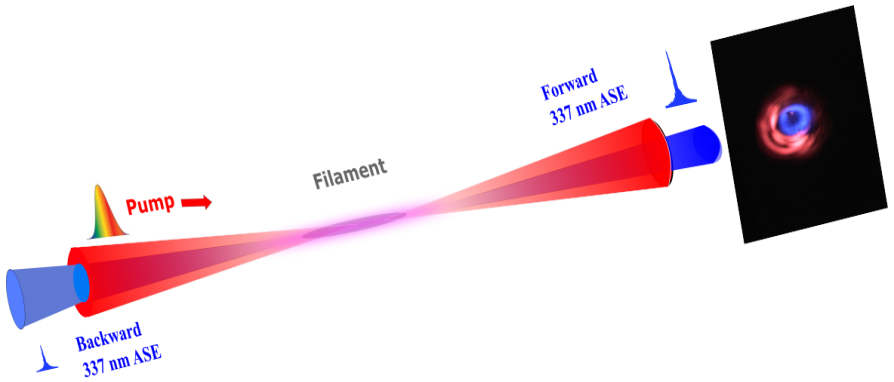

Figure 1.6: Schematic illustration of 337 nm ASE-type lasing effect of neutral nitrogen molecules in filament plasma. The photograph for forward 337 nm ASE is shown on the right.

Another type of lasing action in filament plasma is from ionic molecule N_2^+ [20–27]. It mainly occurs at 391 nm and 428 nm wavelengths. These two wavelengths corresponds to the $B^2\Sigma_u^+ \rightarrow X^2\Sigma_g^+$ transition between the excited and ground cation states. The 391 nm lasing emission is normally generated at low gas pressure while the 428 nm lasing emission at high gas pressure. It has been confirmed that this type of lasing emission is superradiance by measuring its temporal profile [28]. The experiment and simulation results about this ionic nitrogen lasing will be presented in Chapter 5-6.

1.4 Summary

Femtosecond laser filamentation primarily results from a dynamic competition between the self-focusing due to the optical Kerr effect and plasma defocusing due to ionization. It enables extending the filamentation over Rayleigh lengths by many times, resulting in a long filament plasma column. Various nonlinear effects are involved in femtosecond laser filamentation, which makes it a fascinating field covering nonlinear optics, quantum optics, plasma physics, atomic and molecular physics. In following chapters, we

are going to explore a research field in femtosecond laser filamentation under intensive studies, namely lasing action of nitrogen molecules.

Part II

337 nm Nitrogen Lasing in Femtosecond Filaments

Chapter 2

Bidirectional 337 nm Lasing in Femtosecond Filaments

Contents

"Air lasing", which refers to the pumping of the constituents of ambient air that results in a directional laserlike emission, has emerged as an attractive topic in recent 5 years, due to its potential for remote sensing applications. Traditional optical remote sensing systems for probing the atmosphere rely on collecting backward scattered incoherent light from targets in the atmosphere by detectors on the ground, a technique hindered by low efficiency and poor directionality. Availability of a light source which emits coherent light in the backward direction from a certain point in the sky back towards a ground-based detector, could have a great impact on the efficiency and precision of optical remote sensing techniques.

In this chapter, we report the observation of a bidirectional lasing emission at 337 nm wavelength, from few-centimeter-long, 100 $\sim$ 200 μm-wide filament plasma which is created by focusing circularly-polarized 800 nm femtosecond laser pulse in pure nitrogen or ambient air. We particularly focus on the backward nitrogen lasing emission because of its interests for remote atmospheric sensing.

We start by presenting the research background including previous studies of lasing action from filament plasma and a brief introduction to optical remote sensing. Then we show the observation and characterization of bidirectional 337 nm lasing emission enabled by circularly polarized pump laser, including its spectra, spatial profile, divergence, energy, etc. The 337 nm lasing action in ambient air is also presented. Finally, the temporal profiles of lasing emissions in both directions will be discussed.

2.1 Research background

2.1.1 Lasing action from filament plasma

The first research work about lasing action from femtosecond laser-induced filament in air was published in 2003 [15]. The authors focused 42 fs, 800 nm laser pulses in air to generate a filament plasma with a length of few centimeters, and then collected the backward emission by a photomultiplier (PMT) connected to an oscilloscope. Before the PMT, interference filters were used to select the backward emission signal at certain wavelengths. They measured the backward emissions at 337 nm and 357 nm wavelengths as a function of the incident pump energy. The 337 nm and 357 nm are transitions of the triplet states of neutral nitrogen molecule which has been historically named as the second negative band, from $C^3\Pi_u^+(\upsilon' = 0)$ to $B^3\Pi_g^+(\upsilon = 0, 1)$, where υ denotes the vibrational level at each electronic state, as shown in Fig. 2.1.

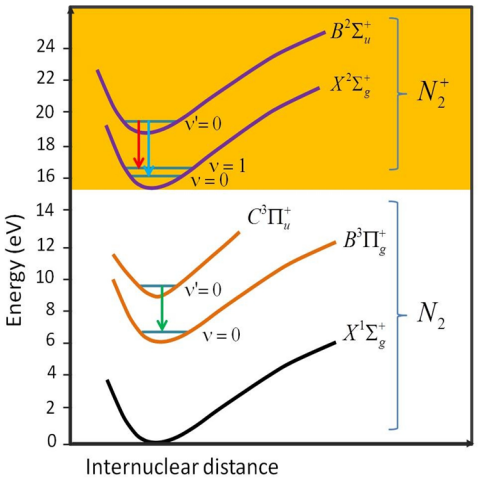

Figure 2.1: Schematic diagram of the potential energy levels of the neutral and ionic nitrogen molecule. The symbols ν and ν' denotes the quantum numbers of vibrational levels.

The sole proof of lasing action in this work was based on the exponential fit of the dependence of backward emission intensity on the filament length. Later, it was pointed out that the reasoning and conclusion are questionable [16]. Firstly, the filament length was not experimentally measured but calculated from the incident pump energy by using the Marburger formula (see Eq. 1.3). In fact, this formula is only applicable for single filament regime where incident laser power is close to the critical power for self-focusing. However, the experiment in this work was carried out with laser power ranging from about 11 to 170 critical powers of self-focusing, assuming the critical power in air to be 5 GW [1]. Secondly, multiple filamentation occurs at such high incident laser power, which wasn't considered. Mostly important, the authors treated the geometrical length of filament plasma as the gain length, which was later found to be not correct. Actually, the effective gain length for backward lasing is much less than the geometrical length due to the short lifetime of the optical gain [17]. Nevertheless, this work serves as the first suggestion of backward lasing from femtosecond laser filamentation in air, for which it is important.

In 2011, a real experiment breakthrough about air lasing was reported [29]. It is based on photo-dissociation of oxygen molecules in ambient air and resonant photo-excitation of oxygen atoms by using 226 nm pump laser. Both forward and backward coherent emission at 845 nm wavelength was observed. The physical picture of the buildup of population inversion consists of three steps: at the first step, the oxygen molecule is dissociated to two oxygen atoms by two photons at 266 nm, and subsequently the dissociated oxygen atom is resonantly driven by another two photons to its excited state, and finally the excited atom will emit coherent emission at 845 nm wavelength due to population inversion. The same method was applied to nitrogen molecule, in

which case 745 nm lasing emissions in both directions were observed by using 207 nm pump laser. However, for real applications, the difficulty of this scheme is that the deep-UV pump pulses at 226 nm or 207 nm wavelengths has a poor transmission in air, and therefore the propagation distance of pump laser is significantly limited.

Another work on filament-assisted lasing action of neutral nitrogen molecules was reported by in 2012 [16]. In this work, the authors focused an mid-infrared laser at 4 μm or 1.03 μm wavelength into a gas mixture of 5 bar argon and 1 bar nitrogen. In the backward direction, a microjoule (μJ) level lasing energy of both 337 nm and 357 nm emissions was detected, which corresponds to a 0.5% conversion efficiency from mid-infrared pump laser to the lasing energy. The underlying mechanism of population inversion between $C^3\Pi_u^+(\upsilon^{'}=0)$ and $B^3\Pi_g^+(\upsilon=0,1)$ states was attributed to that the argon atoms in the excited state collide with the nitrogen molecules in the ground state, and then transfers its excitation energy to the nitrogen molecule through $Ar^*(4^3P_2) + N_2(X^1\Sigma_g) \rightarrow Ar + N_2(C^3\Pi_u)$ collision. Thus, the excited argon atoms can provide a collisional pump for laser transitions of N_2 in a laser-induced filament plasma, playing the same role as the one played by hot electrons in a conventional discharge-pumped nitrogen laser. However, the significant difficulty of this experimental scheme is the requirements of high pressure argon gas, which is not possible for real remote sensing application in atmospheric air.

In the above two works, either deep-UV pulse or mid-IR pulse were used as pump laser to drive the lasing effect. As the mostly equiped femtosecond laser system is at 800 nm wavelength, is it possible to be applied to generate a laser source emitting in the backward direction? Recently, we reported that an intense stimulated emission at 337 nm wavelength from filaments in nitrogen gas can be achieved with circularly polarized 800 nm femtosecond laser pulses at the atmospheric pressure [18]. It occurs in both forward and backward directions, and the former prevails dramatically. This 337 nm lasing emission critically depends on the ellipticity of pump laser. The challenge of this scheme is related to the quenching effect of oxygen molecules in air, which significantly suppress the lasing action.

2.1.2 Optical remote sensing

To better illustrate the potential of air lasing for remote sensing application, here we introduce briefly the basis of current optical remote sensing technique. Optical techniques for the remote sensing applications, like standoff detection of hazardous gases in atmosphere, are based on using laser to precisely identify and quantify species of interest. The mostly employed LIDAR (LIght Detection And Ranging) is an optical remote

sensing system for probing the earth's atmosphere through laser transmitter using elastic and/or inelastic scattering techniques. Most of them consist of three functional subsys-

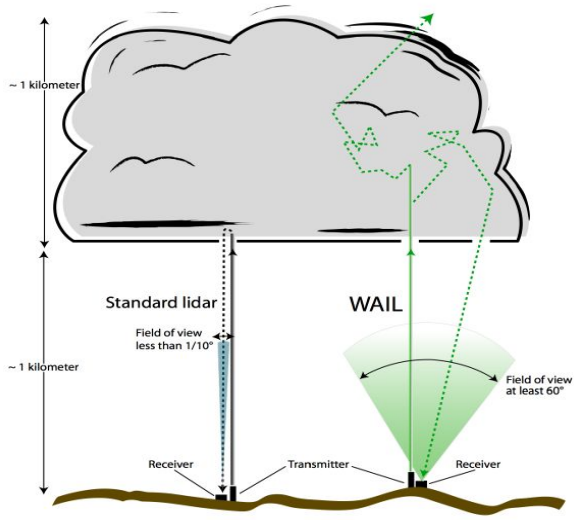

Figure 2.2: Lidar observations of a dense cloud. Left: standard (single-scattering/on-beam) lidar. Right: multiple-scattering/off-beam lidar. Courtesy to the research on website: http://asr.science.energy.gov/science/research-highlights/RMTQw/view.

tems, which are: (1) Transmission subsystem, (2) Receiver subsystem, (3) Electronics subsystem, as shown in Figure 2.2. In the LIDAR system, the light scattering occurs at all wavelengths in the electromagnetic spectrum and in all directions. The collection of signal is in backward direction (scattering angle $\theta_s = 180°$ for monostatic vertically pointed lidar) in order to enable detection on the ground. The non-directional nature of scattered emission from molecules of interest limits its collection. When the laser light interacts with the target molecules, the scattered light propagates in every direction and therefore the scattered light in backward direction is weak, which limits the detection sensitivity and precision. Additionally, the backward optical signal is also not coherent light.

For more sensitive detection, a coherent backward signal beam with well-defined direction will be ideal. But it is prohibited by the phase-matching condition when the pump lasers propagate in the forward direction. As a result, a backward air laser, a coherent beam directed from the sky to the ground observer is highly desired. The concept of remote sensing based on backward air lasing can be illustrated as follows (see Figure 2.3). As the first step, the femtosecond laser is focused into atmospheric air to generate a filament plasma, which provides the backward lasing beam. In the second step, the backward lasing beam interacts with the target molecules and therefore it will carry the information of target molecules. For example, this interaction could be a backward coherent Raman scattering process, with the aid of another forward

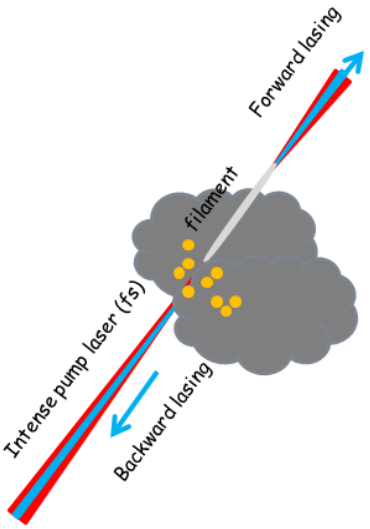

Figure 2.3: The schematic illustration of the concept of backward lasing-based remote sensing. The yellow dots denotes molecules of interest.

wavelength-tunable beam, which could provide chemically specific sensing of airborne trace gases or pollutants.

2.2 Backward 337 nm lasing from filament plasma

In this section, we present the observation of backward 337 nm lasing emission from few-centimeter-long filament plasma created by circularly polarized 800 nm pump laser pulses in pure nitrogen gas. Firstly the experiment setup will be introduced, and the following is the experimental results, and in the end a summary of this part will be given.

2.2.1 Experimental setup

In our experiment, a commercial Chirped Pulses Amplification (CPA) laser system (Thales Laser, Alpha 100, see Appendix A for details) was used. This system delivers 45 fs laser pulses at a repetition rate of 100 Hz, with a maximum pulse energy of 15 mJ. A schematic illustration of the experiment setup is presented in Fig. 2.4.

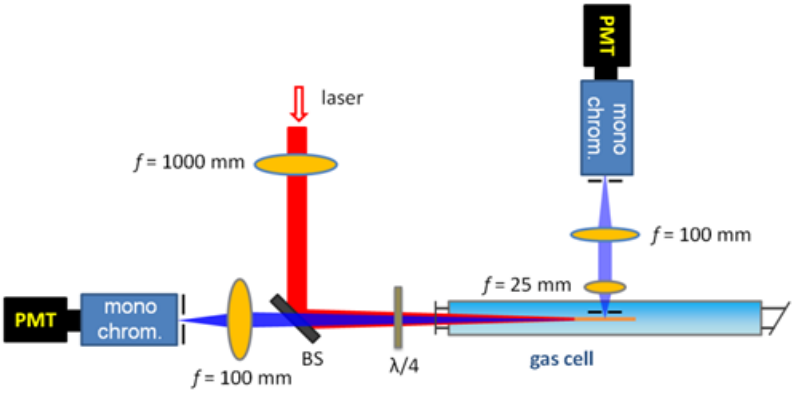

Figure 2.4: Schematic illustration of the experimental setup. Here, the signal of interest is measured by a monochromator combined with a photomultiplier tube.

The 800 nm pump laser pulse is focused by an $f = 1000$ mm convex lens and then passes through a quarter waveplate ($\lambda/4$). By rotating the quarter waveplate, we can change the ellipticity of pump laser. A dichromatic mirror was used to reflect the focused 800 nm pump pulses into a gas chamber filled with pure nitrogen gas at 1.0 bar pressure. A few-centimeter-long filament will be created inside the gas chamber. This dichromatic mirror reflects more than 99% of the 800 nm pump pulse and is transparent for the backward ultraviolet emission from the laser-induced filament plasma located inside the gas chamber. The backward emission from the laser plasma filaments was collected by an $f = 100$ mm silica lens and then detected by either a spectrometer (Ocean Optics HR 4000), an intensified Charge Coupled Camera (Princeton Instrument, model: PI-MAX), a monochromator (Jobin-Yvon H-20 UV, grating: 1200 g/mm) combined with a photomultiplier tube (PMT), or a calibrated photodiode.

The transverse fluorescence from the filament plasma was also measured by a monochromator combined with a PMT. The transverse fluorescence passing through the chamber window is first collimated by an $f = 2.5$ cm fused silica lens and then focused by another $f = 10$ cm fused silica lens to the incident slit of the monochromator.

2.2.2 Backward 337 nm stimulated emission from nitrogen filament with circularly polarized pump laser

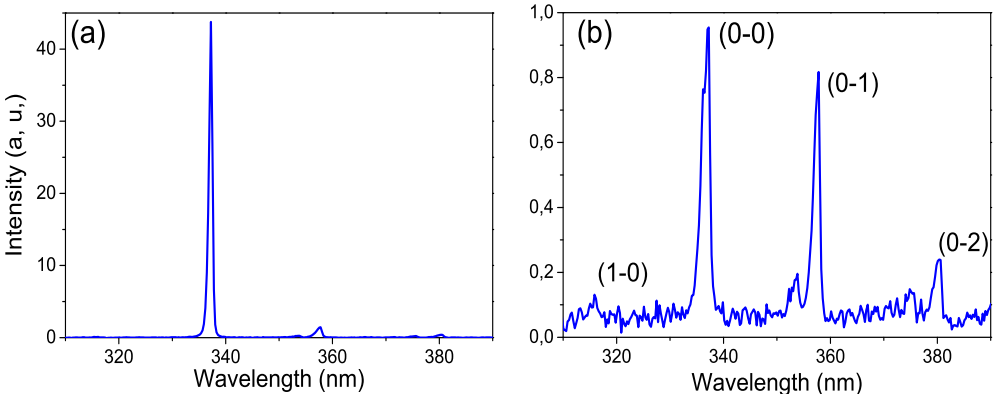

Figure 2.5: Backward emission spectra from 6-cm long filament plasma generated by circularly (a) and linearly (b) polarized pump pulses in 1-bar nitrogen gas.

In this experiment, a 6-cm long filament plasma was formed with pump pulse energy of 8.5 mJ in 1.0 bar pure nitrogen gas. The results of spectra for circularly (a) and linearly (b) polarized pump pulses are shown in Fig. 2.5. In Fig. 2.5(b), the fluorescence emission lines at 315 nm, 337 nm, 357 nm, 380 nm have been well identified as the transitions from the $C^3\Pi_u^+$ to $B^3\Pi_g^+$ states of the neutral nitrogen molecules with different initial and final vibrational quantum numbers, as denoted in the figure. In addition, one can observe that each line consists of two peaks, namely R-branch (weak peak on the left) and P-branch (strong peak on the right) of transition. Interestingly, when the polarization of pump laser was changed from linear to circular, the emission intensity at 337 nm wavelength increases by almost 40 times compare to that obtained with linearly polarized pump laser. Notice that the emission lines at 357 nm and 380 nm wavelengths still keeps its intensity.

The spectra of figure (a) and (b) are compared with normalized intensity, as shown in Figure 2.6, in order to examine the linewidths of 337 nm emission lines for two cases with different polarizations of pump laser. The linewidth of 337 nm emission with circularly polarized pump laser is about 1.06 nm, which is twice less than that with linearly polarized one. Note that the 1.06 nm bandwidth is mostly related to the spectral resolution of our fiber spectrometer.

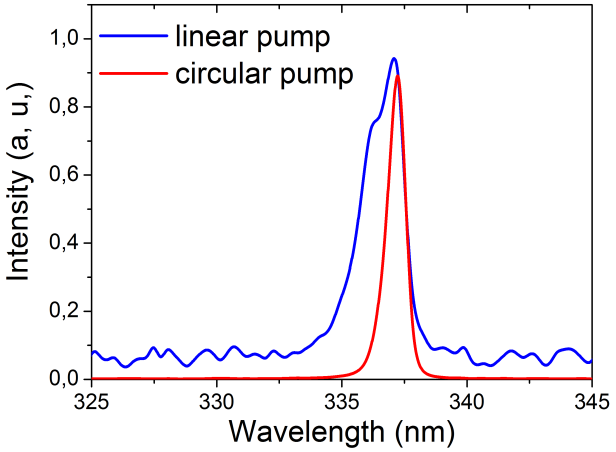

Figure 2.6: The spectra of 337 nm emission in the backward direction for linear and circular pump laser, in which their intensities are normalized.

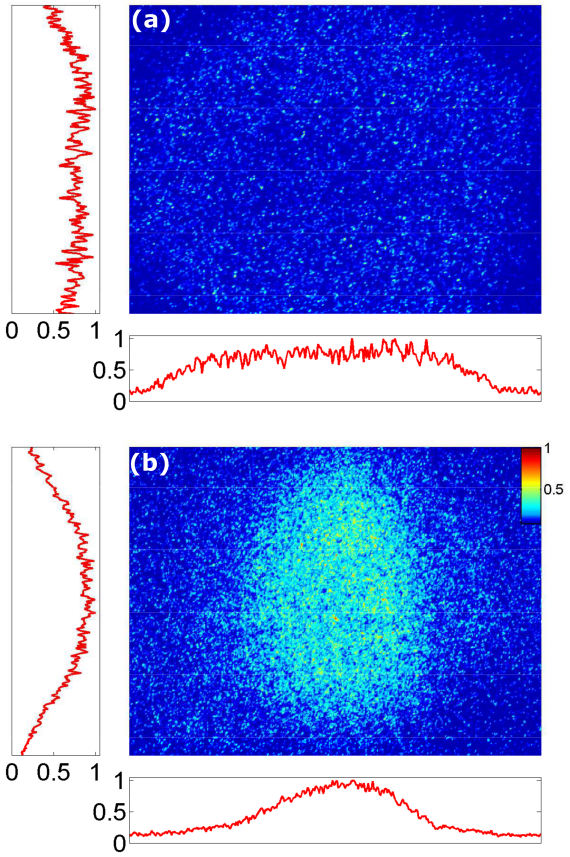

Figure 2.7: The spatial profiles of 337 nm emissions measured by iCCD camera in backward direction for linearly (a) and circularly polarized (b) 800 nm pump laser pulses in 1 bar nitrogen gas. The red curve represents the normalized space-integrated intensity along the corresponding axis.

By using an iCCD camera with high sensitivity, the spatial profiles of 337 nm emission were measured. Before doing that, a UV filter centered at 337 nm wavelength with bandwidth of 10 nm was placed very close to the entrance of iCCD camera in order to filter out other frequency components. The measured spatial profile of the backward emission with linearly polarized pump laser are shown in Figure 2.7, where no detectable signal was observed. However, with circularly polarized pump laser, we can see an obvious spatial profile of 337 nm emission and it exhibits a Gaussian distribution (Fig. 2.7(b)). Its divergence is then calculated by measuring the 337 nm beam diameter in two different positions, which gives a divergence of 9.2 mrad. This result means the 337 nm emission from filament plasma is highly directional in the backward direction. These spatial profile measurements agree with the above spectral measurements where significant increased emission at 337 nm has been generated by circularly polarized pump laser pulses.

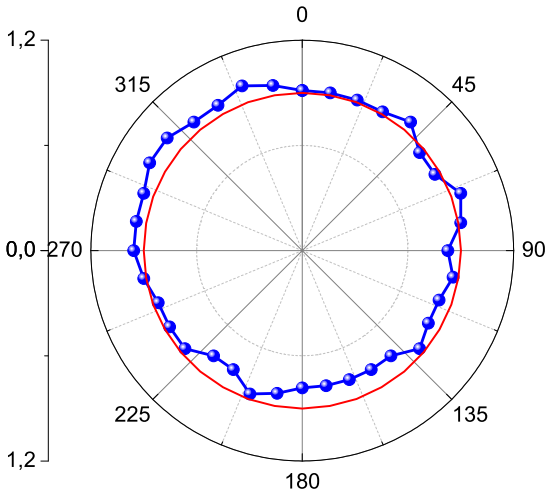

Figure 2.8: Polarization of the backward 337 nm ASE with circularly polarized pump laser. The solid-red line denotes the theoretical fit of Malus' law .

The above experimental results, including the significant increase of emission intensity, the spectral narrowing, and the high directionality of 337 nm emission beam, strongly suggests stimulated emission of the backward optical signal at 337 nm wavelength from filament plasma driven by circularly polarized 800 nm pump laser. This indicates that optical gain at 337 nm wavelength occurs in filament plasma.

The polarization of the backward 337 nm emission was then measured by inserting a Glan-Taylor polarizor before a detecting photodiode. In the experiment, we recorded the intensity of the transmitted 337 nm emission as a function of the rotation angle of the Glan-Taylor polarizor. The result is shown in Figure 2.8. It indicates the backward 337 nm emission is not polarized. Therefore, the observed 337 nm stimulated emission

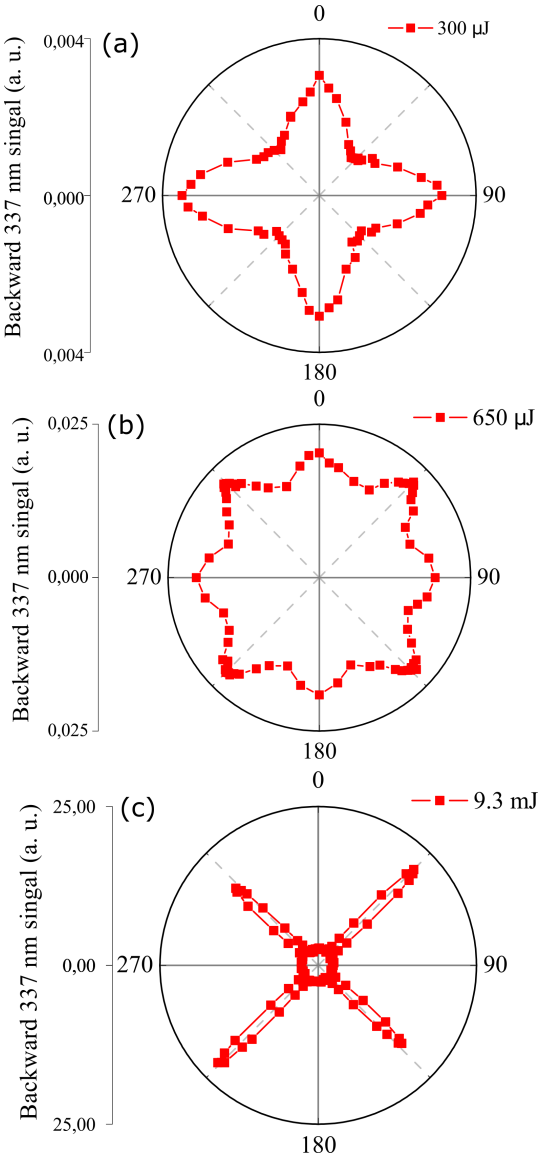

Figure 2.9: Backward emission intensity at 337 nm wavelength as a function of the rotation angle of the quarter-wave plate. The incident pump laser energy for (a), (b), (c) are 0.3 mJ, 0.6 mJ, and 9.3 mJ, respectively. Angle 0° corresponds to the linear polarization of pump laser. The emission signal was collected by a PMT followed by a monochromator.

can be attributed to Amplified Spontaneous Emission (ASE). In the following content, this laser-like emission will be called as 337 nm ASE.

The linear and circular polarization are two special cases of pump laser ellipticity, with ellipticity of 0 and 1 respectively. For having a general picture, we investigated the 337 nm ASE lasing as a function of pump laser ellipticity by rotating the $\lambda/4$ waveplate for different incident pump laser energies (see Fig. 2.9). The angles $\phi = 90° \times m$ correspond to linearly polarized laser, with $m = 0, 1, 2, 3$. The angles $\phi = 45° + 90° \times m$ correspond to circularly polarized laser. For a low pulse energy of 300 μJ, linearly polarized pump pulses generate a 337 nm radiation with an intensity twice stronger than

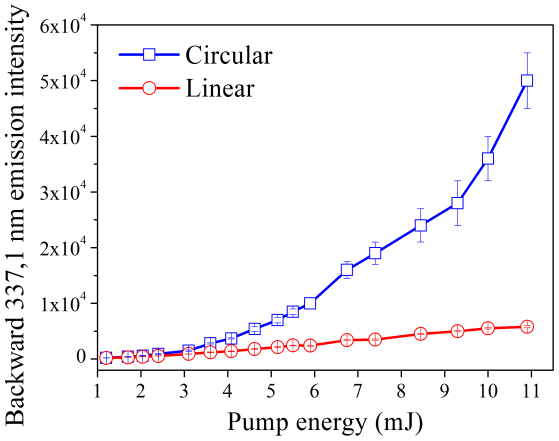

Figure 2.10: Backward 337 nm ASE intensity as a function of incident pump pulse energy, for both circular (blue diamond) and linear (red circle) polarizations of pump laser.

that obtained with circularly polarized one. For an increased incident energy of 660 μJ, an octagon-shaped dependence is observed, indicating the onset of a new mechanism for the emission at 337 nm. In the case of $E_{in} = 9.3$ mJ, the signal obtained with circular laser polarization dominates and decreases rapidly when the laser polarization deviates slightly from circular.

While the polarization of pump laser was set to be circular, the pump laser energy dependence of backward 337 nm ASE lasing intensity was measured with fiber spectrometer. Two UG11 filters is used to block infrared light and a $f = 100$ mm fused silica lens was used to collect the backward emission into the detecting fiber. It shows a monotonous increase with the energy of pump pulse (see Figure 2.10). Increasing pump pulse energy generates longer and wider filament plasma [18], and its volume almost linearly depends on the pump pulse energy. Therefore, this measured result also indicates the backward 337 nm emission intensity exponentially depends on the filament volume when the pump laser is circularly polarized, which is different from that of linearly polarized pump laser. Note that the backward 337 nm lasing threshold is about $\sim$ 4.0 mJ, from where the emission intensity for circular polarization increases super-linearly with pump energy.

2.3 Forward 337 nm nitrogen lasing emission

We notice that the 337 nm lasing emission can also be generated in forward direction. The intensity of forward lasing is actually much stronger than that in backward direction, no matter in nitrogen or ambient air. In our experimental practice, as the 337 nm lasing signal in forward direction can be rather easily observed, we can then further optimize the experimental conditions, such as the pump laser alignment, the angle of quarter

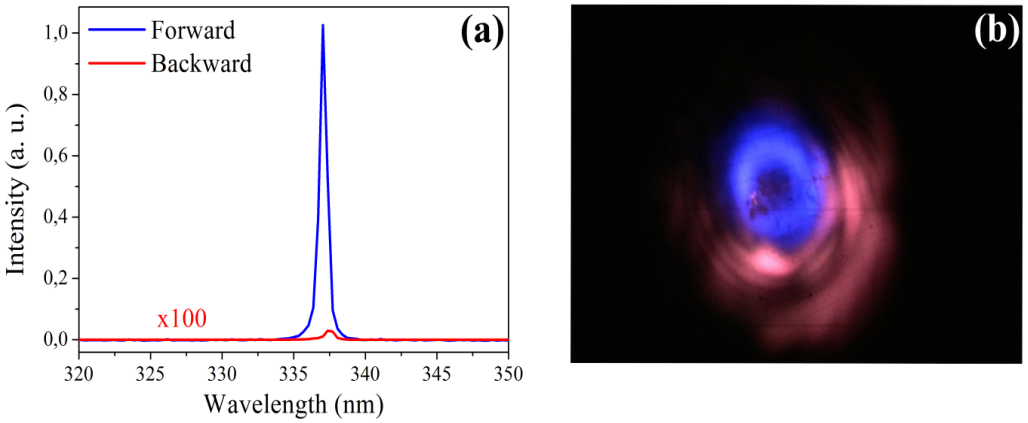

Figure 2.11: (a) Spectra of 337 nm laser in the forward (blue) and backward (red) direction, where the latter is enlarged by 100 times as denoted in the figure. (b) Photo of the forward 337 nm lasing emission beam after UG11 filter taken by mobile phone.

waveplate etc, in order to detect the 337 nm lasing emission in backward direction. In this section, the forward 337 nm lasing emission will be characterized and compared to the backward one as shown above.

In the experiment, we focused circularly-polarized 800 nm laser pulse with pulse energy of 13.6 mJ and duration of 42 fs by 1-m lens to generate 6-cm-long, 400-μm-wide filament plasma in 1.0 bar pure nitrogen. After the exit window, a UG11 filter was used to block the fundamental light and attenuate the accompanying white light. The emissions in both directions were detected by fiber spectrometer and compared. Figure 2.11(a) shows the spectra results. We can see that the forward 337 nm lasing

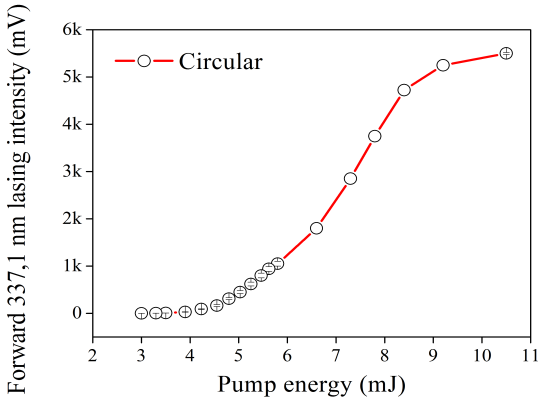

Figure 2.12: Pump energy dependence of 337 nm lasing emission in forward directions. The signal was detected by a calibrated photodiode.

emission is much stronger than the backward one by 3 orders of magnitude. By placing a white paper, a donut spatial shape of the forward 337 nm lasing beam can be clearly seen by naked eyes, as shown by Fig. 2.11(b). In contrast, the backward 337 nm lasing

beam has a central-maximum profile as shown in previous section. In order to obtain its beam divergence, we measured the beam size and distance from the filament plasma at two different positions. A divergence of ∼10.0 mrad was obtained for the forward 337 nm lasing beam, which is close to that of backward 337 nm lasing beam (∼ 9.2 mrad).

For the forward 337 nm lasing emission, the pump energy thresholds was found to be around 4.0 mJ under our experimental setup, as shown in Fig. 2.12. When the pump energy exceeds the threshold of 4 mJ, the forward 337 nm lasing intensity increases more rapidly than the backward one with increasing pump energy. As shown in Fig. 2.11, the lasing intensity in forward direction can be 3 orders of magnitude stronger that that in backward direction when the pump laser energy is about 13.6 mJ. We didn't show the forward 337 nm emission intensity for linear pump laser, because there is strong third harmonic generation in forward direction when the pump laser polarization is linear. The 3^{rd} harmonic signal covers a large range of spectra so that we can't isolate the 337 nm emission signal.

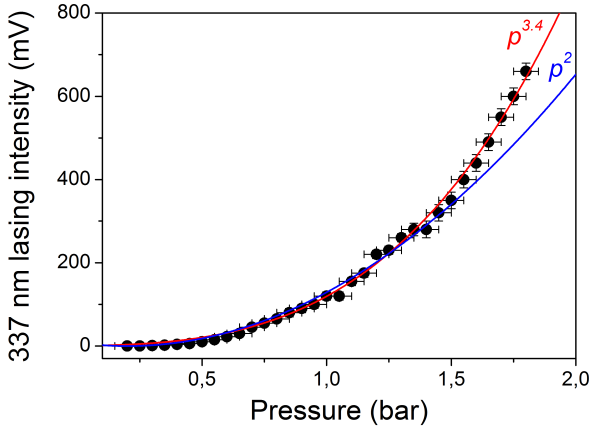

Figure 2.13: 337 nm lasing emission in forward direction as a function of the nitrogen gas pressure. The pump pulse energy is about 9 mJ and the focal length is 1 m. The polarization of pump pulse was set to be circular. The line curves show the polynomial fits.

Figure 2.13 shows the dependence of 337 nm lasing intensity in forward direction on the nitrogen gas pressure. It shows a polynomial dependence relation of $I_{337} \propto p^{3.4}$ within the nitrogen gas pressure range from 0 to 2.0 bar, where I_{337} is 337 nm lasing intensity and p is nitrogen gas pressure respectively. Following the trend of dependence, we can expect stronger 337 nm lasing emission at higher gas pressures. However, it is not so necessary to extend further gas pressure from the point view of application in ambient air.

2.4 337 nm lasing emission in ambient air

For practical application of this backward 337 nm lasing source for remote sensing, its operation in ambient air is mandatory. Therefore we studied the 337 nm lasing action in ambient air. First we measured the bidirectional 337 nm emission from filament plasma formed in ambient air driven by both linearly and circularly polarized pump laser pulses. Second, we examined the influence of oxygen molecules on the 337 nm lasing emission by varying the percentage of oxygen while keeping the total gas pressure at 1 bar. In the end, we give the explanation to the question why in air the lasing action is weak.

Figure 2.14 shows the spectra result of forward 337 nm ASE lasing emission from filament plasma in air and nitrogen. In the experiment, the pulse energy of pump laser was 14.0 mJ, and the pulses were focused by 1-m focal lens. The polarization state of pump laser was set to be circular. It is clear that the 337 nm ASE intensity in air is much weaker than that in nitrogen under same pressure. An estimation of $I_{N_2}/I_{air} \sim 240$ can be got under this experiment condition.

For backward 337 nm emission in air, the emission intensity with circular pump pulses is just few times stronger than with linear pump pulses, as shown in Fig. 2.15. Previous results of backward 337 nm emission in pure nitrogen (see Fig. 2.9) shows huge difference between circular pump pulse and linear one. In air and under same experimental condition, this difference becomes much smaller. From above two results, one can see that 337 nm lasing from neutral nitrogen molecules is dramatically suppressed in air compared to that in pure nitrogen.

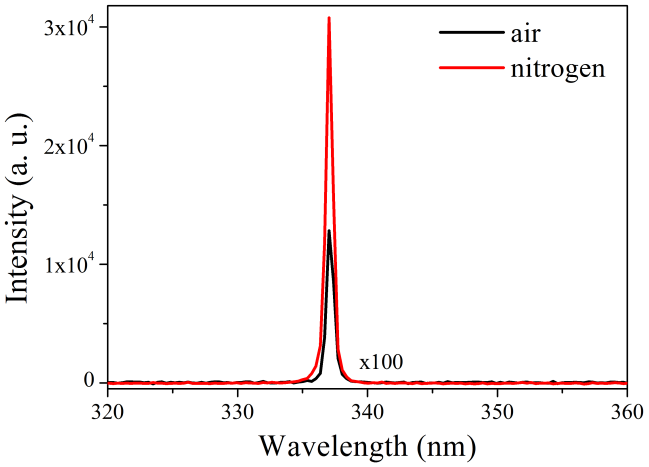

Figure 2.14: Spectrua of forward 337 nm ASE lasing emission from filament plasma in air and nitrogen with pressure of 1 bar. The lasing intensity in air was magnified by one hundred times for easier comparison.

Figure 2.16 presented the backward 337 nm emission signal in different mixtures of pure nitrogen and oxygen to assess the influence of oxygen molecules for the lasing action. The 337 nm signal for both circularly and linearly polarized laser as a function of the percentage of oxygen was measured. A slow decrease of the signal was observed upon increasing oxygen concentration up to 10%. Beyond 10% oxygen, the signal shows a rapid decrease, indicating the termination of significant lasing action. For oxygen concentration more than 13%, the signal obtained with circular laser polarization becomes ~ 2 times larger than that of linear laser polarization, similar to the transverse fluorescence.

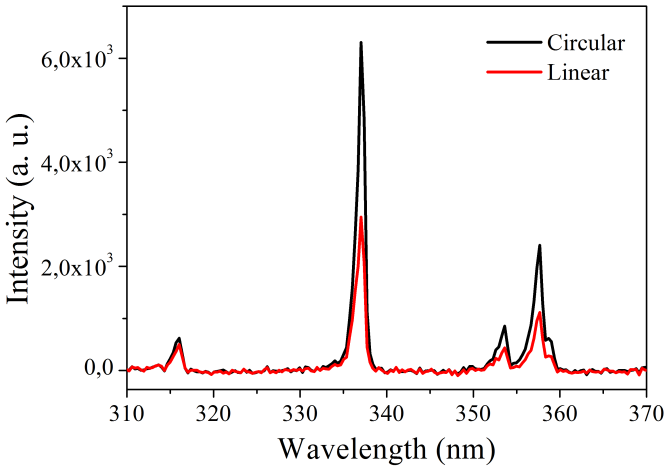

Figure 2.15: Spectrua of backward 337 nm emission from filament plasma in 1 bar air both for circular and linear pump laser.

The presence of oxygen molecules in air suppressed significantly 337 nm lasing emission from nitrogen molecules in filament plasma. For conventional discharge-pumped 337 nm nitrogen laser, it also experiences detrimental influence of oxygen molecule and the mechanism has been well documented [30]. The underlying physical mechanism is attributed to the collision reactions

$$N_2(C^3\Pi_u^+) + O_2 = N_2(X^1\Sigma_g^+) + O + O \tag{2.1}$$

$$N_2(C^3\Sigma_u^+) + N_2 = N_2(a^1\Sigma_g^+) + N_2, \tag{2.2}$$

which efficiently reduces the population density in the upper state $C^3\Pi_u^+$ of 337 nm lasing. In the studies of high pressure plasma created by high repetition-rate nanosecond pulsed discharges in air, it was found that a rapid production of O radicals follows a fast decay of electronically excited states of molecular nitrogen (N_2^*), indicating that dissociative quenching of N_2^* by O_2 may be the main O radical production channel [31]. Kinetic experiments also suggest that ground-state molecular oxygen O_2 quenches N_2^* more effectively than molecular nitrogen molecule. This first dissociative process

expressed by Eq. 2.1 has a reaction rate coefficient $k = 10 \times 10^{-11}\ cm^3 s^{-1}$, four times higher than the rate coefficient of nitrogen-nitrogen molecule collisions. There are also other reactions, such as dissociative recombination, molecular attachment and electron-oxygen collision, contributing to the reduction of 337 nm lasing efficiency.

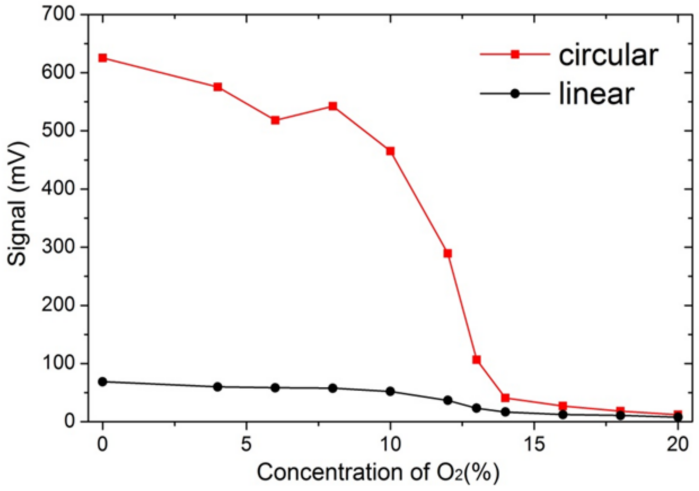

Figure 2.16: Measured backward 337 nm lasing signal from filament plasma in a mixture of nitrogen and oxygen as a function of oxygen gas concentration, for both circular and linear polarized laser pulses. The incident pulse energy is 9.3 mJ.

In order to obtain practical 337 nm coherent emission source in atmospheric air, it is required to have enough population inversion density to overcome the quenching effect of oxygen molecules. One possible approach to achieve this goal is to use powerful pump laser at long wavelength, because the kinetic energy of electron born in strong laser field quadratically increases with the pump laser wavelength, e.g. $E_k \approx I\lambda^2$. Another possible approach is that we first use powerful nanosecond pump laser to dissociate oxygen molecules in order to reduce the influence of dissociative quenching effect of oxygen molecules and then launch the second circularly polarized near-infrared laser in air to generate backward 337 nm lasing emission.

2.5 Temporal profile of 337 nm lasing pulse from filament plasma

2.5.1 Introduction

In previous sections we have demonstrated for the first time the observation of 337 nm lasing emission from neutral nitrogen molecules in filament plasma, which is created by focusing 800 nm circularly polarized pump laser pulses in pure nitrogen gas or ambient

air. We have characterized this 337 nm lasing emission through spectra, spatial profile, polarization, divergence and pump energy dependence. The forward 337 nm nitrogen ASE is much stronger than the backward one, showing pronounced asymmetry. This is regrettable since the backward lasing is particularly useful for long distance atmospheric diagnostics. It is therefore important to understand in detail the origin of this asymmetry in order to envision strategies allowing backward lasing in air.

To this purpose, we have measured the temporal dynamics of the ASE at 337 nm wavelength in a filament plasma, both in the forward and backward direction. Significant difference in pulse duration is observed. We first shows experiment results of temporal profiles of both forward and backward 337 nm ASE pulse. A short summary will end up this section.

2.5.2 Experiment results of forward 337 nm lasing pulse

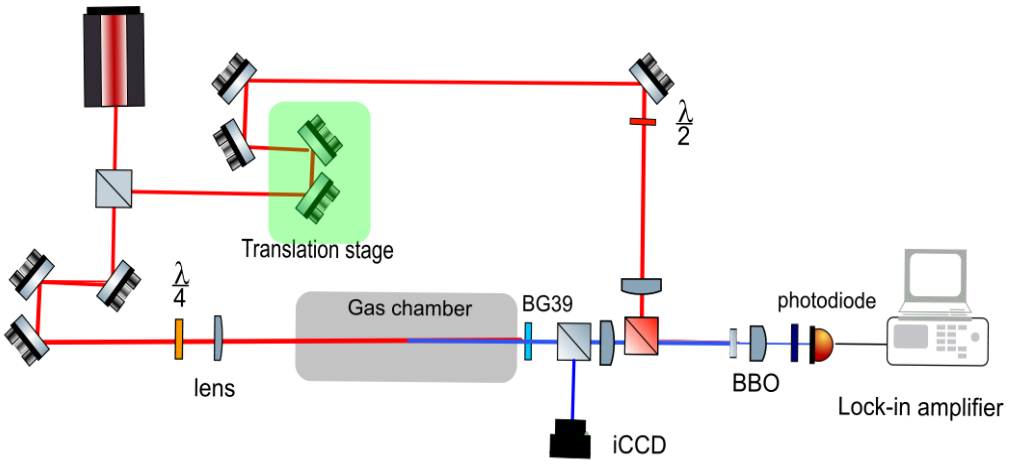

Figure 2.17: Schematic illustration of experimental setup for measuring the temporal profiles of forward 337 nm lasing emission. $\lambda/4$ and $\lambda/2$ denote quarter and half wave plate, respectively.

We first introduce the experimental setup. Figure 2.17 shows the schematic illustration of the cross-correlation method, which is modified based on previous setup shown in Fig. 2.4. Briefly, the cross-correlation method exploits shorter pulse to measure the temporal profile of longer pulse via nonlinear process such as generating sum-frequency signal in a BBO crystal. A probe beam is introduced by a first beamsplitter, which reflects 10% of incident laser power. It first pass through a time delay line (TDL) formed by a pair of mirrors fixed on an electric-controlled translation stage. A half wave plate is inserted in probe arm to change its direction of linear polarization. By using a dichromatic mirror, the 800 nm probe pulse is combined with the forward 337 nm lasing pulse

into a 2-mm-thick type-I BBO crystal cut specially at 50.7°, to efficiently produce a sum frequency generation (SFG) signal at 240 nm wavelength. By recording the sum frequency signal at 240 nm as a function of the time delay between the 337 nm lasing signal and the weak 800 nm probe pulse, the temporal profile of the 337 nm lasing pulse can be obtained.

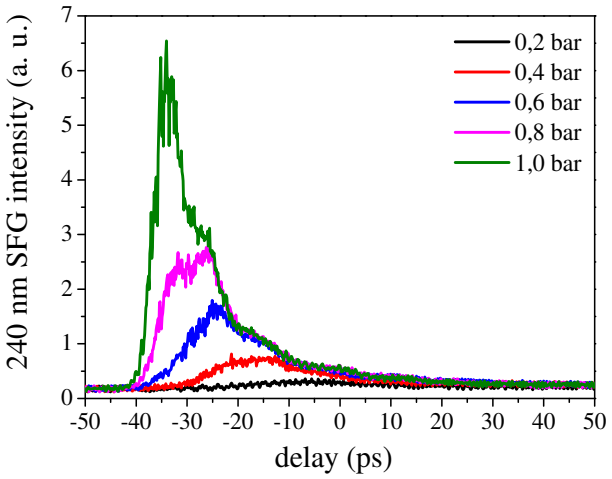

Figure 2.18: Measured temporal profiles of forward 337 nm ASE at nitrogen pressures ranging from 0.2 bar to 1.0 bar.

Figure 2.18 shows the measured temporal profiles of forward 337 nm ASE lasing pulses for nitrogen gas pressures ranging from 0.2 bar to 1.0 bar. In the measurements, the circularly polarized pump laser with pulse energy of ∼10.0 mJ was focused by $f = 1\ m$ convex lens into nitrogen gas chamber, and it generated about 6-cm-long filament plasma under 1.0 bar pressure. The general observation is that the forward 337 nm ASE lasing pulse become shorter and stronger with the increase of nitrogen pressure. Under 0.4 bar pressure, the pulse duration can be estimated as ∼25 ps, whereas the pulse duration reduces down to ∼10 ps under 1.0 bar nitrogen. Note that there exists very weak periodic structures, for instance the result under 1.0 bar pressure. The temporal profile of forward 337 nm ASE under 0.8 bar clearly shows two peaks. In next chapter, we will show that these weak periodic structures on temporal profiles of forward 337 nm ASE pulse is originated from quantum beating effect between triple fine transitions of $C^3\Pi_u^+(v' = 0) \rightarrow B^3\Pi_g^+(v = 0)$, which will be more significant in external seeding scheme.

2.5.3 Experiment results of backward 337 nm lasing emission pulse

The backward 337 nm ASE lasing signal is too weak to be measured by the cross-correlation method. We therefore turned to a Michelson interferometer to estimate its

pulse duration by measuring the interference fringe visibility between two 337 nm ASE pulse replicas as a function of their relative delay.

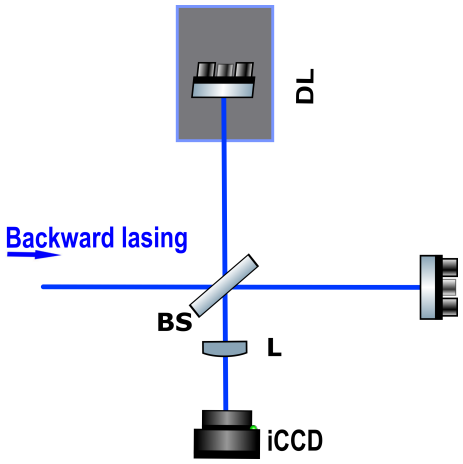

Figure 2.19: Schematic illustration of Michelson interferometer for measuring the interference pattern of backward 337 nm lasing emission. BS denotes a beamsplitter with a thickness of 500μm. DL is a time delay line controlled by a motorized stage. L is a 10 cm fused silica lens for collecting the light to iCCD camera.

The experimental setup of Michelson interferometer is shown in Fig. 2.19. The interference pattern of 337 nm lasing beam was captured by an iCCD (Princeton Instrument, PI-MAX). By adjusting the delay between the two beams to obtain the temporal overlap (0 ps), we observe an interference pattern with few vertical fringes as shown in Fig. 2.20. When the two arms was separated much longer, by 100 ps for example, the fringe visibility becomes poor because of partial temporal overlap.

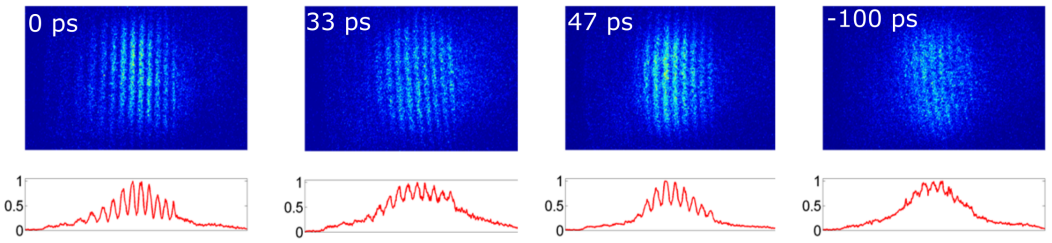

Figure 2.20: Interference pattern of backward 337 nm ASE lasing pulse for time delay of 0 ps, 33 ps, 47 ps and -100 ps. Vertical fringes were observed because we elaborately set a small angle between two identical arms of incident 337 nm ASE. The red curve shows normalized integrated intensity along vertical direction.

The fringe visibility V, given by

$$V = (I_{max} - I_{min})/(I_{max} + I_{min})$$

where I_{max} and I_{min} are respectively the maximum and minimum intensities, measures the coherence of light source. For each fringe pattern at certain time delay, we choose the

central peak to calculate its visibility. To confirm the validation of this autocorrelation method for measuring the temporal profiles of 337 nm ASE pulse, we also measured the temporal profile of forward 337 nm ASE pulse. Figure 2.21 shows the fringe visibility

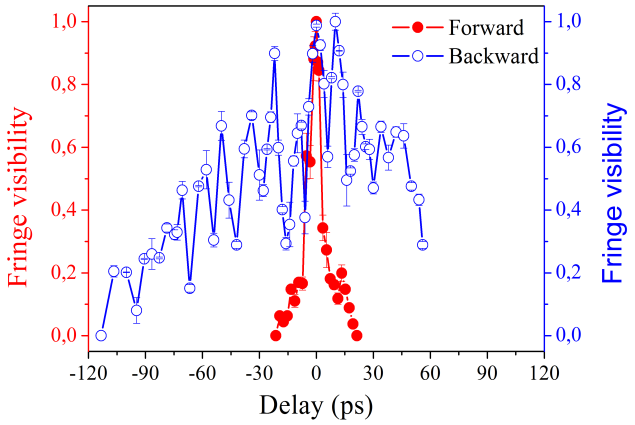

Figure 2.21: Fringe visibility of both forward and backward 337 nm ASE lasing as a function of time delay between two identical arms in Michelson Interferometer. The measurement in positive delay range is incomplete because of setup limitation.

of both forward and backward 337 nm ASE lasing as a function of time delay. Based on that, we can obtain that the coherence time of forward 337 nm ASE pulse is ∼20 ps. By assuming the ASE pulse as a transform-limited Gaussian-shaped pulse, its pulse duration can be estimated as ∼15 ps. It is in good agreement with the result obtained by using cross-correlation method (∼10 ps), validating the autocorrelation method is suitable to measure the backward lasing pulse. The measured result of backward 337 nm ASE pulse shows very long coherence time with a half width about 120 ps. Therefore, the pulse duration of backward 337 nm ASE is approximately 85 ps assuming a Gaussian temporal shape, much longer than forward ASE. The backward 337 nm ASE has high coherence about 0.72 (zero delay). In addition, the fringe visibility as a function of delay shows strong oscillation with a period of 11 ps, which is attributed to quantum beating effect. It will be in detail discussed in the case of externally-seeding configuration in next chapter.

2.5.4 Conclusion

In conclusion, we have performed experimental measurements of the temporal dynamics of the bidirectional 337 nm ASE-type lasing pulse from filament plasma in nitrogen gas pumped by circularly polarized femtosecond laser pulses. The 337 nm ASE pulse in the backward direction has a pulse duration around 85 ps, much longer than that the forward one (10 ps) and a much weaker peak intensity, showing profound asymmetry.

2.6 Summary

In this chapter, we presented the observation of a bidirectional lasing emission at 337 nm wavelength, from few-centimeter-long, $100 \sim 200\mu m$ -wide filament plasma (plasma density $\sim 10^{16}\ cm^{-3}$ under 1 bar gas pressure) which is created by focusing circularly-polarized 800 nm femtosecond laser pulse (45 fs pulse duration, 100 Hz repetition rate, pulse energy up to 14 mJ) in pure nitrogen or ambient air. This 337 nm lasing emission corresponds to the $C^3\Pi_u^+(\upsilon' = 0) \rightarrow B^3\Pi_g^+(\upsilon = 0, 1)$ transition of excited neutral nitrogen molecule.

We have characterized it through measuring the spectrum, spatial profile, temporal waveform, beam divergence, polarization, pump energy dependence, nitrogen pressure dependence and the dependence on pump laser polarization, for both in forward and backward directions. One of main features of the 337 nm lasing emission is that the lasing intensity in forward direction is 3 orders of magnitude stronger than that in backward direction. The spectrum of 337 nm lasing emission shows a narrower line width compared to fluorescence. The forward 337 nm lasing beam has a donut shape but backward one shows a central-maximum distribution. Both have a small divergence about 10 mrad, showing high directionality. The measurement on the polarization of lasing pulse shows that it is non-polarized, indicating this kind of stimulated emission intrinsically is ASE. For both forward and backward 337 nm ASE, the pump energy threshold is around 4 mJ with $f = 1\ m$ focusing geometry. It is worthy to mention that the lasing intensity polynomial depends on nitrogen gas pressure ranging from 0.4 bar to our limit 2.0 bar, and therefore one can expect stronger lasing intensity with higher pressure.

The temporal profile of forward 337 nm ASE pulse was measured by cross-correlation method while that of backward one was estimated by indirect way, in which the interference fringe visibility of backward ASE as a function of time delay gives the coherence time and duration by assuming its waveform. The forward 337 nm ASE has a pulse duration (FWHM) of $\sim 10\ ps$ whereas the backward ASE has a much longer duration of $\sim 85\ ps$ under the condition of 1 bar nitrogen pressure and $\sim$10 mJ pump laser energy. Remind that the lasing intensity in forward direction is much stronger than that in backward.

Backward 337 nm lasing emission is particularly interesting because of potential application in atmospheric remote sensing. Unfortunately, the quenching effect of oxygen molecules results in much weaker forward 377 nm lasing in air than in pure nitrogen, by a factor of ~ 200. In backward direction, ASE-type 337 nm lasing has not yet been observed in ambient air. To obtain practical 337 nm coherent emission source in atmospheric air, it is then required to have higher population inversion density to overcome the quenching

effect of oxygen molecules. One possible approach to achieve this goal is to use powerful pump laser at long wavelength. Another possible approach is that we first use powerful nanosecond pump laser to dissociate oxygen molecules in order to reduce the influence of dissociative quenching effect of oxygen molecules and then launch the second circularly polarized near-infrared laser in air to generate backward 337 nm lasing emission.

Chapter 3

Externally-Seeded 337 nm Lasing in Femtosecond Filaments

Contents

In the previous chapter, we have reported the observation of bidirectional 337 nm ASE from few-centimeter-long, 100 $\sim$ 200μm -wide filament plasma in nitrogen gas pumped by circularly polarized 800 nm femtosecond laser pulse. In the presence of population inversion, by injecting an external seed pulse at corresponding wavelength into the gain medium, the emission should be significantly amplified. In this chapter, the externally-seeded 337 nm lasing emissions in both forward and backward directions will be investigated experimentally.

We first present that dramatically enhanced 337 nm lasing emission can be obtained in the presence of an weak seed pulse in both forward and backward directions. For the spatial profiles, the forward seeded 337 nm lasing beam has a donut-like shape similar to that of forward ASE while the backward seeded lasing beam shows a central-maximum mode. For the polarization, the seeded 337 nm lasing pulse inherits that of the incident seed pulse. The temporal profile measurements of seeded 337 nm lasing pulse show that it consists of the seed and a following wake pulse that composes of periodic structures due to quantum beats effect. Finally, by varying the time delay between the pump and seed pulses, the gain dynamics was characterized, which indicates electron collision excitation being the population inversion mechanism.

3.1 Forward externally-seeded 337 nm lasing emission

3.1.1 Experimental setup

The experiment setup for studying the forward seeded 337 nm lasing pulse is shown in Fig. 3.1, modified on the basis of setup shown in Fig. 2.17. In this setup, the second beamsplitter reflects 80% laser energy to the pump arm and transmit 20% to the seed arm. M1 and M2, two highly reflective mirrors, installed on the moving tracks, consist of a optical delay line. A quarter-waveplate was installed in the pump arm to change the polarization of the pump pulse. The pump pulse was focused by a $f = 1000$ mm lens into the gas chamber filled with nitrogen. In the seed arm, a BBO crystall was first installed to generate second harmonics around 400 nm. Then, the blue second harmonic was focused by a $f = 15\ cm$ fused silica lens into a bulk BK7 glass in order to generate down-converted white light covering the 337 nm wavelength range. As follows a bandwidth filter centered at 337 nm ($\sim$ 10 nm) was used to select light component around 337 nm. Afterwards, another $f = 15\ cm$ fused silica lens was used to collimate the divergent seed light. After reflection by M4, the seed pulse was focused by another silice lesn with $f = 50\ cm$, which was installed on a 3-dimensional translation stage in order to adjust the spatial overlap between the pump and seed pulse. A dichromatic mirror

(DM1), which reflects UV light and transmit infrared light, combine spatially the pump and seed pulses into the chamber. After the chamber, a BG39 filter was used to block the strong infrared light. The 337 nm lasing signal was focused by another silice lens with $f = 10\ cm$ to combine the 800 nm fundamental pulse to form the cross-correlation measurement setup.

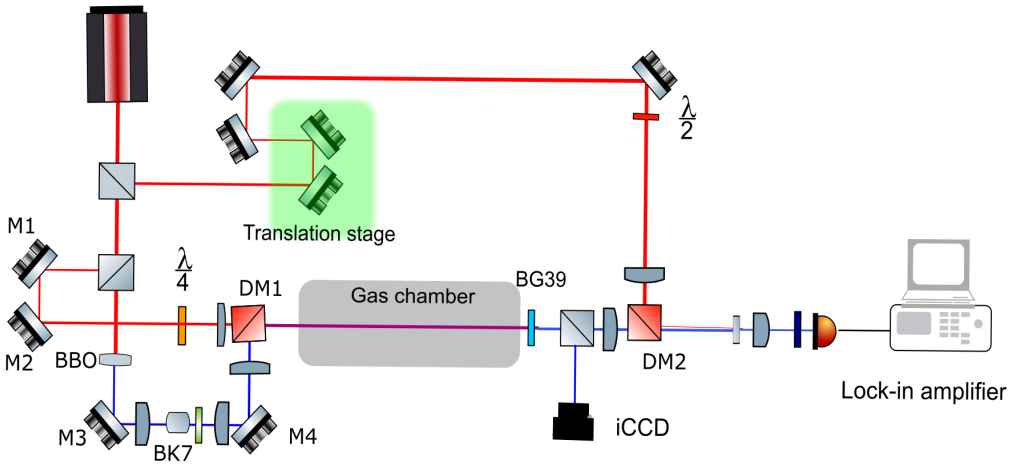

Figure 3.1: Schematic illustration of co-propagating configuration for measuring the gain dynamics and temporal profile of 337 nm lasing emission.

3.1.2 Characterization of forward seeded 337 nm lasing pulse

3.1.2.1 Spectra

During the experiments, the pump-seed time delay was kept at the position of ∼4 ps, where the maximum 337 nm lasing intensity was detected. The pump pulse is set to circular polarization, and the seed pulse is linearly polarized. Figure 3.2 shows the spectra of 337 nm lasing emission with and without the seed pulse, and the spectrum of the seed pulse. In the presence of an weak seed pulse, a significantly enhanced 337 nm emission was obtained, almost 7 times stronger than that without the seed pulse. Note that in this measurement the seed pulse has a broad bandwidth and its component at 337 nm wavelength is quite weak. In addition, the beam size of the seed at focus is 2∼3 times larger than the transverse size of filament plasma, which is typically $100 \sim 200\ \mu m$. By considering these two facts, we estimate the intensity ratio between the externally-seeded 337 nm lasing pulse and the seed pulse to be ~ 400.

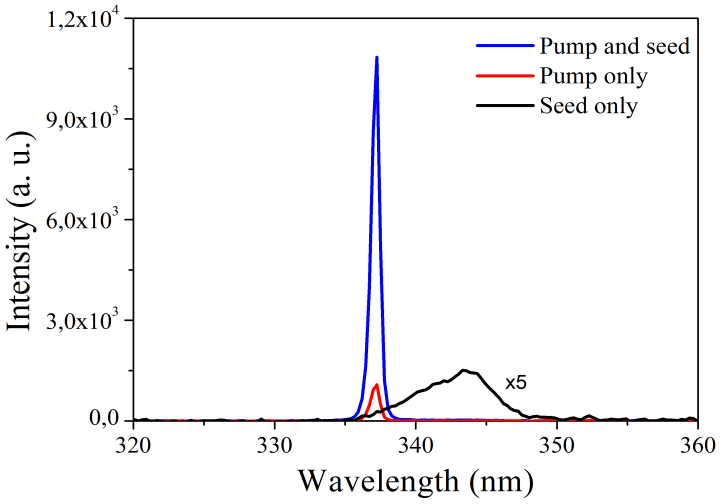

Figure 3.2: Spectra of forward externally-seeded 337 nm lasing emission, the forward 337 nm ASE and the seed pulse. The pump pulse energy is about 7.2 mJ. The intensity of seed pulse is magnified by 5 times for better vision.

3.1.2.2 Spatial profiles of the forward seeded lasing beam

We also measured the spatial profile of externally-seeded 337 nm lasing pulse by an iCCD camera, as shown in Fig. 3.3. We measured it at two different positions along the propagation direction to determine its divergence. The forward 337 nm ASE is directional and shows a donut shape with a divergenece of ∼20 mrad. With the almost uniformly distributed seed beam as shown in Fig. 3.3(b), the externally-seeded 337 nm lasing beam shows a donut-like shape, similar to that of 337 nm ASE. We notice that this donut shape is a common feature for different lasing effects of air plasma, including the 845 nm lasing from atomic oxygens [29], 337 nm lasing from neutral nitrogen molecules, as well as 391 nm lasing from nitrogen ions that will be discussed in Chapter 5. It is quite universal, indicating it stems from basic aspect of laser-plasma interaction. We speculate it is from an axicon-like transverse plasma distribution.

3.1.2.3 Seed intensity dependence

Figure 3.4 shows the seed intensity dependence of externally-seeded 337 nm lasing in forward direction. In this measurement, we used photodiode to detect the lasing signal. The seed intensity was controlled by rotating a continuously-varying attenuator. The relative delay between the pump pulse and the seed pulse was adjusted by moving the translation stage to the case where the maximum lasing emission was recorded. One can see that the forward externally-seeded lasing intensity monotonously increases with the

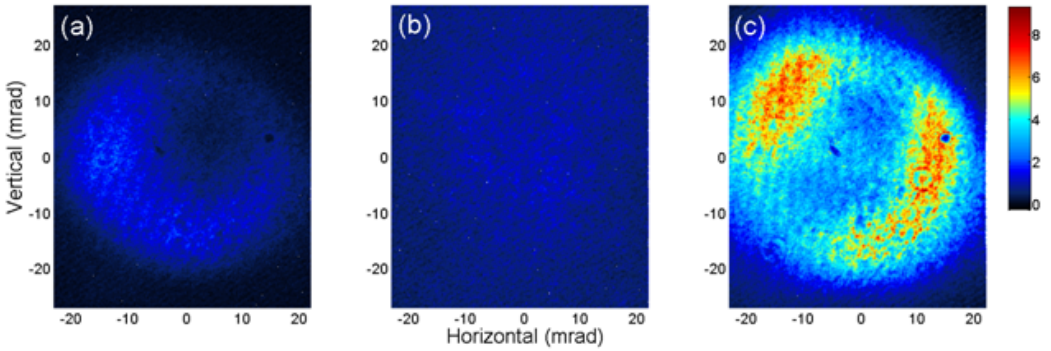

Figure 3.3: Measured spatial profiles of forward 337 nm ASE (a), seed pulse (b) and externally-seeded 337 nm lasing pulse (c) in pure nitrogen gas with pump pulse energy of ~9.0 mJ.

seed intensity, and then saturates until $\sim 10\ mV$. This indicates that laser amplification reaches the saturation regime for relatively strong seeding pulse.

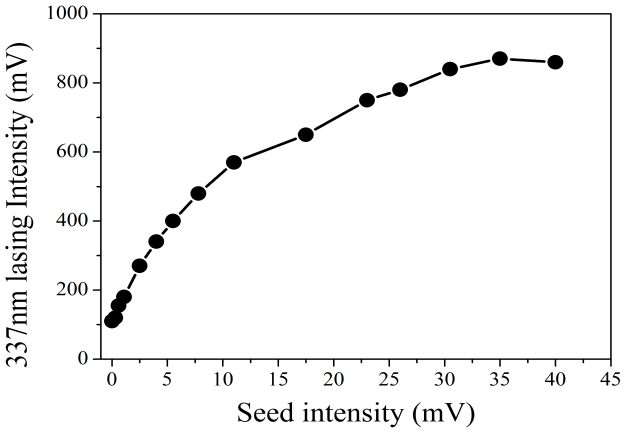

Figure 3.4: The forward externally-seeded 337 nm lasing intensity as a function of the seed intensity. The pump pulse energy was kept as 7.2 mJ.

3.1.3 Temporal profile of forward seeded 337 nm lasing pulse

The experiment setup to measure the temporal profile of forward 337 nm lasing pulse has been shown in Fig. 3.1. Several experiments has been performed to address different aspects of temporal dynamics of forward externally-seeded 337 nm lasing emission.

In the first experiment, we used $f = 50\ cm$ convex lens to focus pump laser with pulse energy of $\sim 9\ mJ$, which induced ~3-cm-long filament plasma in 1 bar nitrogen gas. The temporal profile of the seed pulse is shown in Figure 3.5 where the zero is defined as the peak position of the seed pulse. The pulse width (FWHM) of the seed pulse can be estimated as 0.85 ps. The temporal profile of seeded 337 nm lasing emission clearly

shows two peaks in time domain, in which the first one is the seed pulse. Its intensity doesn't change much compare to that without pump laser. The external injection of seed pulse leads to the generation and amplification of a wake pulse. It develops in time very after the seed pulse. The duration of the wake pulse is about 3.4 ps, and the wake reaches peak after ~ 6 ps with respect to the seed pulse. Note that the most energy of seeded 337.1 nm lasing emission contains in the wake pulse.

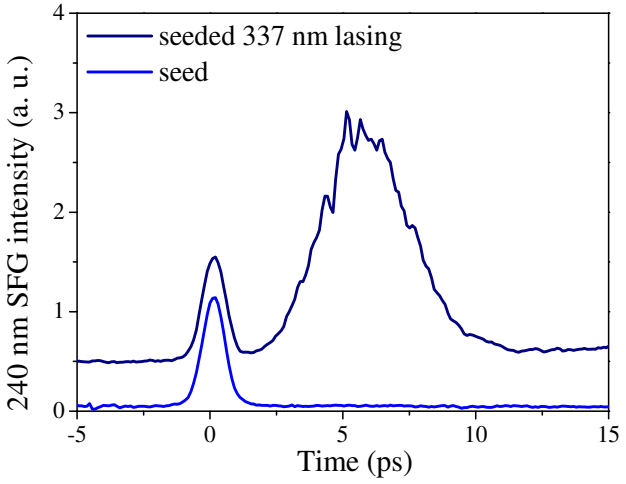

Figure 3.5: Temporal profiles of seed pulse and externally-seeded 337 nm lasing pulse measured with cross-correlation method. Before detector, we used BG40 and UG11 filters to block the IR pump light, and 240 nm bandwidth filter to select the sum-frequency signal.

The seeded 337 nm lasing emission is highly similar with the plasma-based soft-X-ray lasers seeded by high-order harmonics [32, 33]. The duration (~ 1 ps) of the seed pulse is much shorter than the time scale of the atomic response of the lasing molecules determined by electron-molecule elastic and nonelastic collisions. This time scale mismatch leads to a long wake following the seed pulse due to the long-lasting polarization of the plasma by the seed pulse. The amplification of a short pulse in plasma is an intrinsically dynamic process which can be numerically solved only through a fully time-dependent treatment of the atomic polarization density. The qualitative explanation and numerical simulation about it will be in details addressed later in the simulation part.

We also studied the effect of the seeding time on the temporal profile of seeded lasing pulse, as shown in Fig. 3.6. In this experiment, we varies the relative delay between the seed and the pump ranging from -2.0 ps to 5.0 ps through a delay line in the pump beam. The zero of relative delay corresponds to the case where the maximal seeded 337 nm lasing emission is detected, e.g. the peak of gain dynamics (see Fig. 3.11), and the positive delay means the seed pulse is behind the pump pulse. When the delay changes

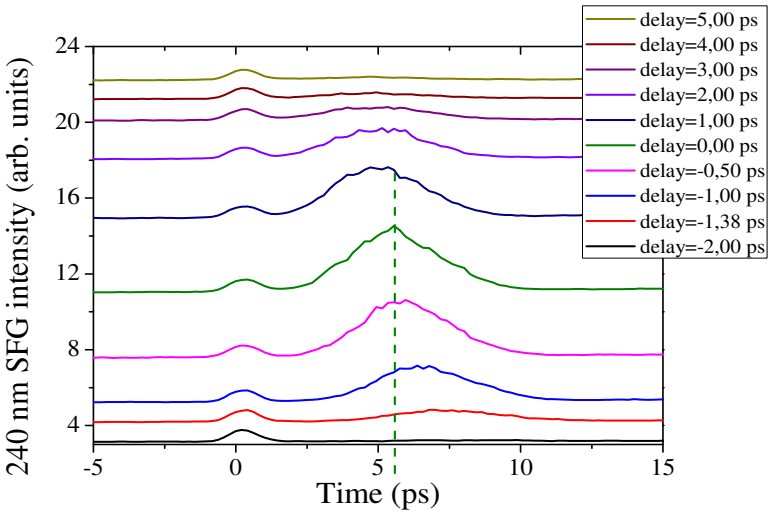

Figure 3.6: Temporal profiles of forward externally-seeded 337 nm lasing pulse for different delays between the IR pump and the seed pulse. The green dashed line denotes the peak position of the wake pulse in the case of zero delay.

from $-2.0\ ps$ to zero, the wake moves towards the seed and becomes stronger. It behaves oppositely for positive delays. When the delay changes from zero to 3 ps, the intensity of wake pulse decreases continuously.

Figure 3.7 shows the results of the temporal profiles of forward seeded 337 nm lasing pulse measured at different nitrogen gas pressures, ranging from 0.2 bar to 1.0 bar. In the experiment, the pump pulse energy has been set to 11.1 mJ, and we used $f = 1$ m convex lens to focus the pump beam into gas chamber. The seed beam size at focus was estimated as ∼1 mm while filament transverse size is about 0.2 mm. The zero time corresponds to the peak position of seed pulse, which is barely seen because strong wake generation. First feature is that the wake pulse becomes stronger and shorter in duration when the nitrogen pressures increases from 0.2 bar to 1.0 bar. In addition, its peaks moves more close to the zero time, e.g., the delay with respect to the seed pulse gets shorter.

Another feature is quite obvious, e.g. the wake pulse shows oscillating temporal structures, which is quite periodic. For example, the result at 1 bar pressure shows three peaks positioning at ∼7 ps, ∼17 ps and ∼29 ps, respectively. Note that the first feature is also valid for the second peak for each curve, e.g., the peak moves towards the zero with the increase of nitrogen pressure. The typical result at 0.6 bar pressure and corresponding Fast Fourier Transform (FFT) result are shown in Fig. 3.8. The oscillating temporal structure is quite significant. By transforming it to the frequency domain, we can obtain a small peak at 0.095 THz that corresponds to a period of 11 ps. Please note that the temporal profile of forward 337 nm ASE pulse (see Fig. 2.18) also shows very weak periodic temporal structures.

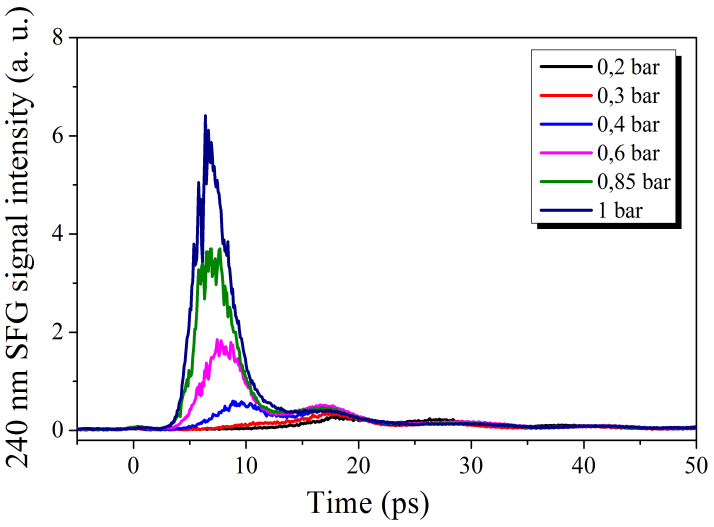

Figure 3.7: Temporal profiles of forward externally-seeded 337 nm lasing pulse for different nitrogen pressures.

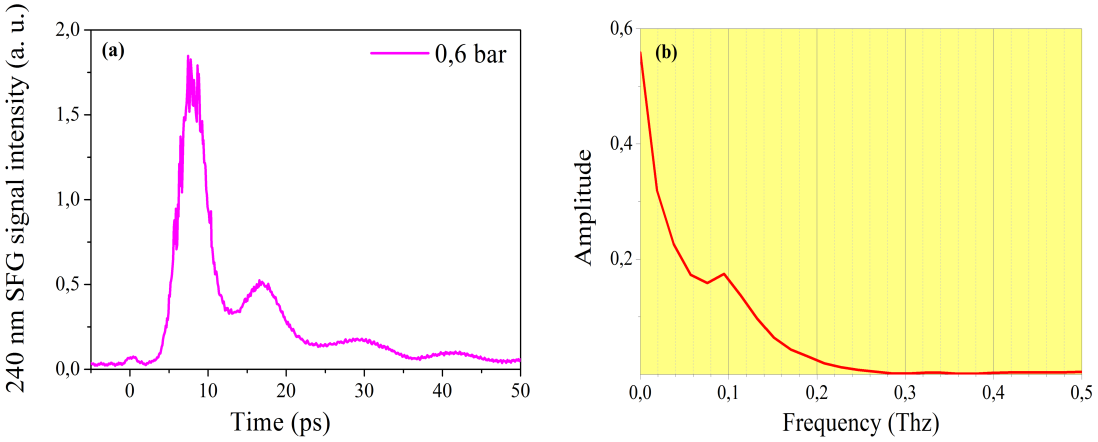

Figure 3.8: Measured temporal profile (a) of forward seeded 337 nm lasing pulse at 0.6 bar nitrogen pressure. (b) the corresponding FFT transformation.

What is the origin of the temporal modulation of the 337 nm lasing? We found clues about it in literatures. It has been confirmed in traditional discharge pumped nitrogen laser that the lasing line at 337 nm, corresponding to the P branch of the $C^3\Pi_u^+(v' = 0) \rightarrow B^3\Pi_g^+(v = 0)$ transition of excited neutral nitrogen molecule, is composed of three finely separated branches P_1, P_2 and P_3, due to the interaction between orbital angular momenta and spin [34, 35], shown in Fig. 3.9. The separation between these fine branches is about 0.33 $A_\circ$, which is beyond the resolution of our spectrometer. Furthermore, superfine separation of ~ 0.05 $A_\circ$ inside P_1 has been observed in literatures. We suggest the fast collisional excitation process brings the molecules into a coherent superposition of the three branches. An intensity modulation in the temporal domain

is then expected due to quantum beating between them. The corresponding temporal modulation period T can be expressed as

$$T = \frac{\lambda_0^2}{c\Delta\lambda}, \tag{3.1}$$

where $\lambda_0 = 337\ nm$ is the central wavelength of lasing emission, and $\Delta\lambda = 0.033\ nm$ (0.005 nm for superfine separation) is the wavelength separation of three branches. Therefore, we can obtain $T = 11.5\ ps$, in good agreement with the experiment result. For superfine separation of 0.005 nm, it corresponds to a temporal modulation period ~75 ps. This modulation has been also observed in temporal profile measurement of backward seeded 337 nm lasing emission, which will be presented later.

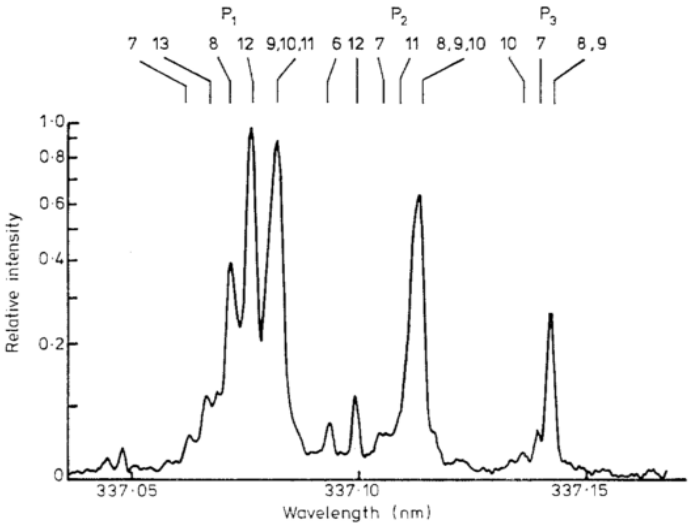

Figure 3.9: Fine spectrum of 337 nm $C^3\Pi_u^+(\upsilon' = 0) \rightarrow B^3\Pi_g^+(\upsilon = 0)$ transition consisting of P_1, P_2 and P_3 branches. Courtesy to the reference [34].

We also measured the temporal profiles of forward seeded 337 nm lasing pulse generated in ambient air. In the experiment, the pulse energy of circularly polarized pump laser was set to 11.2 mJ, and it was focused by $f = 50\ cm$ lens. The linear seed pulse was focused by another $f = 50\ cm$ fused silica lens and the size of seed beam at focus is about 1 mm. The result is shown in Fig. 3.10. It is quite similar with the result obtained in 1 bar nitrogen, and also shows temporal structure due to quantum beats effect. The wake pulse gives a width of 3.7 ps, delayed by $\sim 5\ ps$ with respect to zero.

In short summary of this subsection, we have experimentally investigated the temporal profiles of forward seeded 337 nm lasing pulse. The injection of an external seed pulse leads to the generation and amplification of a wake pulse instead of amplification of the seed pulse itself. The measurements of temporal profiles of the wake pulse at different pressures shows that higher gas pressure lead to narrower pulse, higher peak intensity,

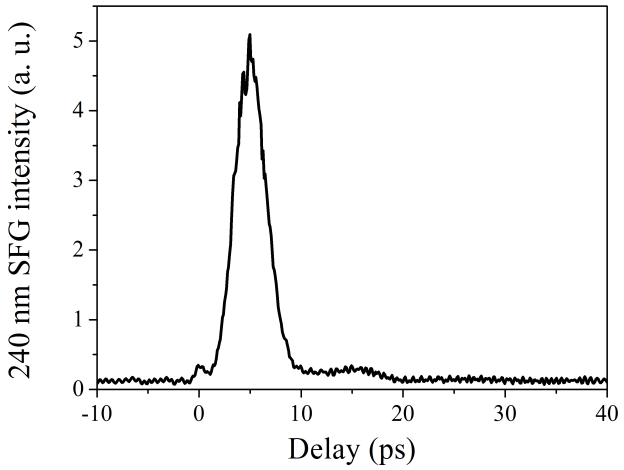

Figure 3.10: The temporal profile of forward seeded 337 nm lasing pulse in ambient air measured through cross-correlation method.

and shorter delay time with respect to the pump pulse. The wake pulse shows periodic temporal structures due to quantum beats effect, which becomes more significant at lower pressure.

3.2 Gain dynamics of 337 nm lasing emission

The temporal dynamics of the gain is a very important aspect of an optical amplifier. In the co-propagation configuration of the pump and seed pulse, we can obtain the gain dynamics of 337 nm lasing emission by changing the relative delay between them and recording the 337 nm signal. The setup for this measurement has been shown in Fig. 3.1. Figure 3.11 shows the results of gain dynamics for three different nitrogen gas pressures. The zero time delay is defined as the position where noticeable 337 nm lasing intensity exceeds that of the seeding pulse. For 1 bar nitrogen pressure, a gain built-up time of ~4 ps and a decay process of ~20 ps are observed. For lower gas pressures of 600 and 400 mbar, the gain built-up times increase to 7 and 11 ps respectively. This dependence of the gain built-up time on the gas pressure indicates the collision excitation as the origin of population inversion between the $C^3\Pi_u^+(\upsilon' = 0)$ and $B^3\Pi_g^+(\upsilon = 0)$ states of the neutral nitrogen molecule. Note that for 1 bar gas pressure the maximum amplified 337 nm lasing intensity reaches to ~850 mV, compare to which the maximum amplified 337 nm lasing intensity dramatically decrease to 100 mV (20 mV) for 600 mbar (400 mbar) gas pressure. It means higher optical gain can be obtained under higher gas pressure when other experimental parameters keep constant, which is consistent with the result in Fig. 2.13, where forward 337 nm ASE intensity monotonously increases with gas pressure.

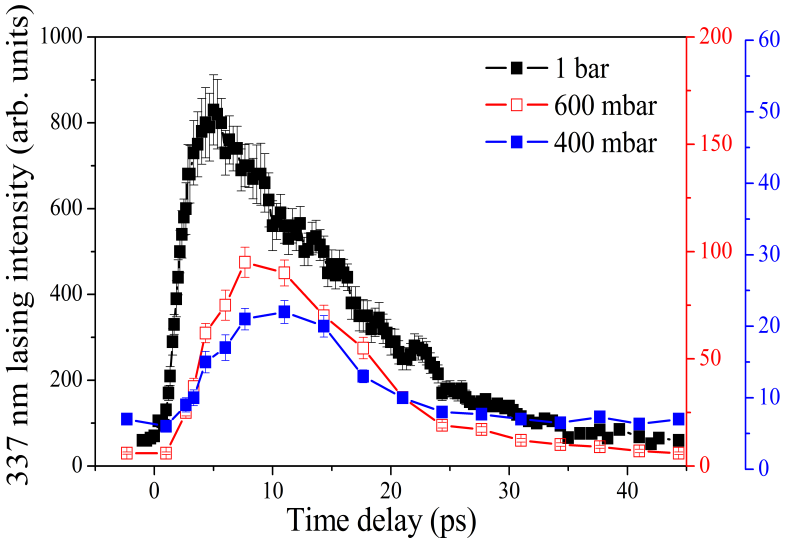

Figure 3.11: Measured forward amplified 337 nm lasing signal as a function of the relative time delay between the pump and seeding pulse. The pump pulse energy was 7.5 mJ and the focal length is 1 m.

From this result, we can estimate effective gain length $l_{eff} = c\tau_g$ where c the light speed in vacuum and τ_g the gain lifetime. For 1 bar gas pressure with 1 m focal length, $\tau_g \sim 15\ ps$ and therefore $l_{eff} \sim 4.5\ mm$. It is much smaller than the filament plasma length of ~6 cm.

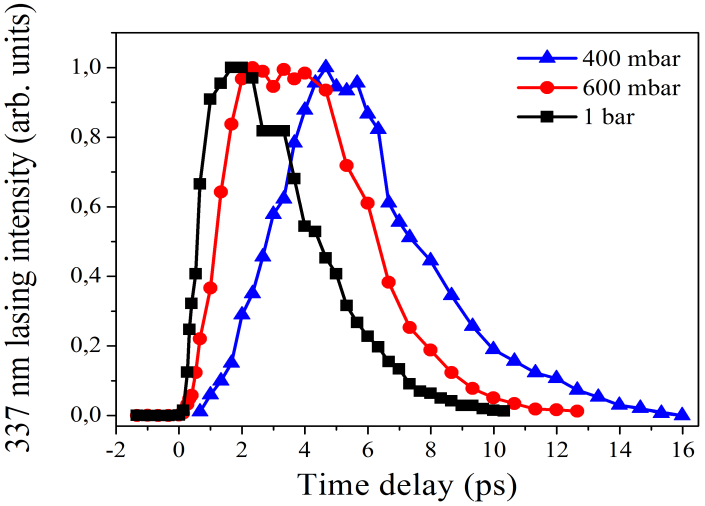

Figure 3.12: Measured forward amplified 337 nm lasing signal as a function of the relative time delay between the pump and seeding pulse. The focal length is 50 cm.

We also measured the gain dynamics for a more tightly focused pump pulse. Figure 3.12 shows the gain dynamics results of 337 nm lasing under 1 bar, 600 mbar and 400 mbar gas pressures with 50 cm focal length. Similar to the results in Fig. 3.11, shorter gain built-up time is obtained under higher gas pressure. For instance, under 1

bar pressure the gain built-up time is ∼2 ps, twice shorter than that in the case of 1 m focal length. For 1 bar gas pressure, the gain lifetime is about 4 ps. By decreasing the gas pressure to 600 mbar (400 mbar), the gain lifetime becomes ∼5 ps (5 ps). So it is clear that with shorter focal length, the gain built-up become faster and the gain lifetime also get shorter. These results can be understood qualitatively as follows: when we use shorter focal length without changing other experimental parameters, such as pump pulse energy, the pump pulse would generate a more dense filament plasma due to higher laser intensity. This leads to faster gain buildup and shorter gain lifetime.

3.3 Backward externally-seeded 337 nm lasing emission

In this section, we investigate the backward 337 nm lasing emission in the presence of a backward-propagating external seed pulse. First, the experimental setup will be briefly introduced. Then, we characterized the backward seeded 337 nm lasing emission by measuring its spectra, polarization dependence on that of seed pulse, spatial profiles, seed pulse energy dependence.

3.3.1 Experimental setup

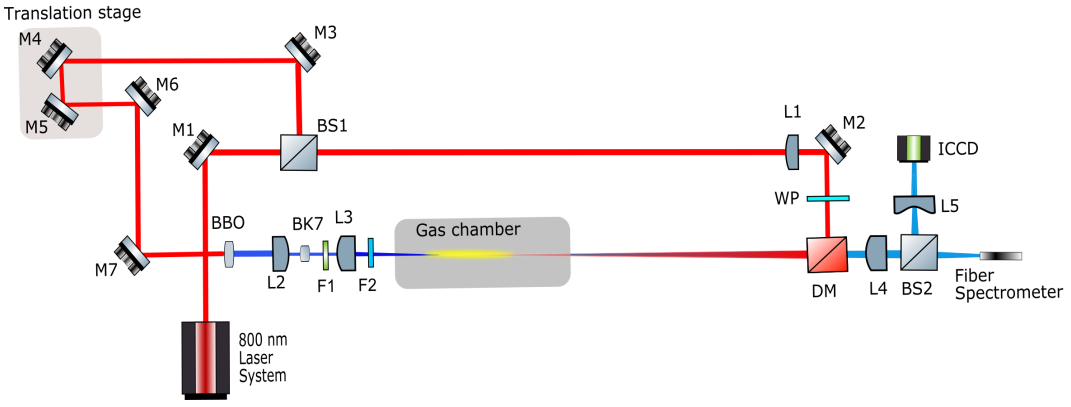

Figure 3.13: The schematic illustration of experimental setup for backward seeded 337 nm lasing emission.

In order to introduce a backward-propagating seed pulse, the femtosecond pulse from our laser system was split into a main pump pulse and a much weaker second pulse by a 1 mm thick 5%/95% beamsplitter. The pump pulse passes through a quarter waveplate and is then focused by an f = 1000 mm convex lens (L1). A dichromatic mirror was used to reflect the focused 800 nm pump pulses into a gas chamber filled with pure nitrogen gas a 1 bar pressure. This dichromatic mirror reflects more than 99% of the 800 nm pump pulse and it is transparent for the backward ultraviolet emission from

the laser plasma situated inside the gas chamber. The second weaker 800 nm pulse first passes through a mechanical delay line and then a 1 mm thick type-I BBO crystal in order to generate femtosecond pulses at 400 nm. The 400 nm pulses is linearly polarized in the vertically direction. The obtained 400 nm pulses is further focused by an f = 200 mm convex lens (L2) inside a 20 mm long fused silica sample to broaden its spectrum through intense nonlinear propagation. We selected the spectrum component around 337 nm with an interference bandpass filter, which has a transmission peak at 340 nm and a bandwidth of 10 nm. The resulting pulse centered at 340 nm, referred to as seeding pulse in the following, was focused by another f = 100 mm lens (L3) into the gas chamber from the opposite direction of the pump pulses. The separation between the lenses L2 and L3 was adjusted to insure that the geometrical focus of the seeding pulse overlaps with the central part the of the long plasma filament in the longitudinal direction. The transverse spatial overlapping between the geometrical focus of the seeding pulse and the center of the plasma filament was carefully assured by translating finely L3 in the transverse plane. The temporal delay between the 800 nm pump pulses and the seeding pulse at 337 nm can be adjusted by the mechanical delay line.

For some of our experiments, we installed a quarter waveplate (WP) for 400 nm after the BBO crystal, where circularly polarized seeding pulse can be obtained after filamentation inside the fused silica sample. The backward emission from the laser plasma filaments was collected by a f = 100 mm silica lens (L4) and detected by either a spectrometer (Ocean Optics HR 4000), an intensified Charge Coupled Camera (Princeton Instrument, model: PI-MAX), or a calibrated photodiode.

3.3.2 Characterization of backward seeded 337 nm lasing pulse

3.3.2.1 Spectra measurement

The spectra of backward 337 nm emission in the presence of a backward-propagating seed pulse are presented in Fig. 3.14. Considering the intensity of the seed pulse at the 337 nm spectral position, we estimated that the seed pulse is amplified by a factor of ~200 times (Fig. 3.14(a)). Compare to the backward ASE intensity, the seeded 337 nm lasing emission intensity is 40 times higher. With the effective amplifier length of 0.45 cm as estimated before, we calculated the small-signal gain coefficient to be $g = ln(I_f/I_0)/l_{eff} = 11.8\ cm^{-1}$. Here, I_f, I_0, l_{eff} are the intensity of the amplified 337 nm emission, the intensity of the seed pulse, and the effective length of the plasma amplifier. The population inversion density is then estimated as $\delta n = g/\sigma_s \sim 10^{15}\ cm^{-3}$, where $\sigma_s \sim 10^{-14}\ cm^2$ is the stimulated cross-section of the $C^3\Pi_u^+(\upsilon' = 0) \rightarrow B^3\Pi_g^+(\upsilon = 0)$ transition. In the case of linearly polarized pump pulses (Fig. 3.14(b)), no detectable ASE

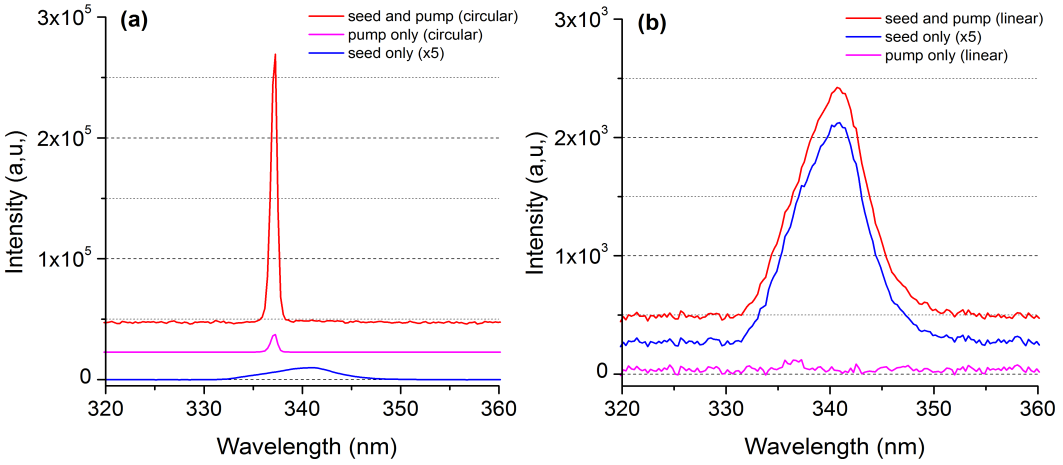

Figure 3.14: Spectra of the backward emission with circularly (a) and linearly (b) polarized pump pulsed at 800 nm. The spectra of the seed pulses and those of the backward emission from the pump pulses are also presented for comparison. The spectrum of the seed pulse is magnified by a factor of 5 for better comparison.

and no amplification of the seed pulse could be observed, which indicates the absence of optical gain at 337 nm transition.

3.3.2.2 Spatial profiles of seeded 337 nm lasing pulse

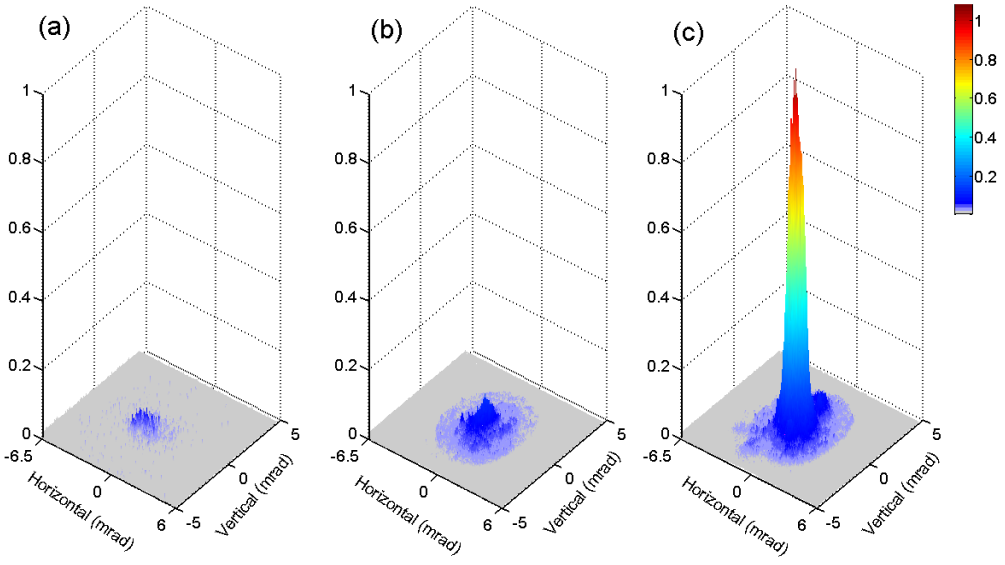

Figure 3.15: Spatial profile of the backward ASE (a), the seed pulse (b), and the externally-seeded 337 nm emission (c). The opening angle of each panel is 12.5 $mrad \times$ 10.0 $mrad$. The color bar indicates the normalized emission intensity.

We also measured the spatial profiles of the seeded 337 nm lasing emission with the iCCD camera. Figure. 3.15(a) is the spatial profile of the backward ASE, the same

with Fig. 2.7(b). We present the spatial profile of the seed pulse in Fig. 3.15(b). In the presence of circular pump and linear seed pulse, an intense 337 nm emission was observed, as presented in Fig. 3.15(c).

This seeded 337 nm lasing emission shows a center-maximum distribution with a divergence angle of $\sim$ 3.8 *mrad*, smaller than that of the ASE and the seed pulse. Compare to the spatial profiles of forward 337 nm ASE and seeded 337 nm lasing emission beam shown in Fig. 3.3, we can notice two differences: (1) The spatial profiles in forward direction show donut shape, whereas that in backward direction is center-maximum-shaped; (2) The beam divergence in forward direction is larger than that in backward direction.

3.3.2.3 Polarization of seeded 337 nm lasing pulse

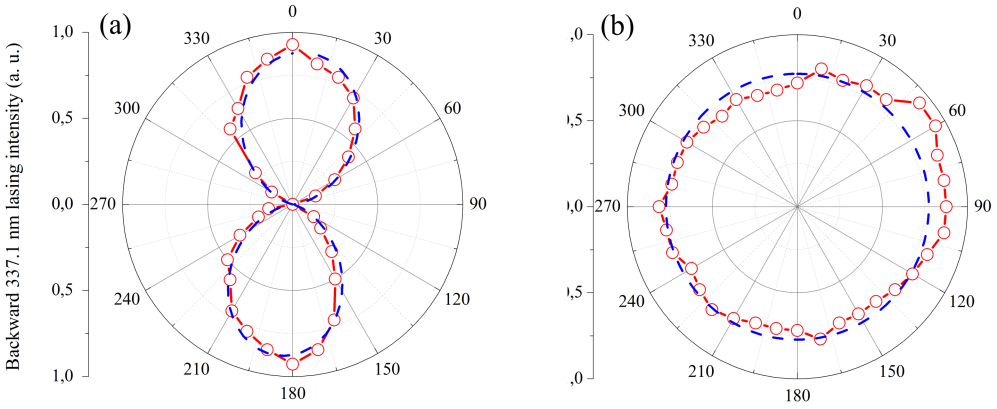

Figure 3.16: Polarization of the seeded backward stimulated emission with linearly (a) and circularly (b) polarized seed pulses at 337 nm. The dots present the experimental results and the dashed lines denote the theoretical fitting with Malus' law.

In order to identify the dependence of polarization of seeded 337 nm lasing pulse on that of seed pulse, we used a Glan-Taylor prism as the analyzer before the detecting photodiode. According to the Malus' law, when linearly polarized light is incident on the analyzer, the intensity I of the light transmitted by the analyzer is directly proportional to the square of the cosine of angle θ between the transmission axes of the analyzer and the polarizer, e.g.,

$$I \propto \cos^2 \theta.$$

For linearly polarized seed pulses in the vertical direction, we observed that the seeded 337 nm lasing signal shows a 8-like-shape dependence on the rotating angle of analyzer (see Fig. 3.16(a)). It means linear polarization in vertical direction, evidenced by the

good agreement between the experimental results and the theoretical fit with Malus' law, as shown by the dashed curve.

The result for circularly polarized seed pulses is presented in Fig. 3.16(b), where the seeded 337 nm lasing pulse possess the same polarization. To summary, in both two cases, the seeded 337 nm lasing pulse has same polarization state with the incident seed pulse. As discussed before, the injection of an external seed pulse leads to generation and amplification of a wake pulse, rather than the seed amplification in which case one can expect that the seeded output naturally has the same polarization with the seed pulse. In our case, we believe that the seed pulse creates a macroscopic polarization along its propagation in gain medium rather than the pump pulse, which should have same direction with the oscillation direction of the electric field of the seed pulse. Therefore, the polarization of wake pulse maintains that of seed pulse.

3.3.2.4 Seed pulse energy dependence

In order to determine whether the seed amplification is in the saturated regime, we varied the intensity of the seed pulse with a variable metallic optical density. The seed pulse energy was measured to be less than 1 nJ and we estimated its absolute value with a calibrated photodiode. We consider the beam size of the seed is larger than the transverse size of filament size. We therefore calculated the effective energy of seeded lasing pulse by subtracting that of seed pulse . Figure 3.17 presents the calibrated results. We fitted the experiment results with linear function. It shows the backward seeded 337

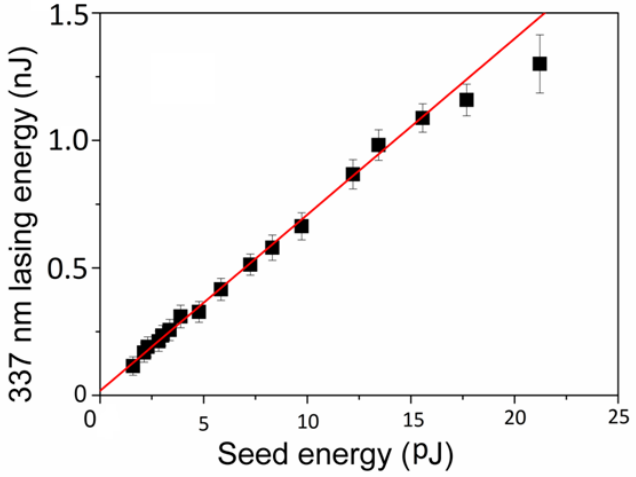

Figure 3.17: The calibrated seeded 337 nm lasing pulse energy in the backward direction as a function of the seed pulse energy. The red line curve denotes linear fit.

nm lasing energy linearly depends on the seed pulse energies within the range from 1

pJ to 15 pJ, which can be considered as the small-signal amplification regime. The maximum output of the backward seeded 337 nm lasing pulse was measured to be 1.2 nJ under the experimental conditions. This output pulse energy corresponds to energy conversion efficiency of 1.4×10^{-7} from 8.5 mJ pump pulse. Therefore, the pulse energy of the ASE was deduced to be ~ 0.03 nJ based on the enhancement factor of 40, which gives a conversion efficiency of 3.5×10^{-9}.

In summary of this subsection, we have investigated the backward 337 nm lasing emission in the presence of a weak seed pulse propagating in backward direction by charactering its spectra, polarization state dependence on the seed pulse, spatial profile and pulse energy dependence on the seed pulse energy. In the presence of external seed pulse, the backward 337 nm lasing emission can be dramatically enhanced compare to ASE. For the polarization of seeded 337 nm lasing pulse, it has the same polarization with the seed pulse. In addition, the divergence of seeded 337 nm lasing beam is smaller compare to that of ASE, and keeps the central-maximum mode. With increased seed pulse energy, the seeded 337 nm lasing pulse energies linearly increase in small-signal amplification regime until the seed pulse energy reaches to 15 pJ. Under the experimental conditions of 8.5 mJ pump pulse energy, 1-m focal length and 1 bar nitrogen gas, we can get the maximum 337 nm lasing pulse energy of ~1.2 nJ.

3.3.3 Temporal dynamics of backward seeded 337 nm lasing pulse

In order to measure the temporal profiles of backward seeded 337 nm lasing pulse, we used the cross-correlation method. Based on the setup shown in Fig. 3.13, we combined it with a cross-correlation setup in which the 337 nm lasing pulse and 800 nm fundamental pulse (FWHM width ~45 fs) are overlapped spatio-temporally in a BBO crystal to generate sum-frequency light at 240 nm wavelength (see section 2.5). By recording the 240 nm signal as a function of relative delay between the 337 nm lasing pulse and the fundamental pulse, the temporal profile of the 337 nm lasing pulse will be recorded.

In the experiment, we focused circularly polarized pump laser with pulse energy of ~13 mJ with a $f = 1\ m$ convex lens into nitrogen gas under 1 bar pressure, and a sensitive spectrometer was used to collect the 240 nm SFG signal. Figure 3.18 shows the results of temporal profile of backward seeded 337 nm lasing pulse and that of seed pulse. It is clear that the intensity of seed pulse barely changes in the generation of backward seeded lasing pulse compare to the case of only seed pulse, e.g., the seed pulse is not amplified when it pass through the gain medium. It was ascribed to the fact that there exists a linewidth mismatch between the seed pulse and the 337 nm transition. Instead,

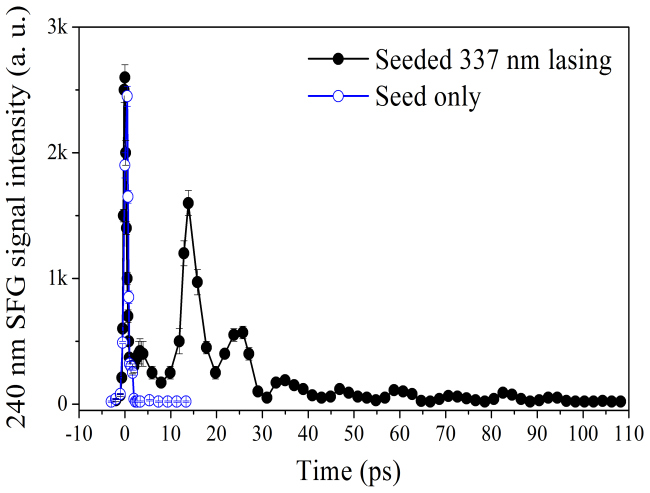

Figure 3.18: The measured results of the temporal profile of backward 337 nm signal in the cases of with circular pump (e.g., seeded 337 nm lasing) and without pump (e.g., only seed pulse). The 240 nm SFG singal is measured by a spectrometer.

the injection of seed pulse triggers a wake following it closely. The explanation of the wake creation can refer to the sub-subsection 4.2.3.

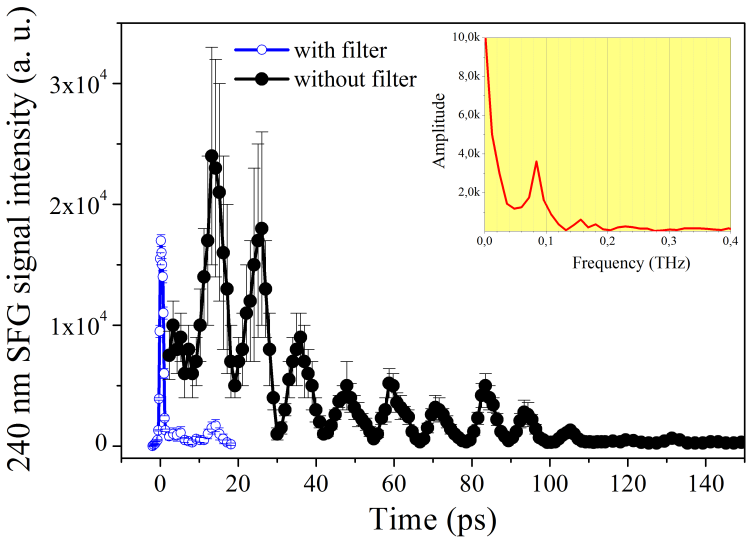

Figure 3.19: The measured results of the temporal profile of backward seeded 337 nm lasing pulse for two cases, with and without 240 nm bandwidth (∼10 nm) filter. The inset is the FFT result of the black curve obtained without filter.

Surprisingly, the wake pulse shows more significant temporal modulation due to quantum beats compare to the case of forward seeded 337 nm lasing pulse. In addition, it lasts for ∼100 ps. Figure 3.19 shows another similar result of more significant temporal modulation structures. By implementing the fast Fourier transform (FFT) of the temporal profile curve obtained without 240 nm bandwidth filter, we can observe a

peak at 0.09 THz in frequency domain that corresponds to 11 ps in time domain. It is consistent with the aforementioned result of forward seeded 337 nm lasing pulse(see Fig. 3.8). Thus both the forward and backward seeded 337 nm lasing pulses have a temporal profile with periodic modulation due to quantum beats effect. And furthermore, it is reasonable to expect that the 337 nm ASE-type lasing pulse has same feature when the gain is large enough. Recalling the results shown in Fig. 2.18, they do show fuzzy temporal modulations. The results of backward 337 nm ASE pulse measured by interferometer show strong modulation of fringe visibility as a function of delay (see Fig. 2.21), evidencing more significant quantum beats effect. In forward direction, competition between different lines of lasing emission exists because optical amplification reached saturation regime. Therefore, one of these lines dominates over others, manifesting weak periodic modulation. In contrast, in backward direction, different lines of lasing emission can be amplified almost equivalently in the small signal regime. Thus, the lasing emission presents much stronger temporal modulation.

In short summary of this subsection, we have measured the temporal profiles of backward seeded 337 nm lasing pulse by cross-correlation method. The injection of an external seed pulse in backward direction leads to generation and amplification of a wake pulse with significant temporal modulation due to quantum beats effect. The temporal modulation is much deeper than that in forward direction and it lasts for ∼100 ps.

3.4 Summary

In this chapter, we have studied the 337 nm lasing emission in external-seeded configuration in both forward and backward directions. A dramatically enhanced 337 nm lasing emission can be obtained in the presence of a weak seed pulse. For the spatial profiles, the forward seeded 337 nm lasing beam has a donut-like shape similar to that of forward ASE while the backward seeded lasing beam shows a central-maximum mode. For the polarization, the seeded 337 nm lasing pulse inherits it from the incident seed pulse.

By introducing a weak seed to probe the filament plasma, we studied gain dynamics of 337 nm lasing at different nitrogen pressures. It shows ultrafast gain built-up time and relatively slow decay. For instance, a gain built-up time $\sim$ 4 ps and a decay time of $\sim$ 20 ps are observed for 1 bar pressure. The dependence of gain built-up time on the gas pressure shows that the higher gas pressure leds to shorter gain built-up time, indicating the collision excitation as the origin of population inversion. From the gain lifetime result, we calculated the effective gain length, which is in fact much shorter than the geometric length of filament plasma. For 1 bar nitrogen gas pressure with 1 m focal

geometry, the gain lifetime is measured as ~ 15 ps and therefore we get the effective gain length as ~ 4.5 mm, while the filament plasma is 6 cm long.

The temporal profile measurements of seeded 337 nm lasing pulse show that it consists of the seed and a following wake pulse that composes of periodic structures due to quantum beats effect. To inject an external seed pulse is only to polarize the gain medium, e.g., to create a macroscopic polarization inside the gain medium, which leads to a wake pulse following the seed pulse.

Chapter 4

Interpretation of 337 nm Lasing Effect in Femtosecond Filaments

Contents

In the above two chapters, we have presented the experimental results as to the lasing effect of neutral nitrogen molecules inside femtosecond plasma filament. It has been show that ASE at 337 nm in both backward and forward directions can be observed with circularly polarized 800 nm femtosecond pump pulse. When an external seeding pulse is injected inside the plasma, the emission can be significantly enhanced. In this chapter, we will provide interpretation for these experimental results. Firstly, we will discuss the mechanism for population inversion. Then, we will present theoretical modeling for this lasing phenomenon based on a non-adiabatic Maxwell-Bloch equations. Numerical results for the gain dynamics and the temporal profile of the emission will be presented and compared with previous experimental results.

4.1 Physics mechanism of population inversion: electron collision excitation

Experimental observations implies that population inversion was established between the $C^3\Pi_u^+$ and $B^3\Pi_g^+$ states of the neutral N_2 molecules. What is the underlying mechanism of population inversion between these two states, at the origin of bidirectional 337 nm lasing emission ?

4.1.1 Proposed mechanisms

First, it is necessary to remind that a direct population transition between the ground singlet state $X^1\Sigma_g^+$ and the excited triplet $C^3\Pi_u^+$ state is forbidden in the electric dipole approximation, according to the selection rules of electronic transition of molecules.

In the literatures, we noticed that one widely proposed mechanism to populate the N_2 molecule to the $C^3\Pi_u^+$ state inside filament plasma is the following reaction [36]:

$$\begin{aligned} N_2^+ + N_2 &= N_4^+, \\ N_4^+ + e &= N_2(C^3\Pi_u^+) + N_2(X^1\Sigma_g^+). \end{aligned} \tag{4.1}$$

In this process, the $C^3\Pi_u^+$ state is populated by the dissociative recombination through the N_4^+ formation. With this mechanism, one can expect that a linearly polarized pump laser produces stronger lasing signal at 337 nm wavelength for the following two reasons: (1) Both in the multiple-photon ionization and tunneling ionization regimes, a linearly polarized pump laser induces a higher ionization rate of atoms or molecules rather than circularly polarized one [37]. As a result, the densities of free electrons and N_2^+ ions

should be higher with linearly polarized pump laser, and hence leads to more $N_2(C^3\Pi_u^+)$ compare to that with circularly polarized one. (2) The nonlinear refractive index of ambient air is higher for linearly polarized pump laser than that for circularly polarized pump laser. This fact results in slightly higher laser intensity inside filament plasma, which should additionally lead to higher densities of electrons and N_2^+ ions, and therefore $N_2(C^3\Pi_u^+)$. This mechanism could be responsible to the fluorescence result at low pump energies, for example that when the incident pump energy is about 300 μJ as shown in Fig. 2.9(a), where the 337 nm emission intensity is stronger with linear laser polarization. However, this mechanism fails to explain our lasing results with high pump energies. The experiment results clearly show that bidirectional stimulated emission at 337 nm wavelength critically depends on the polarization of pump laser. When the pump laser slightly deviated from circular polarization, the 337 nm lasing intensity decreases rapidly (see Fig. 2.9(c)).

In the literatures [38, 39], we found out the distribution of kinetic energies of electrons born in the intense laser field, strongly depends upon the pump laser polarization. With linearly polarized pump laser, free electrons are accelerated back and forth along the laser polarization direction at each optical cycle, so that at the end most of them have a low kinetic energy, with a weak tail distribution extending to a few eV. For circularly polarized pump laser, electrons are always accelerated away from the ion core, therefore the final electron distribution is nearly mono-kinetic with a peak at twice the ponderomotive energy U_p. In a linearly polarized laser field, U_p can be represented as

$$U_p = \frac{e^2}{c\epsilon_0 m_e} \times \frac{I}{2\omega_0^2} \tag{4.2}$$

where ϵ_0, m_e, ω_0, and I are respectively the vacuum permittivity, the mass of the electron, frequency of the laser field and the laser intensity. In our experiment, the laser intensity inside the filament plasma was obtained as 1.45×10^{14} W/cm^2 in the case of 9.3 mJ incident pump pulse energy [18]. Thus the peak of electron energy distribution should be around 16 eV according to Equation 4.2.

These facts guide us to another mechanism to explain the excitation transition from the ground state to the $C^3\Pi_u^+$ state: the electron-molecule inelastic collision process

$$N_2(X^1\Sigma_g^+) + e = N_2(C^3\Pi_u^+) + e. \tag{4.3}$$

This is actually the main reaction responsible for population inversion in a traditional N_2 laser, where the electrons are accelerated to obtain sufficient energy by the electric field of discharge [30]. The cross section of the above reaction is sensitive to the kinetic energy of the incident electron, shown in Fig. 4.1. It is nearly zero for electron energy below

the threshold kinetic energy $E_{th} \sim 12\ eV$, and exhibits a resonant peak around 14.5 eV, and then decreases progressively for higher energy electrons. The above calculation indicates that the electron energy required for impact excitation of neutral N_2 molecules is well reached in our case. For linearly polarized laser field, this mechanism is turned off because of the low electron kinetic energy, even with a laser intensity above the clamped value.

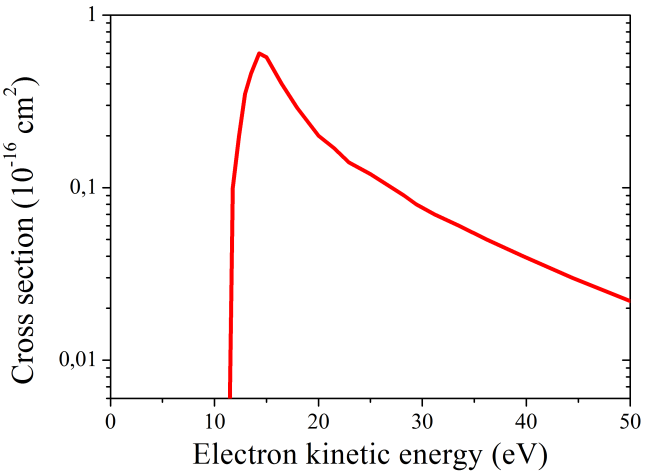

Figure 4.1: Cross-section of the electron-molecule inelastic collision excitation $N_2(X^1\Sigma_g^+) + e = N_2(C^3\Pi_u^+) + e$. Courtesy to the reference [40].

As a conclusion, we believe that the inversion of population inside the triplet manifold of N_2 is due to impact excitation by electron collisions. The threshold character for the inelastic collision cross section with respect to electron energy is reflected in the sharp dependence of the 337 nm lasing emission with pump ellipticity. The electron collision excitation mechanism also explains naturally the measured pressure dependence of the gain dynamics. With higher gas pressure, the electron-nitrogen collision becomes more frequent, leading to faster buildup of the population inversion as presented in Fig. 3.11.

4.1.2 Theoretical model

In order to solidify the proposed mechanism, our collaborator Prof. Arnaud Couairon in École Polytechnique has developed a theoretical model to simulate the distribution of electron energies in filament plasma, taking account into our experiment conditions.

4.1.2.1 Motion of an electron in an intense laser field

We solve the Newton equation for an electron with momentum $\mathbf{p}$, undergoing the effect of the Lorentz force:

$$\frac{d\mathbf{p}}{dt} = -q_e(\mathbf{E} + \mathbf{v} \times \mathbf{B}), \tag{4.4}$$

where $q_e > 0$ denotes the electron charge, and the electric and magnetic fields are expressed in terms of potential vectors $\mathbf{A}$, e.g.

$$\begin{aligned} \mathbf{E} &= -\frac{\partial \mathbf{A}}{\partial t}, \\ \mathbf{B} &= \nabla \times \mathbf{A}. \end{aligned} \tag{4.5}$$

The electric and magnetic field of the laser pulse are transverse. At first order, the electron is accelerated by the electric field in the transverse direction. At second order, the magnetic component of the Lorentz force coupling the transverse velocity with the transverse magnetic field will induce a longitudinal motion of the electron. The main contribution to the kinetic energy of an electron comes from the transverse acceleration, thus we consider only the transverse motion

$$\frac{d\mathbf{p}_\perp}{dt} = q_e \frac{\partial \mathbf{A}_\perp}{\partial t}. \tag{4.6}$$

Equation 4.6 can be readily integrated as

$$\mathbf{p}_\perp = \mathbf{p}_{\perp,0} + q_e(\mathbf{A}_\perp - \mathbf{A}_{\perp,0}). \tag{4.7}$$

We consider the electric field as the product of a consine envelope and a carrier wave, which reads in local frame ($\xi = z - ct$) as

$$\mathbf{E} = \begin{cases} E_0 \cos(\frac{\pi\xi}{Tc})[\cos(\frac{\omega_0\xi}{c} + \theta)\mathbf{u}_x + e\sin(\frac{\omega_0\xi}{c} + \theta)\mathbf{u}_y] \text{ for } & -T/2 < t < T/2 \\ 0 & otherwise, \end{cases}$$

where θ denotes an arbitrary carrier envelope phase and e represnts the ellipticity of the polarization. The vector potential reads

$$\mathbf{A} = \mathbf{A}_x\mathbf{u}_x + \mathbf{A}_y\mathbf{u}_y, \tag{4.8}$$

where $\mathbf{u}_x$ and $\mathbf{u}_y$ denote the units vector along the x and y directions, and

$$A_x = \frac{E_0}{\omega_0}\frac{1}{1-\pi^2/\omega_0^2T^2}[\cos(\frac{\pi\xi}{Tc})\sin(\frac{\omega_0\xi}{c}+\theta) - \frac{\pi}{T\omega_0}\sin(\frac{\pi\xi}{Tc})\cos(\frac{\omega_0\xi}{c}+\theta)] \tag{4.9}$$

$$A_y = -e\frac{E_0}{\omega_0}\frac{1}{1-\pi^2/\omega_0^2T^2}[\cos(\frac{\pi\xi}{Tc})\cos(\frac{\omega_0\xi}{c}+\theta) + \frac{\pi}{T\omega_0}\sin(\frac{\pi\xi}{Tc})\sin(\frac{\omega_0\xi}{c}+\theta)]. \tag{4.10}$$

By rewriting the potential vector in terms of amplitude and phase:

$$A_x = \mathcal{A}_\perp[\cos(u\phi)\sin(\phi+\theta) - u\sin(u\phi)\cos(\phi+\theta)] \tag{4.11}$$

$$A_y = -e\mathcal{A}_\perp[\cos(u\phi)\cos(\phi+\theta) + u\sin(u\phi)\sin(\phi+\theta)] \tag{4.12}$$

$$\mathcal{A}_\perp = \frac{E_0}{\omega_0}\frac{1}{1-u^2} \tag{4.13}$$

where $u \equiv \pi/T\omega_0$ and $\phi \equiv (\omega_0/c)\xi$.

4.1.2.2 Kinetic energy of an electron born in an elliptically polarized electric field

The kinetic energy of an electron, born at time t_0 when the phase $\phi = \phi_0$, after acceleration by the pulse, reads

$$E_k \sim \frac{p_\perp^2}{2m} = \frac{q_e^2}{2m}\mathcal{A}_{\perp,0}^2 \tag{4.14}$$

e.g.

$$\begin{aligned} E_k = &\frac{2U_p}{(1-u^2)^2}\{\cos^2(u\phi_0) + u^2\sin^2(u\phi_0) - (1-e^2)\times \\ &[cos(u\phi_0)cos(\phi_0+\theta) - u\sin(u\phi_0)sin(\phi_0+\theta)]^2\} \end{aligned} \tag{4.15}$$

where $U_p \equiv q_e^2E_0^2/4m\omega_0^2$ denotes the ponderomotive potential. For multiplecycle laser pulses with $T\omega_0 \gg 1$ and thus $u \ll 1$, it leads to the simplified version of Eq. 4.15

$$E_k = 2U_p\cos^2(u\phi_0)[1-(1-e^2)\cos^2(\phi_0+\theta)]. \tag{4.16}$$

We can retrieve that the maximum kinetic energy of the electron is $2U_p$ for a circularly polarized laser pulse ($e = 1$) when it is born at the peak of the field envelop ($\xi = 0$).

4.1.2.3 Ionization of molecules

In order to obtain the distribution of electron energies, we calculate the probability that electrons are born at a given instant t within the pulse. At peak intensities as

high as 10^{14} W/cm^2, optical field ionization is efficient enough to ionize most oxygen molecules at least once and part of nitrogen molecules. Here we consider first and second ionizations of oxygen and nitrogen molecules, described by the rate equations for the densities of molecules O_2, N_2 and ions O_2^+, N_2^+, O_2^{2+}, O_2^{2+}:

$$\frac{dn_{O_2}}{dt} = -W_{O_2}(\mid \mathbf{E}(t) \mid^2)n_{O_2} \tag{4.17}$$

$$\frac{dn_{O_2^+}}{dt} = W_{O_2}(\mid \mathbf{E}(t) \mid^2)n_{O_2} - W_{O_2^+}(\mid \mathbf{E}(t) \mid^2)n_{O_2^+} \tag{4.18}$$

$$\frac{dn_{O_2^{2+}}}{dt} = W_{O_2^+}(\mid \mathbf{E}(t) \mid^2)n_{O_2^+} \tag{4.19}$$

$$\frac{dn_{N_2}}{dt} = -W_{N_2}(\mid \mathbf{E}(t) \mid^2)n_{N_2} \tag{4.20}$$

$$\frac{dn_{N_2^+}}{dt} = W_{N_2}(\mid \mathbf{E}(t) \mid^2)n_{N_2} - W_{N_2^+}(\mid \mathbf{E}(t) \mid^2)n_{N_2^+} \tag{4.21}$$

$$\frac{dn_{N_2^{2+}}}{dt} = W_{N_2^+}(\mid \mathbf{E}(t) \mid^2)n_{N_2^+} \tag{4.22}$$

where the optical field ionization rates for oxygen and nitrogen molecules W_{O_2}, W_{N_2}, and those for ionization of ions $W_{O_2^+}$, $W_{N_2^+}$ are obtained from the general Keldysh-PPT theory. For the numerical resolution of the rate equations by using the electric field given by Eq. 4.8, where E_0 corresponds to an intensity I_0 (e.g. 1.4×10^{14} W/cm^2), we deduced the total electron density as

$$n_t(t) = n_{O_2^+} + 2n_{O_2^{2+}} + n_{N_2^+} + 2n_{N_2^{2+}}. \tag{4.23}$$

4.1.3 Numerical simulation of electron energy distribution

Figure 4.2 shows the ionization of air for a laser pulse with peak intensity of 10^{14} W/cm^2 and ellipticity $e = 1/3$. The total electron density reaches a few 10^{19} cm^{-3} and saturates before the peak intensity of the envelope is reached. We also note that the ionization probability exhibits bursts since the field polarization is close to linear, and the maxima of these bursts do not increase monotonically as the field amplitude increases. This is due to the occurrence of second ionization (generation of O_2^{2+} and N_2^{2+}) before the peak intensity of the pulse.

The probability that an electron be born at instant t_0 (between $t_0 + \Delta t/2$ and $t_0 - \Delta t/2$) within the pulse is

$$p_e(t_0) = \frac{\Delta t}{n_e(t_0)} \frac{dn_e}{dt}\bigg|_{t_0}. \tag{4.24}$$

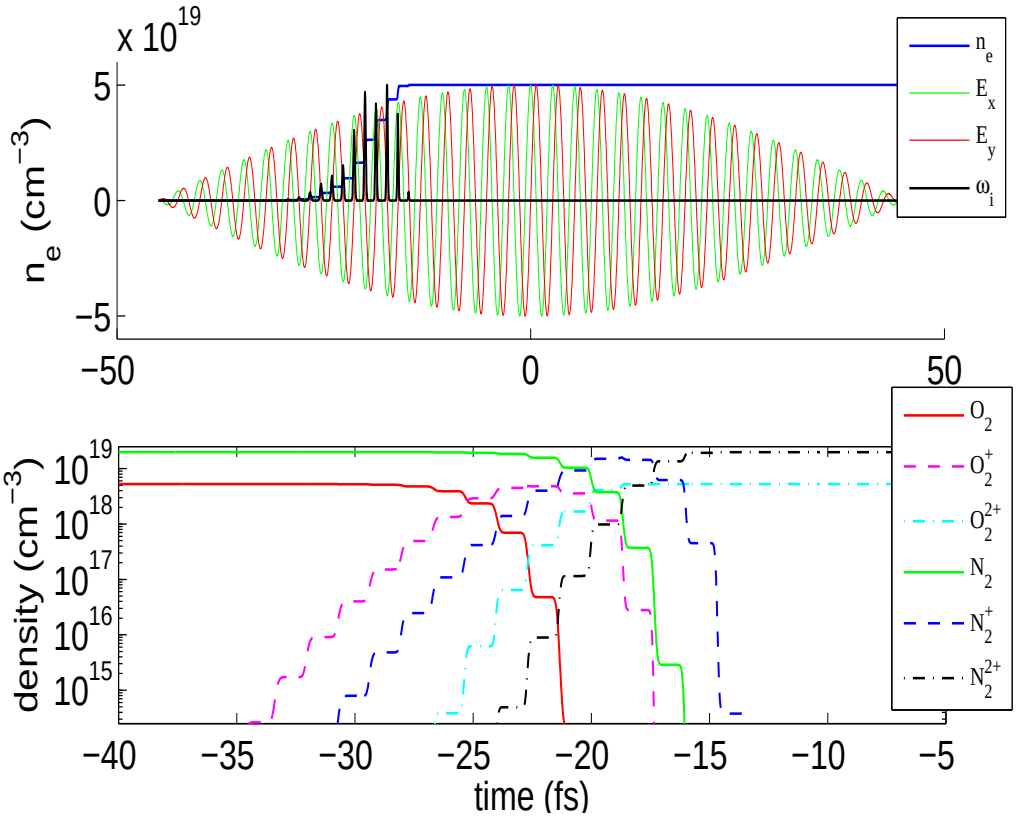

Figure 4.2: Ionization of air for a laser pulse with peak intensity of 10^{14} W/cm^2 and ellipticity $e = 1/3$. (a) Electron density (blue curve) and ionization probability ω_i in arbitrary unit (black curve). The component of the electric field E_x and E_y are superimposed as a guide for the eye to see the intant of ionization. (b) Densities of oxygen and nitrogen molecules, and ions.

Equation 4.15 for $E_k(t_0)$ and 4.24 constitute a parametric representation of the distribution of electron energies in the wake of the pulse due to the transverse acceleration by the laser pulse, with an arbitrary ellipticity e, duration T, peak intensity I_0 undergoing filamentation in air.

Figure 4.3 shows the result of the theory (Eqs. 4.15 and 4.24). This is compared to the result obtained by a direct numerical simulation of the motion of electrons by using Eq. 4.4 and the field equation 4.8, together with ionization rate equations (4.17). There is excellent agreement between theory and simulations. We note that the closer to circular polarization, the largest the number of electrons carrying kinetic energy approaching $2U_p$. The precise shape of the energy distribution depends on the ionization dynamics. The relative minimum close to 13 eV for the case of circular polarization is due to the fact that there is a potential gap between first and second ionization, leading to two humps in the probability $p_e(t)$ to generate the electrons. The different instant and intensities corresponding to these two humps lead to two maxima in the energy distribution.

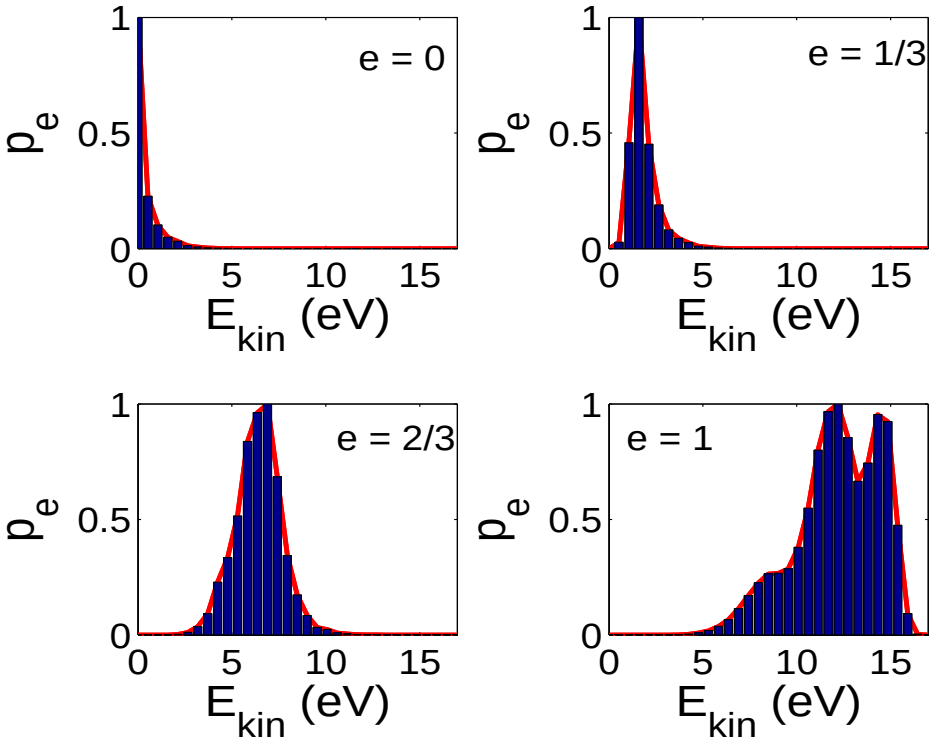

Figure 4.3: Distribution of kinetic energies for electrons generated by a laser pulse with peak intensity of 10^{14} W/cm^2 and ellipticity $e = 0$, $e = 1/3$, $e = 2/3$ and $e = 1$. The curves show the theoretical result. The blue bars show the result of a direct numerical simulation.

4.1.4 Conclusion

In conclusion, we proposed inelastic electron-molecule collision excitation as the underlying mechanism of population inversion for 337 nm stimulated emission of neutral nitrogen molecules in filament plasma, based on the fact that pump ellipticity plays a key role. The simulation results of kinetic energy distribution of electrons in filament clearly indicate that the kinetic energy of electron well reached the threshold of inelastic electron-molecule collision excitation process Eq. 4.3 with circularly polarized pump laser. It well explains the experiment observation that the 337 nm lasing emission critically depends on pump ellipticity and pressure dependence of gain dynamics.

4.2 Numerical simulation of lasing process

In previous section, we have explained the mechanism for population inversion. To understand this lasing effect inside the few-cm long filament plasma, theoretical modeling and numerical simulation are necessary, on which we have collaborated with Eduardo Oliva of Universidad Politécnica de Madrid (Spain) in the past 2 years.

4.2.1 Theoretical model

To numerically simulate the 337 nm lasing, we follow the lines of previous studies [41, 42] and adapt the one-dimensional time-dependent Maxwell-Bloch code Deep-One [33, 43] to our case. This code was originally developed to study the amplification of soft X-rays (λ=10-40 nm) in hot, dense plasma ($n_e > 10^{18}\ cm^{-3},\ T_e > 10 - 100\ eV$).

The propagation of an electric field is deduced from the following Maxwell wave equation in plasma:

$$\Delta\mathbf{E} - \frac{1}{c^2}\frac{\partial^2\mathbf{E}}{\partial t^2} - \frac{\omega_p^2}{c^2}\mathbf{E} = \mu_0\mathbf{P}, \tag{4.25}$$

where c is the light velocity in vacuum, ω_p is the plasma frequency, μ_0 is the vacuum permeability and $\mathbf{P}$ is the polarization density of the medium. In one-dimensional model, the transverse Laplacian is neglected, retaining only the derivatives on the z coordinate. The electric field can be written as $E_z = Re[Ee^{-i\omega_0 t+ikz}]$, where ω_0 is the frequency of the laser field and k is the wave number. Polarization can be expressed in a similar way. In the slowly varying envelope approximation, we assume that the second derivatives of the envelope function $E(z,t)$ can be neglected (first order in the case of polarization). Within this approximation, the paraxial wave equation is expressed as

$$\frac{\partial E_\pm}{\partial t} \pm c\frac{\partial E_\pm}{\partial z} = \frac{i\omega_0}{2}\left[\mu_0 c^2 P_\pm - \left(\frac{\omega_p}{\omega_0}\right)^2 E_\pm\right], \tag{4.26}$$

where E_+, E_- are the electric fields propagating in the forward and backward directions respectively, and P_+, P_- are the corresponding polarization density of the medium. Equation 4.26 describes the electric-field propagation through the plasma, amplification by the polarization density, and damping by the free-electron current. The polarization density is given by $\mathbf{P} = Tr(\rho\mathbf{d})$, where ρ is the density operator and $\mathbf{d}$ is the atomic electric dipole.

Equation 4.26 is enhanced with a constitutive relation derived from Bloch equations

$$\frac{\partial P_\pm}{\partial t} = \Gamma - \gamma P_\pm - \frac{iz_{ul}^2}{\hbar}E_\pm(N_u - N_l), \tag{4.27}$$

where Γ is a stochastic source term modeling the spontaneous emission [44, 45], γ is the depolarization rate due to collisions, z_{ul} is the corresponding dipole matrix element (that can be deduced from Einstein's A coefficient) and N_u, N_l are respectively the population of the upper and lower levels of the lasing transition. The Γ term is random variable with vanishing correlation function, properly normalized to obtain the expected Lorenzian lasing line profile. Since the seed duration (∼100 fs) is shorter than the typical collision time of the plasma (∼ ps), the adiabatic approximation is no more valid [32] and the full differential equation (equation 4.27) must be used to describe the evolution of the polarization. Finally, the populations of the transition levels involved in the lasing emission are computed by using the standard rate equations coupled with the electric field:

$$\frac{\partial N_i}{\partial t} = \sum_k C_{ki} N_k \pm \Im\left(E^* P\right) \frac{1}{2\hbar}, \tag{4.28}$$

where $i = u, l$ denotes the transition levels and C_{ki} coefficients include the collisional (de)excitation and radiative de-excitation rates. These rates are computed from the cross sections reported in [40]. The collisional excitation rates are dominated by electron-molecule collision excitations. The de-excitation rates are dominated by molecular collisions [41], and electron de-excitation contributions are negligible. The radiative de-excitation includes both spontaneous and collisionally induced radiative transitions but is dominated by molecular collisions. The set of Eqs. (4.26) - (4.28) are the Maxwell-Bloch equations.

The electron temperature T_e in femtosecond laser filamentation is given by [41]

$$\begin{aligned}(3/2)\frac{\partial(N_e T_e)}{\partial t} &= \langle \mathbf{J}\cdot\mathbf{E}_o\rangle - Q_c N_a N_e (1 - T_\nu/T_e),\\ (3/2) N_a \frac{\partial T_\nu}{\partial t} &= Q_c N_a N_e (1 - T_\nu/T_e),\end{aligned}$$

where $N_a = 2.5\times10^{19}\ cm^{-3}$ is the number density of nitrogen molecules, $N_e \sim 10^{16}\ cm^{-3}$ the electron density in filament plasma, $\langle \mathbf{J}\cdot\mathbf{E}_o\rangle$ is the Ohmic heating, Q_c is the cooling rate due to all inelastic collisions and T_ν is the nitrogen molecule's vibrational temperature. The cooling rate Q_c includes internal excitation of vibrational, rotational and electronic states of nitrogen molecules. At low kinetic energy of electron, the dominant inelastic cooling process is the excitation of vibrational states of nitrogen molecules. For $T_e < 2\ eV$, Q_c is given analytically by the following formula

$$Q_c \approx 3.5\times10^{-8}\exp(-5/3T_e) + 6.2\times10^{-11}\exp(-1/3T_e). \tag{4.29}$$

Since the initial electron temperature of 16 eV cools in less than 6 ps to a value lower than 2 eV, the value of Q_c is extrapolated for $T_e > 2\ eV$. The Ohimic heating rate is $\langle \mathbf{J}\cdot\mathbf{E}_o\rangle = (\omega_p^2/8\pi)E_{eff}^2/\nu_e$, where ν_e is the electron collision frequency, $E_{eff} =$

$(\nu_e/\omega_0)/(1+\nu_e^2/\omega_0^2)^{1/2}E_0$ is effective electric field, E_0 is the field amplitude of pump laser.

The evolution of electron density is computed by using the following formulas [41]:

$$\partial N_e/\partial t = \nu_{ion}N_e - \beta N_+ N_e - \eta N_e, \tag{4.30}$$

$$\partial N_-/\partial t = \eta N_e - \beta_{-+} N_+ N_-, \tag{4.31}$$

where ν_{ion} is the collisional ionization rate, β is the electron-ion recombination rate, β_{-+} is the ion recombination rate, η is the attachmentc coefficient, N_- is the negative ion density and $N_+ = N_e + N_-$. The collisional ionization rate can be calculated through

$$\nu_{ion} = \nu_{N_2}(T_e/U_{N_2})^{3/2}(U_{N_2}/T_e + 2)\exp(-U_{N_2}/T_e), \tag{4.32}$$

where the nitrogen molecule's ionization potential $U_{N_2} = 15.6\ eV$ and the molecule-electron collision frequency $\nu_{N_2} = 7.6 \times 10^{11}\ s^{-1}$. β is calculated by following approximations

$$\beta[cm^3/s] \approx 1.5 \times 10^{-8} T_e^{-0.7}, for\ T_e < 0.1\ eV \tag{4.33}$$

$$\beta[cm^3/s] \approx 2.0 \times 10^{-8} T_e^{-0.56}, for\ T_e > 0.1\ eV \tag{4.34}$$

and η is estimated as

$$\eta[s^{-1}] = \alpha_2 N + \alpha_3 N^2, \tag{4.35}$$

$$\alpha_2[cm^3/s] = 2.75 \times 10^{-10} T_e^{-0.5}\exp(-5/T_e), \tag{4.36}$$

$$\alpha_3[cm^3/s] = 1.5 \times 10^{-32} T_e^{-1}\exp(-0.052/T_e), \tag{4.37}$$

where $N = 2.7 \times 10^{19}\ cm^{-3}$ is the gas density. The temporal evolution of electron density and temperature is depicted in the following Fig. 4.4. The filament has an initial electron density of $N_e = 2 \times 10^{-16}\ cm^{-3}$ and initial electron temperature of $T_e = 16\ eV$. As shown in the figure, the free electrons cool in the first picoseconds of evolution, due to collisions with neutrals that are ionized. When the temperature is low enough, neither the ionization nor the collisional pumping are effective. The electron density decays due to recombination and the duration of the population inversion is given by the radiative decay of the upper level of the transition. The temporal resolution of level populations, combined with the stochastic treatment of the ASE, allows one to study several processes required to understand the ASE, the amplification of a weak seed in a plasma, such as Rabi oscillations and amplification of a noisy signal (ASE) mixed with the seed signal.

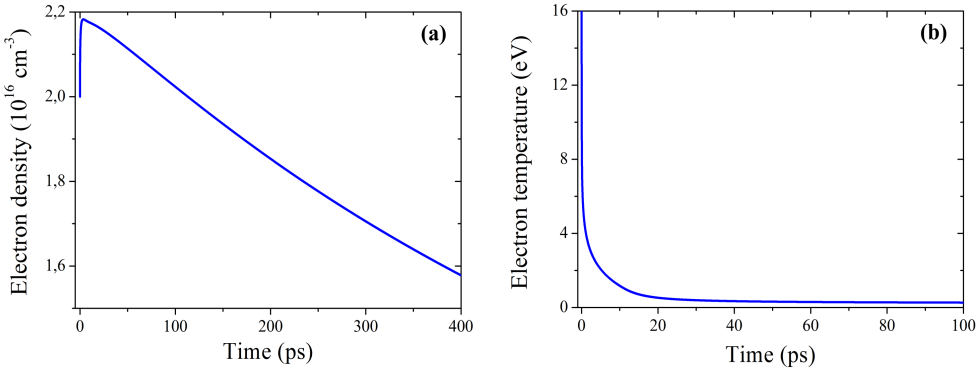

Figure 4.4: (a) Temporal evolution of the electron density along 400 ps. (b) Temporal evolution of the electron temperature along 100 ps.

4.2.2 Simulation results on temporal dynamics of bidirectional 337 nm ASE-type lasing pulse

In our simulation, we solve numerically the set of Eqs. (4.25) - (4.30) to get the gain dynamics and temporal evolution of 337 nm lasing pulse. To start numerical simulations, initial electron density and temperature are needed. For pump laser at $\lambda_0 = 0.8\ \mu m$ wavelength, the electron density N_e for normal neutral nitrogen density (such as 1 bar) varies in a large range from 10^{14} to $10^{17}\ cm^{-3}$, which crucially depends on the focusing conditions and pump laser power [46]. We choose $N_e = 1.0 \times 10^{16}\ cm^{-3}$ for 1 bar nitrogen pressure in our focusing condition of $f = 1000$ mm. The initial electron temperature is set to 16 eV for circular laser polarization according our previous research [47].

First we performed numerical simulation on the optical gain dynamics. As shown in Fig. 4.5, the simulation result agrees well with the experiment. It is now clear that the electron-nitrogen collision excitation results in a gain buildup time of 5 ps in our experimental conditions.

Fig. 4.6 shows the development of the forward 337 nm lasing emission along the filament plasma. The forward 337 nm ASE starts from noise spanning all the gain duration due to the long lifetime of the upper level of the transition $\tau_u \approx 40$ ns [48]. Stimulated emission rapidly dominates over the spontaneous emission at the very beginning of filament plasma. Amplification and saturation effects shorten its duration, accompanied by steepening of the leading front and therefore formation of an asymmetric pulse shape.

This steepening effect is caused by the fact that the leading front always encounters newly-formed population inversion part and experiences amplification, and therefore propagates at lower velocity than the peak and rear of the pulse which propagates in the part with depleted population inversion. After passing through 3 cm of plasma, the

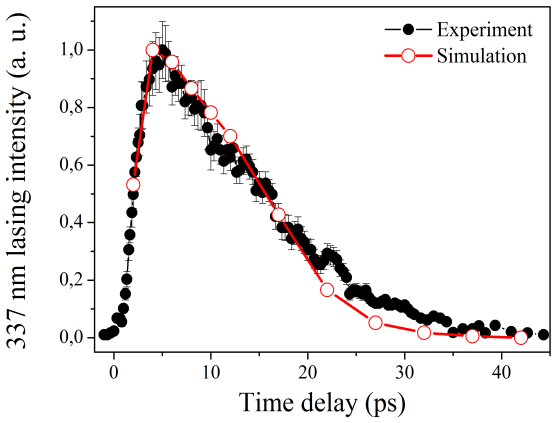

Figure 4.5: Experimental (solid black dots) and simulation (red circles) results of the gain dynamics of 337 nm lasing emission with 7.5 mJ pump pulse energy under 1 bar nitrogen gas.

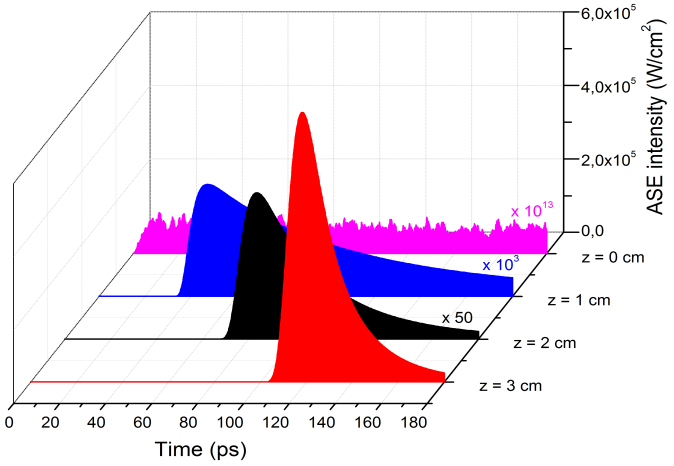

Figure 4.6: Simulated temporal profile evolutions of the 337 nm ASE-type lasing pulse along the 3-cm-long filament plasma in the forward direction. The z term denotes position on filament plasma along the propagation direction of IR pump laser. For better comparison, some curves are enlarged by different factors, which are denoted beside the curves.

ASE pulse has a duration (FWHM) of ∼18 ps, which agrees well with our experimental observations (see Fig. 2.18). This pulse duration is much shorter than the shortest pulse duration (∼ 50 ps) obtained from a discharge pumped nitrogen laser under very high pressure of 6 atm [49]. We can expect even shorter duration of 337 nm ASE lasing pulse at higher nitrogen pressure because of higher optical gain (see Fig. 3.11), which naturally leads to stronger amplification and saturation effect.

Evolution of backward 337 nm ASE is presented in Fig. 4.7. Backward 337 nm ASE is about 100 times weaker than the forward one, which agrees with the experiment observations. For the forward lasing emission, the spontaneous emission photons propagate

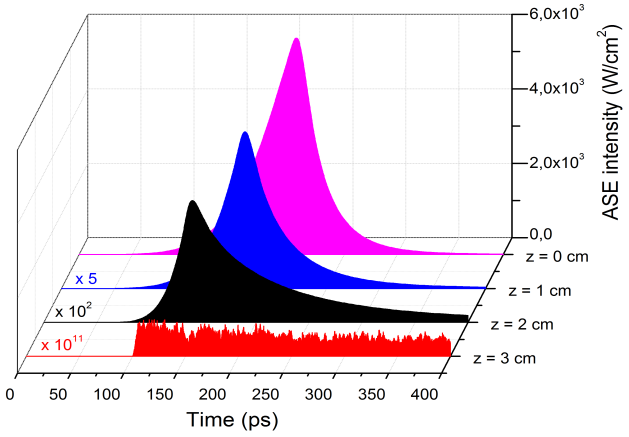

Figure 4.7: Simulated temporal profile evolutions of backward 337 nm ASE-type lasing pulse along the 3-cm-long filament plasma. The z term denotes position on filament plasma along the propagation direction of IR pump laser.

in the same direction as the IR pump beam, and interacts continuously with a newly created population inversion. On the contrary, in the case of backward 337 nm ASE, where the ASE counter-propagates with respect to the IR pump beam, the population inversion experienced by the spontaneous emission photon is depleted gradually by the forward ASE that follows the IR pump pulse. In fact, due to the short lifetime of the gain $\tau_g = 13\,ps$, the effective amplification length for a spontaneous photon propagating in the backward direction is $l = c\tau_g = 4.2\ mm$, which is much less than the 3 cm geometrical length of the plasma filament. After propagating through the 3-cm-long filament plasma, the pulse duration (FWHM) of the backward ASE is found to be 65 ps, in reasonable agreement with the autocorrelation measurement of 85 ps (see Fig. 4.7).

4.2.3 Simulation on temporal dynamics of externally-seeded 337 nm lasing

Considering the injection of an external seed pulse, we also simulated the temporal profile for both forward and backward emission. The result for forward lasing emission is shown in Fig. 4.8. The externally-injected seed pulse has a short duration (FWHM $\sim$ 100 fs) and broad bandwidth ($\sim$ 10 nm). It immediately polarizes the population-inverted medium coherently, which naturally leads to the generation and subsequent amplification of a retarded wake pulse. The evolution of the temporal structure of the seed pulse is mainly driven by its initial spectral profile and dominated by collisions (i.e. a Lorenzian line). The mismatch between the bandwidth of the seed pulse and that of $C^3\Pi_u^+ \rightarrow B^3\Pi_g^+$ transition leads to no seed amplification observed. The seed pulse only creates macroscopic polarization in the gain medium, and therefore the triggered

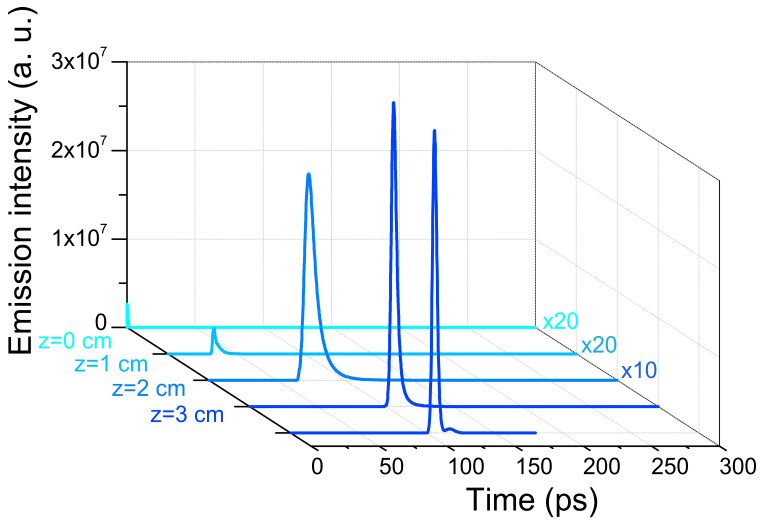

Figure 4.8: Simulation result of temporal profiles of forward seeded 337 nm lasing pulse at different positions (z) of the filament plasma amplifier with $n_e = 1.2 \times 10^{16}\ cm^{-3}$ and $T_e = 16\ eV$. Note that the intensity is magnified by factors denoted on the right for the sake of visualization.

wake pulse evolves independently, consistent with the experiment observation (see Fig. 3.5). The retarded wake appears from the beginning of the filament plasma amplifier, and its duration increases until it matches the temporal scale of the macroscopic polarization. For longer distance, the wake experiences amplification. When the wake is intense enough, the saturation effects reduce its duration until it attains the value of 4.5 ps (FWHM) after propagating through a 3-cm-long filament plasma, in good agreement with the experiment result (see Fig. 3.7).

Due to the employment of the slowly-varying envelope approximation, we are treating the field envelope, not the laser field. As a result, beating effect cannot directly appear in our Maxwell-Bloch simulations. Thus, we post-processed our electric field data assuming an interference effect between sub-levels to examine if the experimental oscillations were caused by the beating. To do this, the total electric field as given by our code is divided into three branches and a coherent sum of the three fields is done. When the arbitrary phases between the three fields are correct, the position of experimental maxima and minima are retrieved. The simulation results agreed well with experimental ones, as shown in Fig. 3.8.

We also simulated numerically the temporal profile evolution of backward seeded 337 nm lasing pulse, as shown in Fig. 4.9. Note that the seed and the IR pump pulses enter the plasma from opposite sides, at t = 0 ps. Thus, the seed propagates without influence until it meets the IR pump in the middle of filament (t = 50 ps). From this point on, the seed starts to polarize the gain medium and generate a wake. At the exit of the filament amplifier, the simulation predicts a moderately amplified seed pulse,

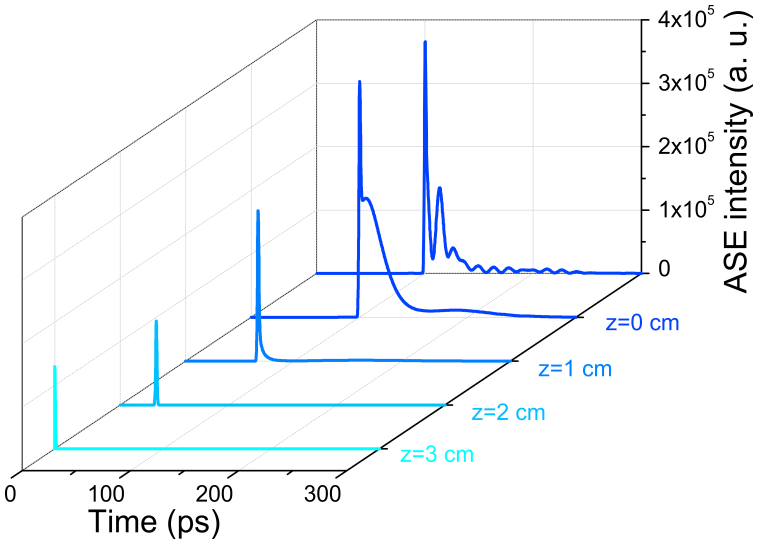

Figure 4.9: Simulation result of temporal profiles of backward seeded 337 nm lasing pulse at different positions (z) of the filament plasma amplifier with $n_e = 1.2 \times 10^{16}\ cm^{-3}$ and $T_e = 16\ eV$.

followed by a wake radiation extending over more than 60 ps, in good agreement with our experiment observations (see Fig. 3.18). We would like to point out that this kind of wake emission has been widely observed in the simulation of X-ray amplification in gas plasma [32].

4.3 Summary

In summary, the underlying mechanism of population inversion has been attributed to the inelastic electron-molecule collision excitation process. This well explains the crucial dependence of this lasing action on pump laser ellipticity through simulating the kinetic energy distribution of electrons upon ellipticity, as well as the pressure dependence of gain dynamics of 337 nm lasing.

We applied a theoretical model to our case to understand the significant differences in 337 nm ASE pulse duration and intensity in forward versus backward directions. This model based on one-dimensional non-adiabatic Maxwell-Bloch equation, which takes into account the pump-seed geometry, the initial free electron energy distribution, well reproduces the observed dynamics. The numerical simulations agree well with the experimental results and reveal that this difference originates from the traveling excitation scheme of pump laser and the limited lifetime of optical gain.

Part III

Superradiance From Singly Ionized Nitrogen Molecule in Femtosecond Filaments

Chapter 5

Lasing of Nitrogen Ions in Air Filament: Experimental Results

Contents

5.1 Introduction

In previous chapters, the bidirectional 337 nm lasing emission from excited neutral nitrogen molecules in filamentary plasma in pure nitrogen gas or ambient air have been studied experimentally and numerically. In this chapter, we are going to present another kind of lasing emissions from filamentary plasma in air and nitrogen, due to ionic molecule N_2^+. It occurs at 391 nm, 428 nm, 471 nm wavelengths and etc. These wavelengths corresponds to the $B^2\Sigma_u^+ \rightarrow X^2\Sigma_g^+$ transition between the excited and ground cation states, as shown in Fig. 5.1.

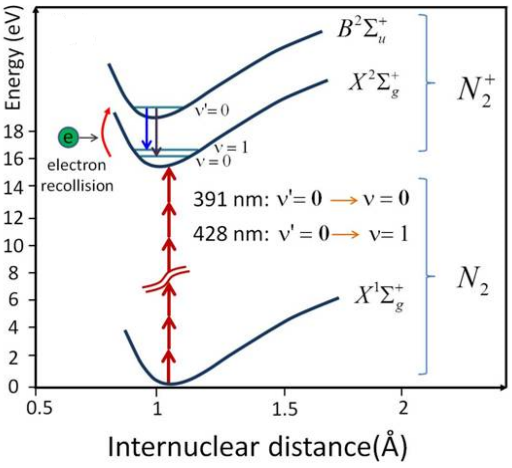

Figure 5.1: Schematic diagram of relevant energy levels of nitrogen ions. The symbols ν and ν' denotes the quantum numbers of vibrational levels.

This lasing effect was discovered in 2011 by researchers from Shanghai Institute of Optics and fine Mechanics (SIOM). In this work, Yao and co-authors reported a strong forward emission from air plasma pumped by tunable mid-IR femtosecond laser pulses ($\lambda = 1.2\ \mu m - 1.9\ \mu m$) [20], see Fig. 5.2. These emission manifests as narrow spectral lines (∼1 nm) located at 330 nm, 357 nm, 391 nm, 428 nm and 471 nm wavelengths, superposed on relative broad 3rd or 5th harmonics. It was found that when the 3rd or 5th harmonic of the driving pulse overlapped with these aforementioned spectral positions, strong emission can be initiated. The authors attributed this phenomena to the amplification of the weak harmonic pulse in the presence of population inversion that occurs at an ultrafast time scale (less than $\sim$ 200 fs). The mechanism of population inversion was attributed to direct formation of excited molecular nitrogen ions by strong-field ionization of inner-valence electrons.

Later on, G. Andriukaitis *et al* obtained forward 391 nm and 428 nm lasing emission by focusing a sequence of millijoule 1030 nm (near-IR) femtosecond laser pulses to generate a filament in a cell filled with nitrogen [21]. Tentatively, the lasing emission was

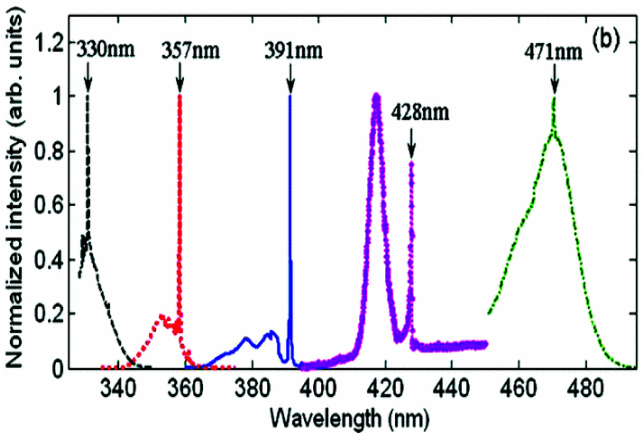

Figure 5.2: Measured lasing peaks at 330, 357, 391, 428 and 471 nm achieved with different pump wavelengths of 1682, 1760, 1920, 2050 and 1415 nm respectively. Taken from the ref. [20].

ascribed to four-wave mixing between intense near-IR pulses and weak supercontinuum components, resonant to the UV transitions.

In above two works, mid-IR ($\lambda = 1.2\ \mu m - 1.9\ \mu m$ or $1.03\ \mu m$) pump laser pulses were employed. In 2013, the observation of 391 nm and 428 nm lasing emissions from N_2^+ by using commercial 800 nm laser as pump was reported, with assistance of external injection of a seed pulse at correspondent wavelength [22, 23]. The durations of these two coherent emissions was measured to be few picoseconds. They also measured the lasing intensity as a function of relative time delay between the pump pulse and the seed pulse, which suggests instantaneous optical gain achieved in molecular nitrogen ion.

Soon, our group made another progress. By just using 800 nm laser pulse, we achieved lasing emission of N_2^+ from filamentary plasma in air and nitrogen, without injecting external seed pulse [24]. We attributed it to self-seeding effect. Specifically, the 391 nm lasing emission observed at low pressure is seeded by the 2nd harmonic around 400 nm generated by the 800 nm pump laser in filamentary plasma. The 428 nm lasing emission observed at higher gas pressure is seeded by the wing of supercontinuum that generated when the pump pulse undergoes filamentation (recalling Chapter 1). At almost same time, another two independent works also reported on self-seeded lasing emission of N_2^+ [25, 26]. Later on, by pumping ambient air with 1.5 TW 800 nm femtosecond laser pulses delivered by the ENSTAmobile laser system, we observed forward 428 nm lasing emission with pulse energy of $2.6\mu J$, corresponding to a conversion efficiency of 3.5×10^{-5} [27]. The optical gain inside the filament plasma was estimated to be in excess of $0.7/cm$.

In my thesis, I mainly focused on the lasing effect of N_2^+ pumped by 800 nm femtosecond laser pulses. In this chapter, we will experimentally study the lasing emission of

excited ionic N_2^+ molecules at 391 nm and 428 nm wavelengths from filamentary plasma in air and nitrogen that has been created by 800 nm femtosecond laser pulses. As we have seen above, this lasing action can be classified into two regimes: self-seeded and externally-seeded cases. In these two regimes, we characterized this ionic lasing through the spectrum, the spatial profiles, the temporal waveforms, the pump ellipticity dependence, the pump pulse energy dependence, the enhancement with the external seeding pulse. In addition, the gain dynamics of 391 nm lasing emission will be in details studied because its importance to understand the underlying mechanism of this lasing effect.

The outline of this section will be as follows: In section 5.2, we briefly introduce the experimental setups for both self-seeding and externally-seeding regimes, and the cross-correlation setup for measuring the temporal waveforms of lasing emission pulse. In following sections, we present the measured results including spectrum, spatial profile, temporal profile, lasing emission polarization, spatial profiles and so on, to fully characterize the lasing emission. In section 5.5, the gain dynamics of 391 nm lasing will be presented. At last in section 5.6, we summarized the experimental observations.

5.2 Description of experiment setup

In this experiment, we employed the same aforementioned laser system (see section 2.2.1, Chapter 2), which provides 45 fs laser pulses at 800 nm wavelength, with pulse energy up to 15 mJ. The experimental setup is shown in Fig. 5.3. The pump laser

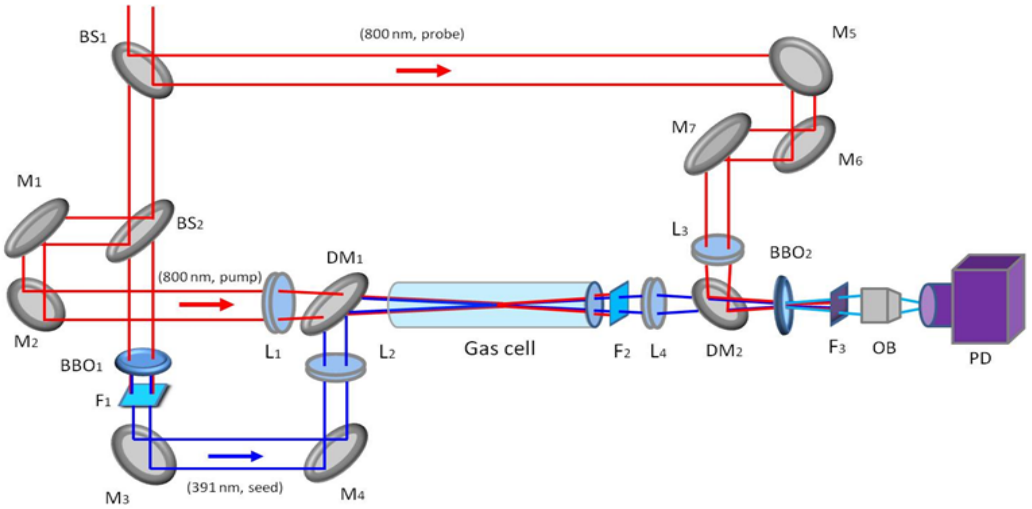

Figure 5.3: Schematic illustration of experimental setup for measuring 391 nm and 428 nm lasing emissions. BS denotes beamsplitter, M the high reflective morror, L the focusing lens, DM the dichromatic mirror, F the interference filter, OB the collecting lens and PD the photodiode detector.

pulses were focused by a convex focal lens ($L_1 = 40\ cm$) into a gas chamber whose

pressure can be well controlled. Bright filamentary plasma strings were created in the gas chamber, with length of few centimeters depending on the focal length, incident pump pulse energy and gas pressure. The emission emerging from the gas chamber were first filtered by two colors filters (BG 40, denoted bu F_2), which transmit the spectral components shorter than 600 nm but block significantly the fundamental pulses and the accompanying supercontinuum. The filtered pulses were then focused by a fused silica lens (f = 10 cm) to couple them into a fiber spectrometer. A photodiode was also used to measure the emission intensity.

In order to provide an external seeding pulse into the plasma, we can split the laser beam by BS_2 and the frequency of transmitted fundamental beam was doubled by a BBO crystal. The residual fundamental beam was then blocked by another BG 40 filter (F_1). The seed pulse at around 400 nm wavelength was then focused into the gas chamber by a convex focal lens ($L_2 = 50\ cm$), which can be precisely controlled three-dimensionally in order to adjust the spatial overlap between the focused seed beam and filament plasma created by the pump pulse.

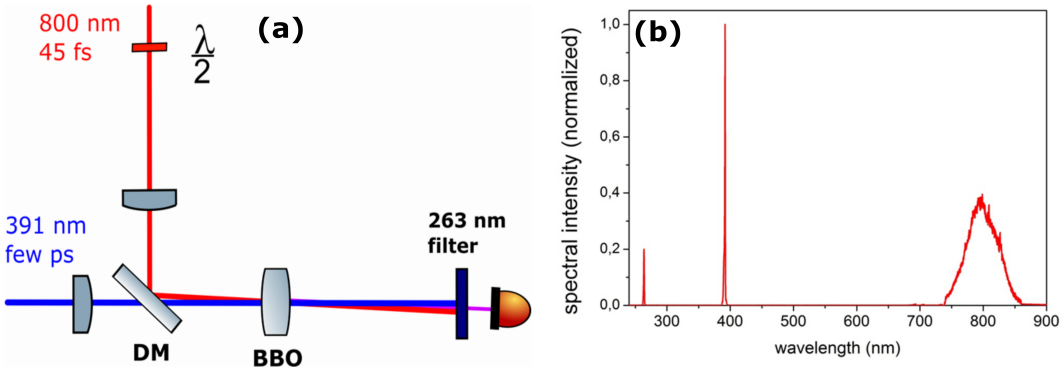

Figure 5.4: (a) Schematic illustration of the cross-correlation method. $\lambda/2$ denotes half wave plate, used to change the polarization of 800 nm probe pulse. (b) Spectra of the fundamental 800 nm pump laser, the 391 nm lasing emission and their sum-frequency signal at 263 nm wavelength.

To measure the temporal waveforms of lasing emission, the laser beam at the beginning can be sampled by a 10% beamsplitter to act as the "probe" beam . After a time delay consisted by M_5 and M_6 positioned on a software-controlled translation stage, the "probe" beam was focused by a convex lens (L_3) and then reflected by a dichromatic mirror (DM_2) into a BBO crystal. The lasing beam from filament plasma was first focused by a fused silica convex lens (L_4) into the aforementioned BBO crystal to spatiotemporally overlap with the "probe" beam, forming up a cross-correlation setup based on sum-frequency generation. In Fig. 5.4(a), we show here a simplified illustration of cross-correlation setup. The sum-frequency generation of 800 nm fundamental pulse (45 fs duration) and 391 nm lasing pulse is at 263 nm wavelength, which is selected by the interference filters (F_3) and then detected by spectrometer or photodiode, as shown

in Fig. 5.4(b). For 428 nm lasing emission, the sum-frequency signal is at 280 nm. By recording the intensity of sum-frequency signal as a function of relative delay between the fundamental 800 nm pulse and lasing pulse, we can obtain the temporal profile of lasing pulse.

5.3 Characterization of ionic lasing emission in self-seeded regime

5.3.1 Spectra of 391 nm and 428 nm lasing emissions

In the experiment, the incident pump energy was 1.8 mJ, and a ~1-cm-long filament plasma string was created in nitrogen gas. In Fig. 5.5, we first present the measured spectra of forward lasing emission of N_2^+ molecules in nitrogen gas for different pressures ranging from low pressure ~2 mbar to high pressure of 1 bar. The general feature is the successive appearance of lasing emissions with the increasing nitrogen pressure in the sense that 391 nm lasing emission appears within the pressure range from 10 mbar to 70 mbar, and 428 nm lasing emission appears from the pressure of 46 mbar to the limit of 1 bar. The pressure range depends on the focal geometry, and the incident pump pulse energy. Given the same pump pulse energy, the pressure range becomes smaller if a longer focal length is used [24].

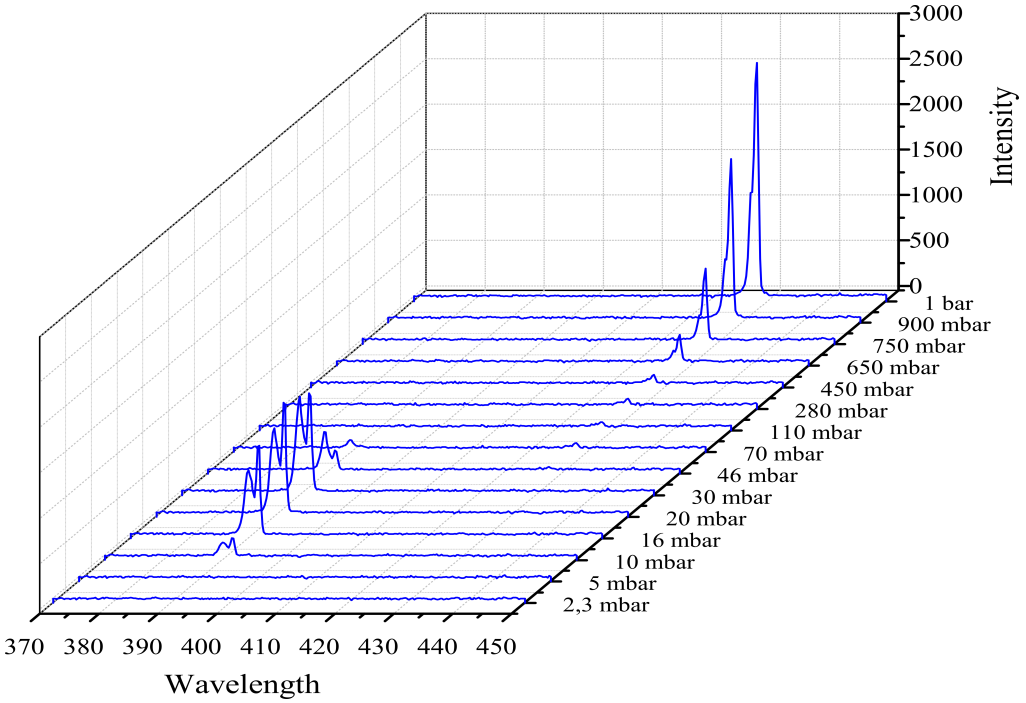

Figure 5.5: Spectrum of the forward lasing emission in nitrogen at different gas pressures. The incident pump pulse energy is 1.8 mJ.

The spectrum of 391 nm lasing emission is actually composed of two separated lines at 390.0 nm and 391.6 nm (see Fig. 5.6), which belongs to the R-branch and P-branch of the $B^2\Sigma_u^+(\nu = 0) \rightarrow X^2\Sigma_g^+(\nu' = 0)$ transition respectively, where different levels of quantum rotation of N_2^+ molecule are involved. The R-branch of the spectrum corresponds to the rotational quantum number $\Delta J = +1$ and the P-branch $\Delta J = -1$. To resolve the discrete spectral lines corresponding to different rotation states of the

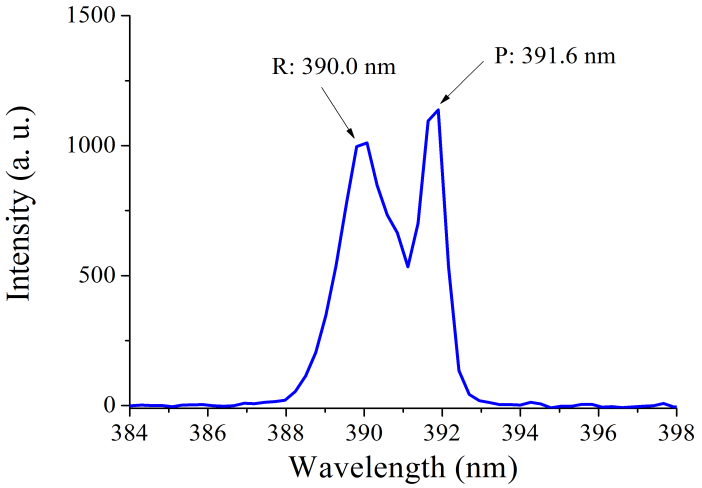

Figure 5.6: Typical spectrum of the 391 nm lasing emission of N_2^+ molecules.

transition, as done in Ref. [50], a higher spectral resolution is required. The relative strength of the two branches changes with the gas pressure. At low pressure, the P-branch is stronger than the R-branch, while at higher presure $P_{N_2} > 30$ mbar the R-branch surpass the P-branch. It is necessary to mention that the relative strength of two branches also depends on the incident pump energy and P-branch dominates at high pump energy.

For the spectrum of 428 nm lasing emission, it also exhibits R-branch and P-branch. We can see that in Fig. 5.5 the P-branch dominates. In addition, with proper experiment condition, a weak emission peaked around 471 nm wavelength, corresponding to the $B^2\Sigma_u^+(\nu = 0) \rightarrow X^2\Sigma_g^+(\nu' = 2)$ transition can be observed [24]. It is necessary to mention here that 391 nm lasing emission and 428 nm lasing emission mostly have the same features except of their different transitions. Therefore, as follows we focus on studying the 391 nm lasing emission and present results of 428 nm lasing emission as it is necessary.

5.3.2 Spatial profile and beam divergence

Fig. 5.7 shows the far-field spatial profiles recorded ~50 cm away in the forward direction by an iCCD camera (Princeton Instrument PI-MAX), before which two BG 40 filters were used to select the lasing emission. In this experiment, the focal length of 75 cm was used. The upper panel shows the spatial profiles of 391 nm lasing beams at different nitrogen pressures of 2 mbar, 15 mbar and 30 mbar respectively. The 391 nm lasing beams show a TEM_{10} mode with a central maximum surrounded by a donut-shaped profile. As mentioned before, the 2nd harmonic at around 400 nm is generated in our experiment, which serves as a seeding emission to initiate strong 391 nm lasing emission [24]. At the same time, the supercontinuum generation in filamentation can extend to the UV range, in which higher frequency components have less energy. For example, the intensity of 428 nm supercontinuum component is stronger than 391 nm component. The supercontinuum is emitted in a conical form during laser pulse filamentation. We here

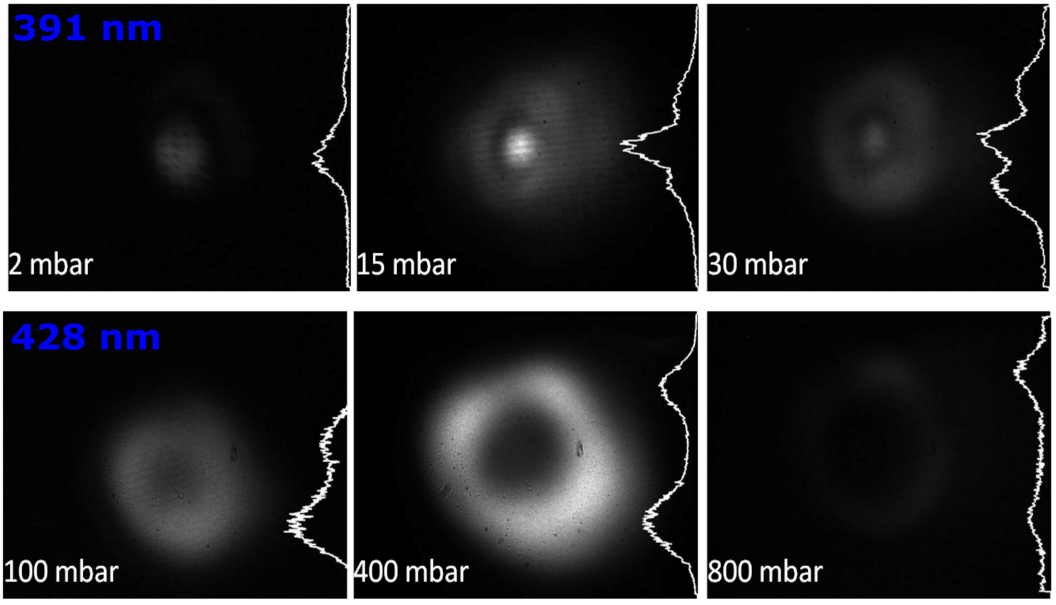

Figure 5.7: Spatial profiles of the 391 nm (upper panel) and 428 nm (lower panel) lasing beams at different nitrogen pressures. In each panel, the pressure is denoted. The angle of view of each panel is 60 × 40 mrad. The white lines on the right of each panel present the vertical line-cut of each intensity distribution on the center.

interpret the self-seeded 391 nm lasing emission is initiated by both the relatively stronger 2nd harmonic along the longitudinal direction and the weaker 391 nm supercontinuum component in the off-axis direction, which respectively result in the central maximum and doughnut-shaped ring of the spatial profile of 391 nm lasing beam, as shown in Fig. 5.7. In contrast, the 428 nm lasing beam only has a pure doughnut TEM_{10} mode, as shown in lower panel for different nitrogen pressures of 100 mbar, 400 mbar and 800 mbar. It is initiated by the 428 nm supercontinuum component in filament.

The lasing beam is well directional, and the divergence of 428 nm lasing beam at 400 mbar was measured to be ~20 mrad. The Fresnel number of filament, considered as pencil-shpaed cylindrical plasma, can be calculated as $F = \pi w^2/L\lambda = 0.61 < 1$, where $w = 50\ \mu m$ is the transverse radius (we assume the width of filament as typical value of 100 μm), $L = 30\ mm$ is longitudinal length of the filament and $\lambda = 428\ nm$ is the lasing wavelength, respectively. If $F < 1$, the lasing emission essentially occurs in a single mode but presents a strong diffraction pattern. The diffraction angle can be estimated as $\theta_D = \lambda/w = 8.56\ mrad$, and the geometrical angle as $\theta_G = w/L = 1.67\ mrad$. So the diffraction angle is about 5 times larger than the geometrical angle. With such small Fresnel number, a single mode emission can be expected and the filament plasma can be considered as one dimensional emitter [51].

5.3.3 Temporal profile

In the experiments, the pump laser with pulse energy of 10 mJ was focused by a $f = 50\ cm$ convex lens into gas chamber to generate a 3-cm-long filament plasma. The optimal nitrogen pressure for forward 391 nm lasing emission was found to be ~20 mbar. Figure 5.8 shows the measured temporal waveforms of forward 391 nm lasing pulses at

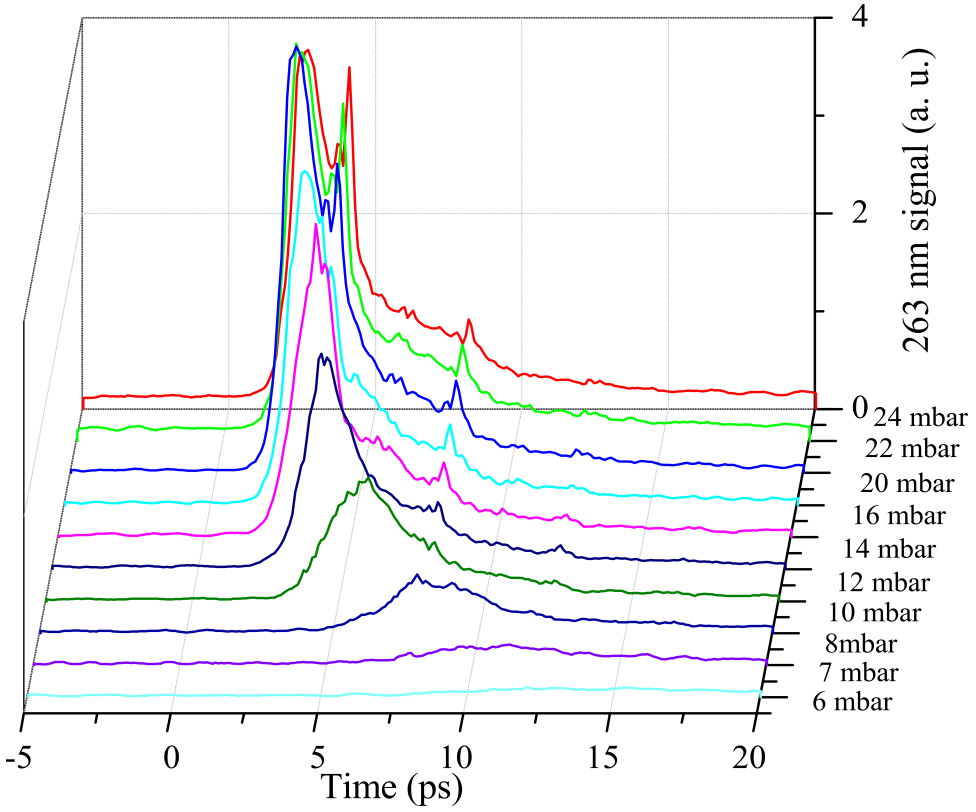

Figure 5.8: Measured temporal profiles of forward self-seeded 391 nm lasing emission in pure nitrogen at different pressures ranging from 6 mbar to 24 mbar.

different nitrogen pressures. The zero time represents the time when pump laser pulse arrives. The general features are that both the pulse width of 391 nm lasing pulse and its delay with respect to the pump pulse become shorter and their peak intensity becomes stronger with the increase of nitrogen pressure in the range from 6 mbar to the optimal pressure of 20 mbar. These are features of the so-called superradiance, which will be discussed in details in Chapter 6. When the nitrogen pressure is increased to be higher than the optimal one, for instance from 20 mbar to 24 mbar, these aforementioned trend develops inversely. It is consistent with the measured pressure dependence of 391 nm lasing intensity shown in Fig. 5.10.

Typically, the temporal profile of 391 nm lasing pulse obtained at the optimal pressure gives a width of ∼1.7 ps and delay of ∼2.7 ps. In addition, we can see two peaks on the temporal profile curves at 4.1 ps and 8.2 ps due to the molecular alignment effect, respectively corresponding to the half-cycle and full-cycle revival of alignment of N_2 molecule in the laser field.

5.3.4 Pump energy threshold

We measured the intensity of forward 391 nm lasing emission and transverse fluorescence as a function of incident pump pulse energy. The result is presented in Fig. 5.9. The focal length is 40 cm and we choose the nitrogen gas pressure as 30 mbar for lasing emission. A pump threshold around 1 mJ is observed for 391 nm lasing emission. The lasing intensity monotonously increases with the pump pulse energy E and somewhat saturates as $E \sim 4$ mJ. We fitted both lasing and fluorescence signal by using a form of $I = aE^b$ where a, b are two coefficients. The forward lasing signal scales as the 2.25 ± 0.10 power of the pump pulse energy and has a threshold, whereas the transverse fluorescence signal scales as the 0.93 ± 0.05 power of the pump pulse energy and has no threshold. This distinct difference indicates that the forward strong 391 nm emission is not at all a normal fluorescence phenomenon and it can have different physical origin.

5.3.5 Nitrogen pressure dependence

The intensity of forward 391 nm lasing emission as a function of the nitrogen pressure is presented in Fig. 5.10. In this experiment, the pump pulse energy is about 1.7 mJ and the focal length of convex lens we used is 50 cm. The lasing emission appears at few mbar pressure, and increases quickly with increasing nitrogen pressure, and finally reaches maximal intensity at around 15 mbar. Beyond that, the lasing emission starts to decrease slowly with increasing pressure until undetectable at about 60 mbar. The optimal gas pressure for lasing generation depends on many factors such as the laser

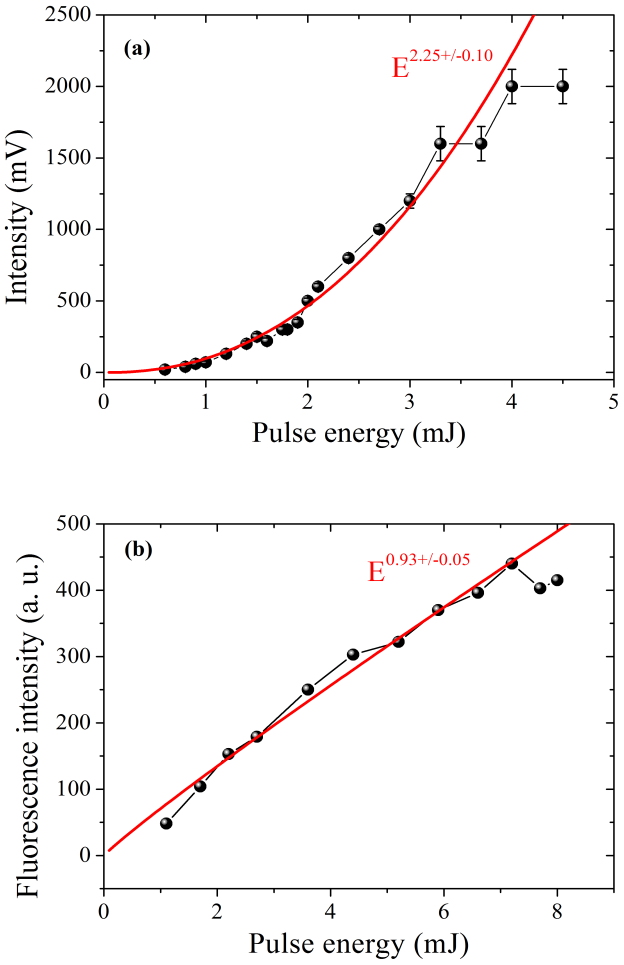

Figure 5.9: (a) The incident pump pulse energy dependence of 391 nm lasing emission of N_2^+ molecules, under experiment conditions: 30 mbar pure nitrogen, the focal length of $f = 40\ cm$ and a photodiode as detector. (b) The incident pump pulse energy dependence of transverse 391 nm fluorescence intensity. The red curves represnts fit with the form $I = aE^b$ with the coefficients denoted beside.

intensity inside filament, the plasma density, the longitudinal length and transverse width of filament plasma. Given the conditions of keeping the pump pulse energy and the focusing geometry, the aforementioned factors nonlinearly depend on the gas pressure, and their synactic process results an optimal gas pressure. For example in the external focusing case, the width of filament increases slightly with pump pulse energy rather than keeping a constant of $\sim 100\ \mu m$ in the self-focusing regime. The laser intensity inside filament first increase almost linearly with the pump pulse energy and then experience clamping [52]. When we change the pump pulse energy or the focusing geometry, the optimal pressure and the pressure range for 391 nm lasing emission will change too. When the pump pulse energy is increased, we observed that the optimal pressure shifts to higher value and the pressure range becomes broader. The increasing pump pulse energy results in higher laser intensity inside filament plasma and elongates the longitudinal length of

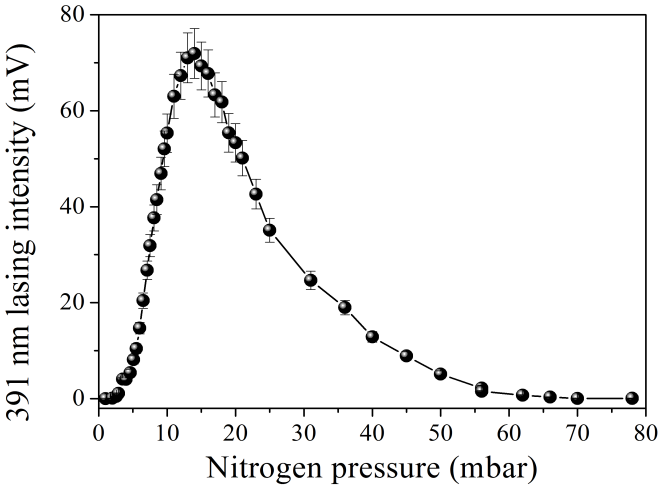

Figure 5.10: Intensity of 391 nm lasing emission as a function of nitrogen pressure, measured by a photodiode. In the measurement, the focal length was 50 cm, and the pump pulse energy was about 1.7 mJ after the dichromatic mirror.

filament. Therefore, a higher density of N_2^+ molecules can be excited, corresponding to an higher optimal nitrogen pressure. When we fix the pump pulse energy and use longer focusing length, the filament will become longer but at the same time the laser intensity becomes lower, which leads to a lower optimal pressure and narrower pressure range (refer to Ref. [24]). In the following context, we usually generate the forward 391 nm lasing emission at the optimal pressure.

5.3.6 Dependence on pump laser ellipticity

The above experimental results were obtained with linearly polarized pump pulses. Here, we studied the emission intensity as a function of the the ellipticity of the pump laser pulses for 391 nm and 428 nm wavelengths in both transverse and forward direction. The transverse emission has been determined as fluorescence and the forward one as lasing emission. The results is presented in Fig. 5.11. The pump laser ellipticity is controlled by rotating a quarter-wave plate. The zero degree corresponds to the ellipticity $\epsilon = E_y/E_x = 0$, e.g., the linear polarization, and 45° corresponds to the ellipticity $\epsilon = 1$, e.g., the circular polarization. For both 391 nm and 428 nm, the transverse fluorescence intensity achieves their maximum with the ellipticity of zero and gradually decreases with the increasing ellipticity.

In contrast, the forward lasing shows different dependence. First, we noticed that the forward lasing emission is more sensitive to the pump laser ellipticity than the transverse fluorescence, in the sense that the fluorescence signal gentle depends on the pump laser ellipticity while the lasing signal decreases from the maximum to undetectable in the

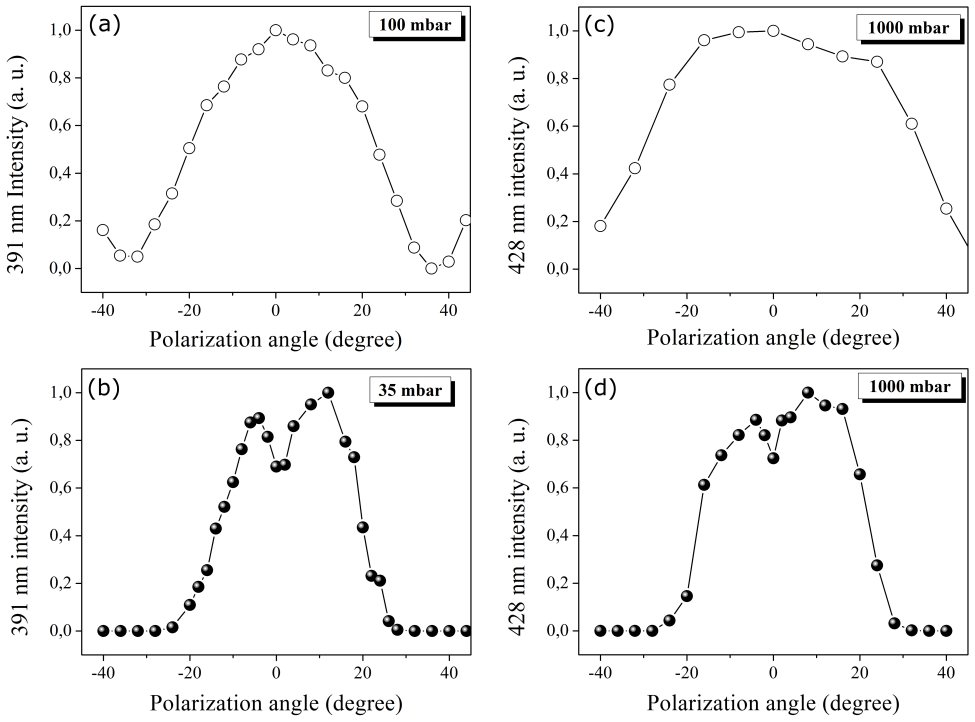

Figure 5.11: The 391 nm and 428 nm transverse fluorescence and forward lasing emission at a function of the ellipticity of the pump laser pulses at 800 nm. The polarization angle of 0° (45°) corresponds to ellipticity of 0 (1), e.g., linear (circular) polarization. (a) The 391 nm transverse fluorescence was measured by using 2.5 mJ pump pulse energy under 100 mbar nitrogen pressure; (b) The forward 391 nm lasing emission was measured by using 2.7 mJ pump pulse energy under 35 mbar nitrogen pressure; (c) The transverse 428 nm fluorescence was measured by 3.5 mJ pump pulse energy under 1 bar air; (d) The forward 428 nm lasing emission was measured by using 2.7 mJ pump pulse energy under 1 bar nitrogen. In all these measurements, the focusing length was 40 cm.

ellipticity change of $\Delta\epsilon \sim 0.4$. Surprisingly, the curve of lasing emission intensity as a function of pump laser ellipticity shows a "dip" in the center and the maximum of forward lasing emission intensity is obtained when $\epsilon \sim 0.2$. This dip is more obvious for 391 nm lasing emission than 428 nm lasing emission.

There is a striking analogy between the ionic lasing emission and high-order harmonics generation (HHG) in the aspect of pump laser ellipticity dependence. To compare their dependences on the pump pulse ellipticity, we performed measurements under identical experimental conditions in a gas cell installed in vacuum background. In our experiments, the gas pressure can be precisely changed from few mbar to hundreds of mbar, and the ambient pressure is controlled to be about 10^{-5} bar. The laser system provides laser pulse with central wavelength of 810 nm, duration of 42 fs, and repetition rate of 1 kHz. The diameter of laser beam is about 26 mm. We used 1-m convex lens to focus the laser beam into the gas cell. The lasing emission is collected by a 40 mm fused

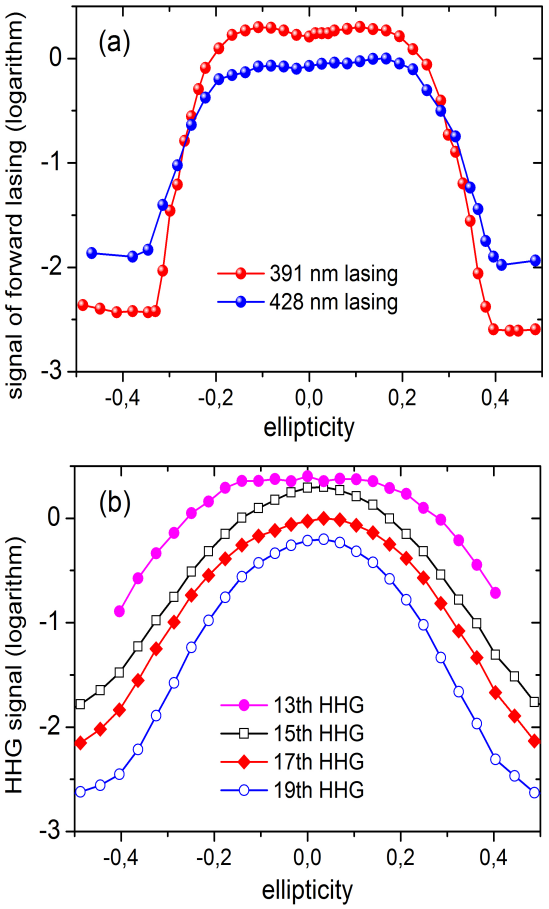

Figure 5.12: (a) 391 and 428 nm lasing emission as a function of the ellipticity of the pump pulses at 800 nm. The gas pressures were 45 and 300 mbar, respectively. (b) Dependence of the high-order harmonic yield in nitrogen gas as a function of the laser ellipticity. The experiments were performed in a 15-mm-long gas cell with two 150 μm holes on the entrance and exit surfaces of the gas cell, which were drilled by the laser pulse itself on the 100 μm thick aluminum foil windows. Each data point was an average over 10 000 laser shots. The nitrogen gas pressure was about 65 mbar and the pump pulse energy was 3.8 mJ.

silica lens into photodiode or spectrometer while the generated $13^{th} \sim 19^{th}$ high-order harmonics was detected by a XUV CCD camera after a diffraction grating.

Fig. 5.12 shows the results. The lasing emission and high-order harmonics show highly similar dependence on the pump pulse ellipticity. The effect of pump laser ellipticity on HHG is well understood based on a semi-classical model proposed by P. B. Corkum in 1993 [53], which successfully predicts the main features of HHG. The HHG process is divided into three successive steps: the tunnel ionization, the motion of the free electron wave packet in the strong laser field, and the recombination with the parent ion. With a circularly polarized light pulse, the returning free electron wave function hardly overlaps with the parent ion and therefore can't transform its kinetic energy in the form of high harmonics.

The "dip" feature of ionic lasing emission is really puzzling. A similar "dip" feature has also been reported for high-order harmonics with photon energies close to the ionization potential in oxygen, hydrogen and noble gases [54–58]. It has been attributed to different mechanisms, such as the interference effect of successive recollisions, free-free or bound-bound transition contributions to the nonlinear atomic susceptibility, and the near-resonant multi-wave-mixing process. To have a convincing interpretation of the "dip" feature of lasing emission, more experimental and theoretical work are needed.

5.4 Externally-seeded ionic lasing emission

As we mentioned in the introduction, strong 391 nm and 428 nm lasing emission from air plasma pumped by 800 nm femtosecond pulse was first observed with the external injection of seeding pulse at proper wavelength. The advantage of this scheme lies in that we can well control the properties of the seeding pulse (energy, polarization, wavelength etc), which is impossible in the self-seeded case. Here, we characterize the lasing emissions in the external-seeded regime. The spectrum measurements of seeded 391 nm lasing emission in both forward and backward directions will be first presented in subsection 5.4.1. Then, the temporal profiles of lasing emission will be presented. The following subsection 5.4.3 and 5.4.4 respectively gives the pump energy threshold and seed intensity dependence of the seeded lasing intensity. In the end, an interesting results regarding the polarization direction of seeded 391 nm lasing will be shown in sub-subsection 5.4.5.

5.4.1 Amplification of the seeding pulse

The experimental setup has been shown in Fig. 5.3 and Fig. 3.13. Given spatial overlap between the focused seed beam and the filament plasma, we vary the relative delay between the seed pulse and the pump pulse by a translation delay line to obtain maximal lasing intensity. Fig. 5.13 shows the results of spectrum measurements of externally-seeded 391 nm lasing signal in both forward and backward directions. Note that the enhancement mainly occurs at P-branch. We can see that the forward 391 nm lasing emission is significantly enhanced in the presence of a weak seed pulse, about 10 times stronger that the self-seeded signal by only pump pulses. The amplified emission is ~300 times more intense than the injected weak seeding pulse. Based on this value, we can estimate the gain as

$$g = \frac{1}{l}(\frac{I_{out}}{I_{in}}) \simeq 5.7$$

where $l \simeq 10\ mm$ denotes the plasma length.

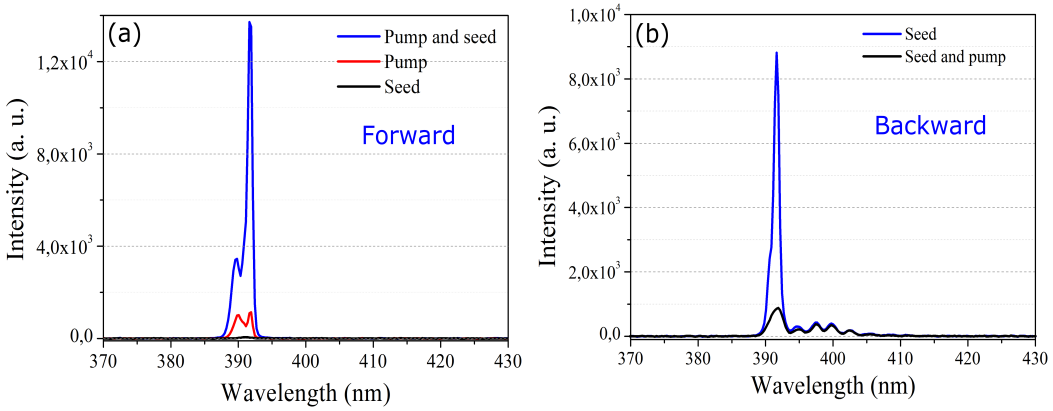

Figure 5.13: (a) The spectra of externally-seeded 391 nm lasing emission in forward direction. In the experiment, the pump pulses with energy of 1.8 mJ was focused by a 40 cm convex lens into 30 mbar nitrogen gas. The black line represents the seed signal, and the red line represents the lasing signal generated by only pump pulses and the blue the lasing signal represents the seeded lasing signal when the pump and seed pulses spatiotemporally overlapped. (b) The spectrum of seeded 391 nm lasing emission in backward direction. The used pump pulse energy was 7.5 mJ. No backward self-seeded 391 nm lasing signal was detected.

In the backward direction, we have not managed to detect the self-seeded 391 nm lasing emission, which is different from the lasing emission from neutral nitrogen molecules. However, in the presence of backward-propagating seed pulse, we observed $\sim$ 10 times amplification compared to the seed intensity by using higher pump pulse energy of 7.5 mJ.

5.4.2 Temporal profile of seeded 391 nm lasing emission

Similar to the measurement of the emission temporal profile in the self-seeded regime, we also characterized the externally-seeded lasing emission in the time domain. The experiment setup has been introduced in section 5.2. Figure 5.14 shows the results of temporal profiles of externally-seeded 391 nm lasing emission at different pressures. Note that the seed pulse keeps $\sim$ 300 fs duration and isn't amplified while passing through the gain medium. Instead, it triggers the generation of a wake pulse. This wake pulse has the similar evolution features with the self-seeded 391 nm lasing pulse when the nitrogen pressure changes, e.g., the pulse width and delay with respect to the seed pulse decrease and the peak intensity increases with the increase of nitrogen pressure ranging from 5 mbar to 20 mbar, the optimal pressure for 391 nm lasing.

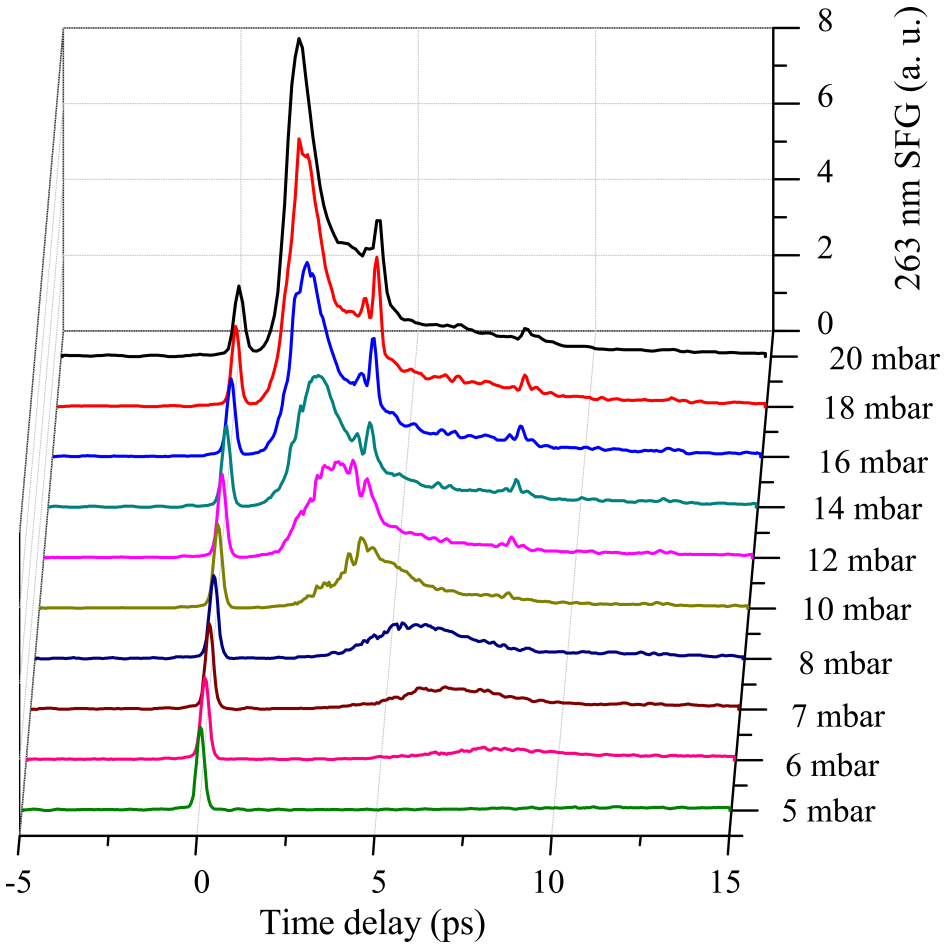

Figure 5.14: Measured temporal profiles of forward externally-seeded 391 nm lasing emission in pure nitrogen at different pressures ranging from 5 mbar to 20 mbar.

5.4.3 Pump energy threshold of backward seeded 391 nm lasing

The pump energy threshold of forward 391 nm lasing emission in nitrogen has been determined around 1 mJ under experiment conditions of 30 mbar nitrogen pressure and 40 cm focal length. In the backward direction, we didn't observe the self-seeded 391 nm lasing emission. Only the externally-seeded lasing signal was detected. Fig. 5.15 shows the pump pulse energy dependence of backward seeded 391 nm lasing intensity for two different seed intensities, respectively 50 mV and 110 mV measured by a photodiode. We can see that the pump energy thresholds in both cases can be estimated as $\sim$ 2.3 mJ, which is much higher than that of forward 391 nm lasing emission. Thus, the threshold doesn't rely on the seed intensity. We have repeated the measurement with spectrometer as detector, and it gives rise to identical pump energy threshold.

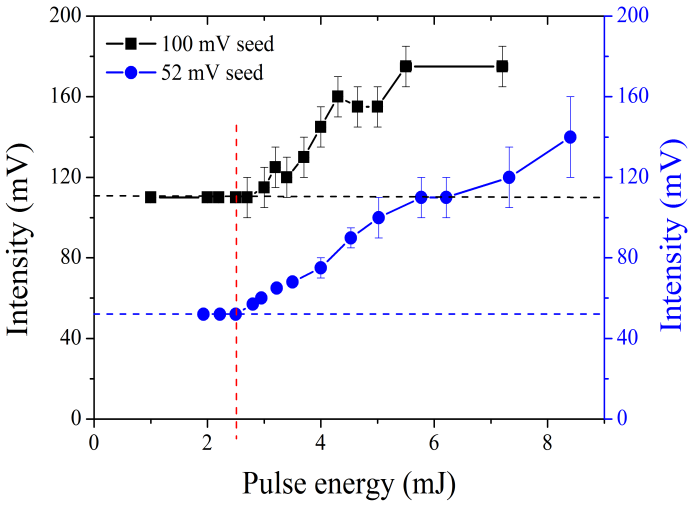

Figure 5.15: The externally-seeded 391 nm lasing intensity in backward direction as a function of pump pulse energy, for two seed intensities. The pump laser pulses were focused by a 40 cm convex lens into gas chamber filled with 30 mbar nitrogen, and the lasing emission was detected by a photodiode.

5.4.4 Seed intensity dependence

Fig. 5.16 shows the forward externally-seeded 391 nm lasing intensity as a function of the seed pulse intensity. In this measurement, the pump laser with pulse energy of 2.0 mJ was focused by a 50 cm convex lens into gas chamber filled with nitrogen under 16 mbar pressure. The 391 nm emission signal was detected by a calibrated photodiode. The externally-seeded 391 nm lasing signal increases linearly with the seed intensity in the range from 0.5 mV to 10 mV, and then starts to saturate when the seed intensity is in excess of 20 mV.

5.4.5 Polarization property of forward seeded 391 nm lasing emission

In the externally-seeded regime of 391 nm lasing, an unexpected phenomena was reported in 2016. The researcher of SIOM observed that the polarization of the seeded 391 nm lasing pulse can be different from that of the seed pulse [59]. In particularly, it has been reported in 2013 that the seeded 391 nm lasing pulse has same polarization with the linearly-polarized seed pulse when the polarization direction of the seed pulse is parallel or perpendicular to that of the pump pulse [22]. In our previous experiments, we have also confirmed this point. This was understood from a seed amplification point of view, in which the lasing signal generated by such process typically inherits the polarization property of the seed pulse. However, in recent publication in 2016, the authors observed that the seeded 391 nm lasing pulse show different polarization direction compare to

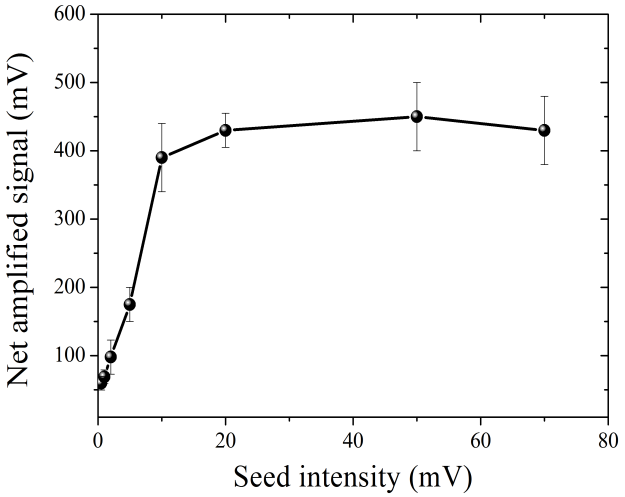

Figure 5.16: The seed intensity dependence of externally-seeded 391 nm lasing emission in forward direction. The net amplified signal is the result by subtracting the seed signal from the detected total 391 nm emission signal.

the seed pulse, when the polarization direction of the seed pulse is between parallel and perpendicular to the pump pulse.

We have tried to address this mysterious feature in our experiments. In the experiments, the polarization direction of the pump laser pulse keeps horizontal. A half wave-plate (HWP) for 391 nm wavelength was inserted after the BBO crystal to change the polarization direction of the seed pulse. A Glan-Taylor prism was placed before the detector to measure the polarization of the signal. Its rotation angle of 0° denotes the horizontal direction. Under optimal nitrogen pressure, the seeded 391 nm lasing emission was dominated by P-branch. Fig. 5.18 shows the measured signal intensities of the seeded lasing pulse and the seed pulse as a function of the rotating angle of the Glan-Taylor prism. In (a), we can see that both the seed pulse and seeded 391 nm lasing pulse have horizontal polarization direction and parallel to the pump pulse, being consistent with previous studies [22, 59]. When the polarization of the seed pulse was changed by rotating HWP to have an angle of 35° with respect to the pump pulse, as shown in (b), the seeded 391 nm lasing pulse does not inherit the polarization of the seed pulse and shows a smaller azimuthal angle of $\sim 10°$. We further changed the angle between the seed and pump pulses to 70° shown in (c), the seeded 391 nm lasing pulse shows an increased angle of 20°. However, the seeded 391 nm lasing pulse shows the same polarization direction with the seed pulse when we change the relative angle between the seed and pump pulses to 90°, e.g., the seed pulse is perpendicular to the pump pulse as shown in (d).

For clarity, the azimuthal angles ϕ of the polarization directions of the seeded 391

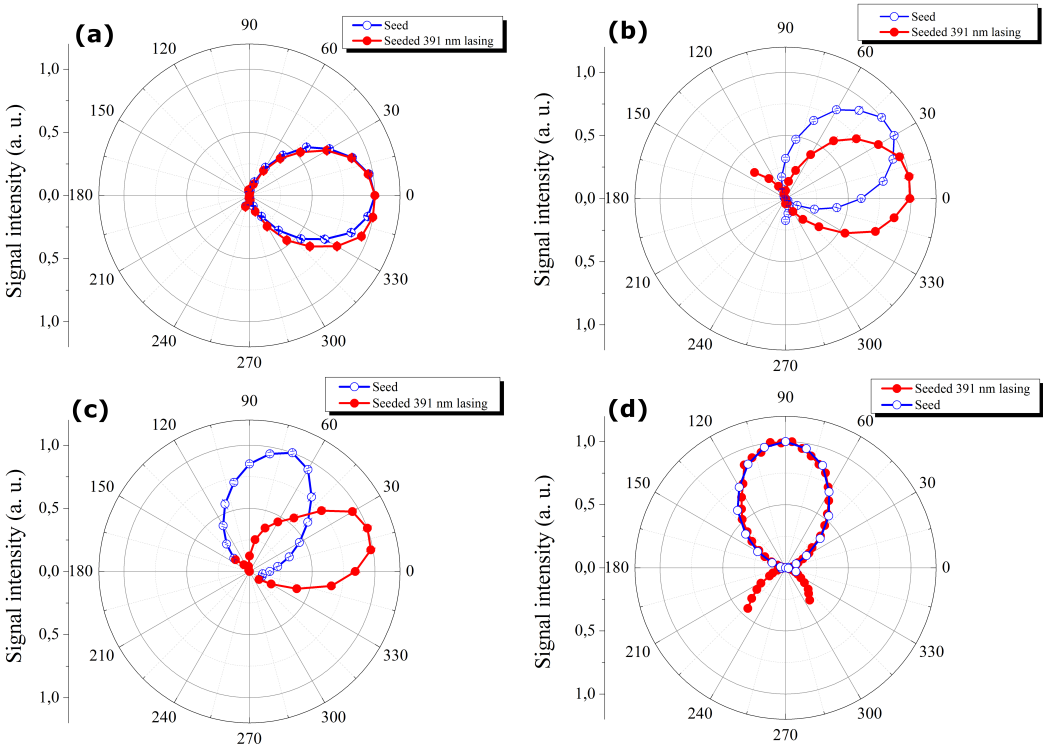

Figure 5.17: Measured intensities of forward seeded 391 nm lasing emission and the seed pulse as a function of the rotation angle of Glan-Taylor prism, for four polarizations of the seed pulse: 0° (horizontal polarization, parallel to the polarization direction of the pump pulse) (a), 35°, 70° and 90° (vertical polarization).

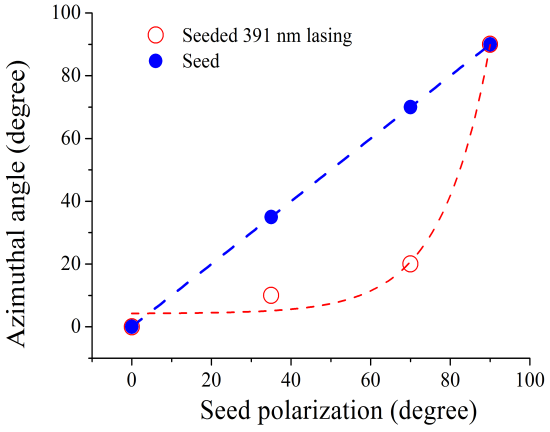

Figure 5.18: The azimuthal angle ϕ of the polarization direction of seeded 391 nm lasing emission as a function of the polarization angle θ of the seed pulse. The azimuthal angle of polarization direction of the seed pulse is equivalent to θ, shown by the dashed blue line. The dashed red line represents an exponential fit to the data of seeded 391 nm lasing emission.

nm lasing emission is plotted as a function of the polarization angle θ of the seed pulse in Fig. 5.18. Naturally the azimuthal angle of the seed polarization is identical to θ, shown by the dashed blue line. We can clearly see that the polarization direction of seeded 391 nm lasing emission is between the polarization directions of the seed and pump pulses as the seed pulse is changed from being parallel to perpendicular to the pump pulse.

This phenomena remains mysterious at this moment. A proposal behind this unexpected experiment result is that the seed pulse experiences strong birefringence during the seed amplification [59]. However, the temporal waveform measurement of the seeded 391 nm lasing emission shows no amplification of the seed pulse itself, as we have already presented in previous subsection 5.4.2. So this proposal actually fails to explain the experimental results. To successfully interpret it, there needs more efforts, including theoretical analysis.

5.5 Gain dynamics of 391 nm lasing emission

As an important aspect of an optical amplifier, the gain dynamics of 391 nm lasing emission was measured in a similar way like in section 3.2 of Chapter 2, in which the amplified signal at 391 nm as a function of relative delay between the pump and seed pulse is measured. Fig. 5.19 shows the gain dynamics results with different seed intensities, ranging from 0.5 mV to 75 mV. Firstly, we look at the result with the seed intensity of 75 mV as shown in upper end panel. It shows an ultrafast gain build-up time $\sim 300\ fs$ and lasts for few picoseconds. Note that the peak in gain dynamics curve positioned at $\sim 4\ ps$. It results from the molecular alignment effect. Here it corresponds to the half-cycle period ($\sim 4.2\ ps$) of the alignment of N_2 molecule after the pump pulse.

There are two regimes shown in Fig. 5.16, e.g. the linear seeding regime and saturation regime. In the former case, the maximal lasing intensity increases and the decay time becomes longer with the increasing seed intensity from 0.5 mV to 10 mV, as shown in Fig. 5.19. By increasing the seed intensity further into the saturation regime, the gain dynamics has no significant change with the increase of the seed intensity. So we get to a conclusion: to measure the complete gain dynamics, it should be performed in the saturation regime.

It is important to note that the ultrafast gain build-up time almost keeps constant as $\sim 300\ fs$ in all the results with different seed intensity. Recalling the gain dynamics of 337 nm lasing emission from neutral nitrogen molecules, its built-up time is normally few picoseconds, much longer than the gain build-up of 391 nm lasing emission. It also depends on the gas pressure, e.g., higher pressures leads to shorter gain built-up time

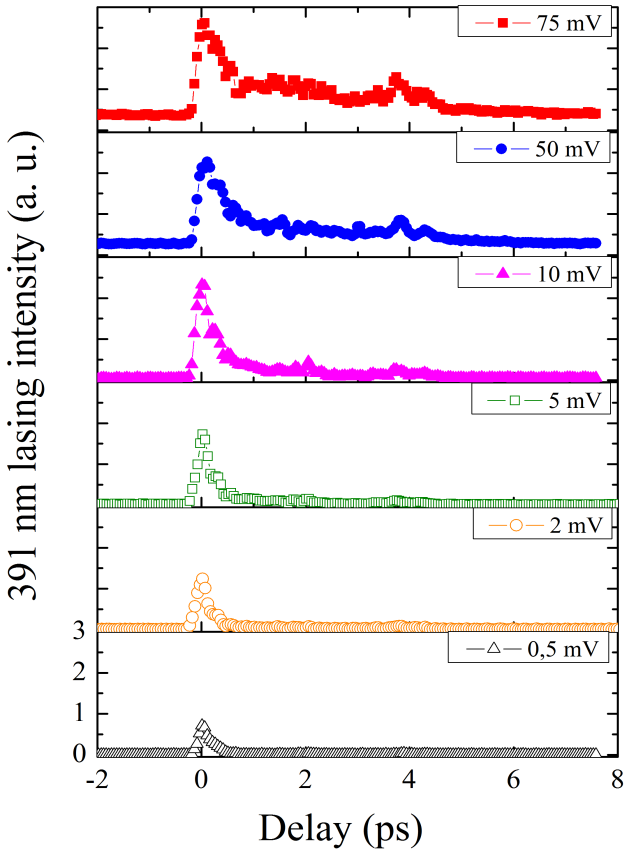

Figure 5.19: Gain dynamics of 391 nm lasing emission for different seed intensity ranging from 0.5 mV to 75 mV. The zero delay is defined as the time when the maximal signal is detected.

because of the collisional excitation process. To examine whether the ultrafast gain build-up time of 391 nm lasing emission depends on the gas pressure or not, we performed the gain dynamics measurement under different pressures, as shown in Fig. 5.20(a) and (b). During the measurements, the pump pulse energy was kept as 1.8 mJ. The gain built-up times, as clearly shown in Fig. 5.20(b), are about $\sim 300\ fs$ and identical under two gas pressures, which indicates this ultrafast gain built-up time is independent of gas pressure. We can see that the gain lasts for 20 ps under low pressure of 10 mbar, while it only lasts for 5 ps under high pressure of 60 mbar. This result excludes the possibility of the inelastic collision excitation, which is responsible for neutral nitrogen lasing, being the gain mechanism of 391 nm lasing emission. With different pump pulse energies, the measured gain dynamics results give the identical build-up time of $\sim 300\ fs$, as shown in Fig. 5.20 (c) and (d). Therefore, there comes a conclusion that the gain build-up time is ultrafast and independent of the seed intensity, the gas pressure and the pump pulse energy.

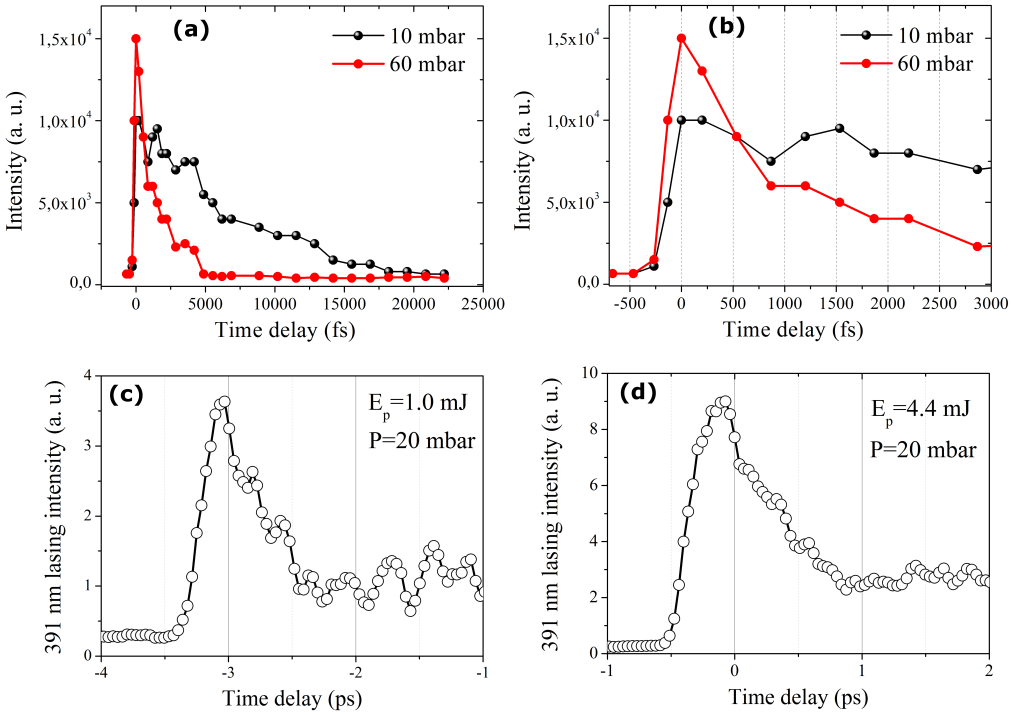

Figure 5.20: (a) Measured gain dynamics of 391 nm lasing emission at 10 mbar and 60 mbar nitrogen gas, respectively. The pump pulse energy was 1.8 mJ. The signal was detected by spectrometer. (b) The details of gain dynamics in the delay range from -500 fs to 3000 fs. (c)-(d) Measured gain dynamics of 391 nm lasing emission with pump pulse energies of 1.0 mJ and 4.4 mJ, respectively. The nitrogen pressure was fixed at 20 mbar.

5.6 Summary

In this chapter, we have studied ionic lasing emissions at 391 nm and 428 nm wavelength in filament plasma created by infrared femtosecond laser pulse. These two emissions belong to the transition $B^2\Sigma_u^+(\nu = 0) \rightarrow X^2\Sigma_g^+(\nu' = 0, 1)$ of the first negative band of singly ionized nitrogen molecule. We focus on studying the 391 nm lasing emission because in many aspects the 428 nm lasing emission possesses quite similar features with 391 nm lasing emission. The lasing emissions at 391 nm have been experimentally characterized by measuring the spectra, spatial profile and divergence, temporal profile, pump energy threshold, gas pressure dependence, and also pump laser ellipticity dependence. The main observations are summarized below:

- Their typical spectrum is composed of two branches, e.g., R-branch and P-branch.

- The 391 nm lasing emission is normally generated at low gas pressure while the 428 nm lasing emission at high gas pressure. The gas pressure range of lasing emission depends on the pump pulse energy and the focusing geometry.

- The pump energy threshold of 391 nm lasing emission was measured to be around 1 mJ.

- For the spatial profiles, the 391 nm lasing beam shows a doughnut-shaped mode with a central maximum while the 428 nm lasing beam a pure doughnut-shaped mode.

- The measurement of two lasing emissions as a function of pump laser ellipticity shows a sensitive dependence on ellipticity, highly similar to HHG. The observed mysterious "dip" needs to be understood while the same feature has been observed in HHG and attributed to different mechanisms.

- In both forward and backward directions, the injection of an external seed pulse can generate strong 391 nm lasing emission. Compare to that in forward direction, the seeded 391 nm lasing in backward direction is more difficult and needs higher pump energy. The forward seeded 391 nm lasing emission saturates when the seed intensity increases to a certain value.

- The polarization direction of seeded 391 nm lasing emission is between the polarization directions of the seed and pump pulses as the seed pulse is changed from being parallel to perpendicular to the pump pulse.

- The gain dynamics measurements of 391 nm lasing emission show a ultrafast gain build-up time of $\sim$ 300 fs, which is independent of the seed intensity, gas pressure and pump pulse energy. For the decay process of the gain, it depends on the pressure in the sense that higher pressures lead to faster decay.

Chapter 6

Lasing of Nitrogen Ions in Air Filament: Interpretation and Discussion

Contents

6.1 Introduction

In previous chapter, we have presented the experimental results as to the lasing emissions of singly ionized nitrogen molecules in filament plasma pumped by linearly polarized 800 nm femtosecond laser pulse in nitrogen and air. Concerning the underlying mechanism of lasing effect from N_2^+ molecule inside filament plasma, it has been discussed in past 5 years and remains controversial up to now. In the first publication that suggesting 391 nm lasing action from filament plasma, population inversion between the upper $B^2\Sigma_u^+$ state and the ground $X^2\Sigma_g^+$ state was proposed [20]. The authors attributed the origin of population inversion to direct ionization of inner-valence electrons of nitrogen molecule in the strong laser field, and claimed that it leads to ultrafast population inversion [20, 23].

By using 1.9 μm mid-IR laser pulse to pump the ambient air, S. Chin *et al* observed the absorption and also amplification of the fifth harmonic around 391 nm wavelength with rather low pump pulse energy of dozens μJ [60]. The authors claimed the existence of population inversion and ascribed it to the fact that the ionization potentials of the outer and inner valence electrons are energetically close to each other. It was argued that the molecules in an excited ionic state not far from the ground state could be ionized and population inversion may be achieved through "nonlinear pumping process including the pump photons and the self-generated harmonic photons".

In experiments by using an optimized sequence of femtosecond pulses at 1.03 μm, the authors tentatively explained their observations through population inversion via a three-photon transition [61]. Later on, it was explained as four-wave mixing (FWM) by the same group [21]. In this scenario, it involves two successive interactions with the non-resonant near-IR pump laser field, one of which is the excitation of the rotational Raman manifold beside the ionization. Another is the subsequent interaction between the pump laser field and a weak resonant UV field (component in supercontinuum) that leads to an automatically phase-matched emission. However, the FWM explanation has been later excluded by an experiment in which the seeded 391 nm lasing emission was observed when the seed pulse counter-propagates with respect to the pump pulse, because the FWM is a parametric process and critically depends on phase matching condition [23].

In 2015, it was reported that population inversion can be established through population exchange (also termed coupling) between the ground $X^2\Sigma_g^+$ state and the excited $A^2\Pi_u$ and $B^2\Sigma_u^+$ states in strong laser field [62, 63]. However, this model seems to be questionable, which will be commented later.

6.2 Populating the upper lasing level: electron recollision excitation

Our experimental results and previous observations in literatures show that there exists a strong forward emission at 391 nm, corresponding to $B^2\Sigma_u^+ \rightarrow X^2\Sigma_g^+$ transition. Therefore, the first question is how the upper level $B^2\Sigma_u^+$ is populated. First, we noticed that direct two-photon excitation of the ion by the pump laser is forbidden due to the angular momentum conservation. A clue to this question is given by the dependence of forward 391 nm lasing intensity on the pump laser ellipticity. Recall the subsection 5.3.6 in Chapter 5, the lasing emission and high-order harmonics show highly similar dependence on the pump pulse ellipticity. The high-order harmonic generation has been well understood by the semi-classical recollision model [53]. Applying the same semi-classical model to our case, we interpret the ellipticity dependence of the lasing emission as being due to a non-radiative transfer of ion population from $X^2\Sigma_g^+$ to $B^2\Sigma_u^+$ state via laser-field-induced recollision.

We consider a semi-classical model of the electron recollision with the parent ion. In each elementary act, an electron in the presence of the intense pump laser is removed from the outer orbital of the neutral nitrogen molecule, accelerated, and then driven back by the laser field to the parent molecular ion where it collides inelastically with an inner orbital electron. During this event, if the impacting electron has a sufficient energy, there is a probability to transfer the inner orbital electron to the outer orbit of the molecular ion. A free electron and an excited molecular ion are left after the event.

In a manner similar to HHG and nonsequential double ionization (NSDI), this excitation process via electron recollision shoud exhibits a strong dependence upon the pump laser ellipticity. It can only occur for returning free electrons with kinetic energy ϵ_e above the excitation energy $\epsilon_{BX} = 3.17\ eV$, the energy threshold to bring the nitrogen molecular ion to the excited $B^2\Sigma_u^+$. This condition is easily met in our experiments. Inside filament plasma, the laser intensity reaches or even exceeds a level of $1.5 \times 10^{14}\ W/cm^2$ [47], which corresponds to a ponderomotive potential (average electron kinetic energy) $U_p = e^2E_0^2/4m_e\omega_0^2 = 9.1\ eV$. All returning electrons with kinetic energy exceeding the threshold can contribute, since the extra energy is carried by the free electron left after the process.

In the following, we present a quantitative calculation based on this model performed by Shihua CHEN (Southeast University, China), its prediction on the pump laser wavelength dependence. Finally, the experiment confirmation of the predication will be presented and discussed.

6.2.1 Tunnel ionization rate

In an analogy to the HHG model, our model also consists of three steps: tunneling ionization of an outer electron, its classic motion in the laser field and recollision excitation from the ground $X^2\Sigma_g^+$ state to the excited $B^2\Sigma_u^+$ state. We first assumed that an electron starts to be ionized at a certain moment τ_0. In the simulation, we need to determine the ionization probability. We adopted the MO-PPT model to calculate the ionization probability because under our situation the Keldysh parameter $\gamma = \sqrt{U_i/(2U_p)} \simeq 0.93$. Basically, if $\gamma << 1$, the MO-ADK [64] works well, while $\gamma \simeq 1$ the MO-PPT model will be better. It takes the form [65] in atomic units

$$w_{MO-PPT} = \frac{B^2(m)}{2^{|m|}|m|!}\frac{A_m(\omega,\gamma)}{\kappa^{2n_{eff}-1}}\left(\frac{2\kappa^3}{F\sqrt{1+\gamma^2}}\right)^{2n_{eff}-|m|-3/2}\exp\left(-\frac{2\kappa^3}{3F}g(\gamma)\right) \tag{6.1}$$

where $\kappa = \sqrt{2U_i}$, $n_{eff} = Z_c/\kappa$, $m = 0$, and F is the instantaneous electric field. For simplicity, we assume the expression $A_m(\omega,\gamma)$ to be unity, i.e., $A_m(\omega,\gamma) \approx 1$. The coefficient $\frac{B^2(m)}{2^{|m|}|m|!}$ is trivial, hence we can completely normalize it. Besides, Z_c is the ionic charge seen by the released electron, $U_i = 15.58\ eV$ is the ionization potential of the N_2 molecule, U_p is the ponderomotive energy, and ω is the laser angular frequency. For numerical calculations, we need to transfer all the formulas in atomic units to those in SI units. To be specific, in all the above formulas, we replace U_i and U_p by U_i/E_h and U_p/E_h respectively, and replace F by F/E_{au}, ω by ω/ω_{au}, where

$$E_h = \frac{e^2}{4\pi\epsilon_0 a_B},\ a_B = \frac{4\pi\epsilon_0\hbar^2}{m_e e^2},\ E_{au} = \frac{E_h}{e a_B},\ \omega_{au} = \frac{eE_{au}a_B}{\hbar}, \tag{6.2}$$

defining the Hartree energy, Bohr radius, atomic electric field, and atomic frequency, respectively. Figure 6.1 shows the ionization rate of nitrogen molecule for an unchirped Gaussian laser field.

6.2.2 Electron dynamics in laser field

Once the electron is tunneled out, its trajectory then is calculated from the solution of the Newton equations for the ionized electron moving in the laser field:

$$\frac{dx_e}{d\tau} = Tv_e, \tag{6.3}$$

$$\frac{dv_e}{d\tau} = -\frac{eT}{m_e}E_x(\tau) \tag{6.4}$$

where x_e and v_e are the trajectory and the velocity of electron, e and m_e are the elementary charge and electron mass respectively, and T is the oscillation period of laser

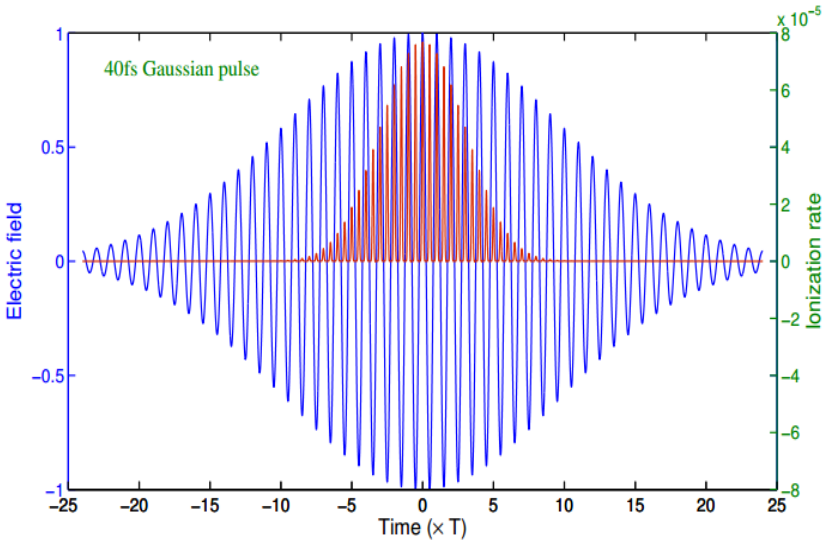

Figure 6.1: Calculated laser electric field and ionization rate of N_2 molecule from Eq. (6.1) for unchirped Gaussian laser field.

field. These linear equations are integrated for given initial conditions: $v_e(\tau_0) = 0$ and $x_e(\tau_0) = 0$. We consider the laser electric field as a product of a Gaussian envelope and a carrier wave, which reads

$$E_x(\tau) = \frac{E_0}{2\sqrt{1-iC}} \exp\left[-2i\pi\tau - \frac{2\ln 2\tau^2}{\alpha^2(1-iC)}\right] + c.c. \tag{6.5}$$

where E_0 is the laser field amplitude, C is the chirp parameter, α is the number of optical cycles of initial unchirped pulse and $c.c.$ denotes the complex conjugate. By input the electric field Eq.6.5 into the Newton equations, we can get analytic solutions for the velocity and trajectory of electron:

$$v_e = \frac{M\sqrt{\pi}e^{-\pi^2/\eta}}{4\sqrt{\eta}\sqrt{1-iC}}\left[\mathrm{erf}(\frac{\eta\tau_0 + i\pi}{\sqrt{\eta}}) - \mathrm{erf}(\frac{\eta\tau + i\pi}{\sqrt{\eta}})\right] + c.c. \tag{6.6}$$

$$x_e = T(\tau + i\pi/\eta)v_e - \frac{TM(e^{-\eta\tau^2 - 2i\pi\tau} - e^{-\eta\tau_0^2 - 2i\pi\tau_0})}{4\eta\sqrt{1-iC}} + c.c. \tag{6.7}$$

where $\eta = 2\ln 2/[\alpha^2(1-iC)]$, $M = eTE_0/m_e$, and erf is an error function of the complex variable. Figure 6.2 shows the calculated electron trajectory and velocity in laser field for electrons born at three different positions, i.e., peak A ($\tau_0 = -0.9991$), peak B ($\tau_0 = 0$) and peak C ($\tau_0 = 0.9991$), respectively. For electrons born at peak A, the electron recollides with the parent ion for many times, while for electrons born at peak B, there is just one collision with its parent ion with zero recollision energy because of zero velocity. For electrons born in peak C, they just drift away and never come back to its parent ion.

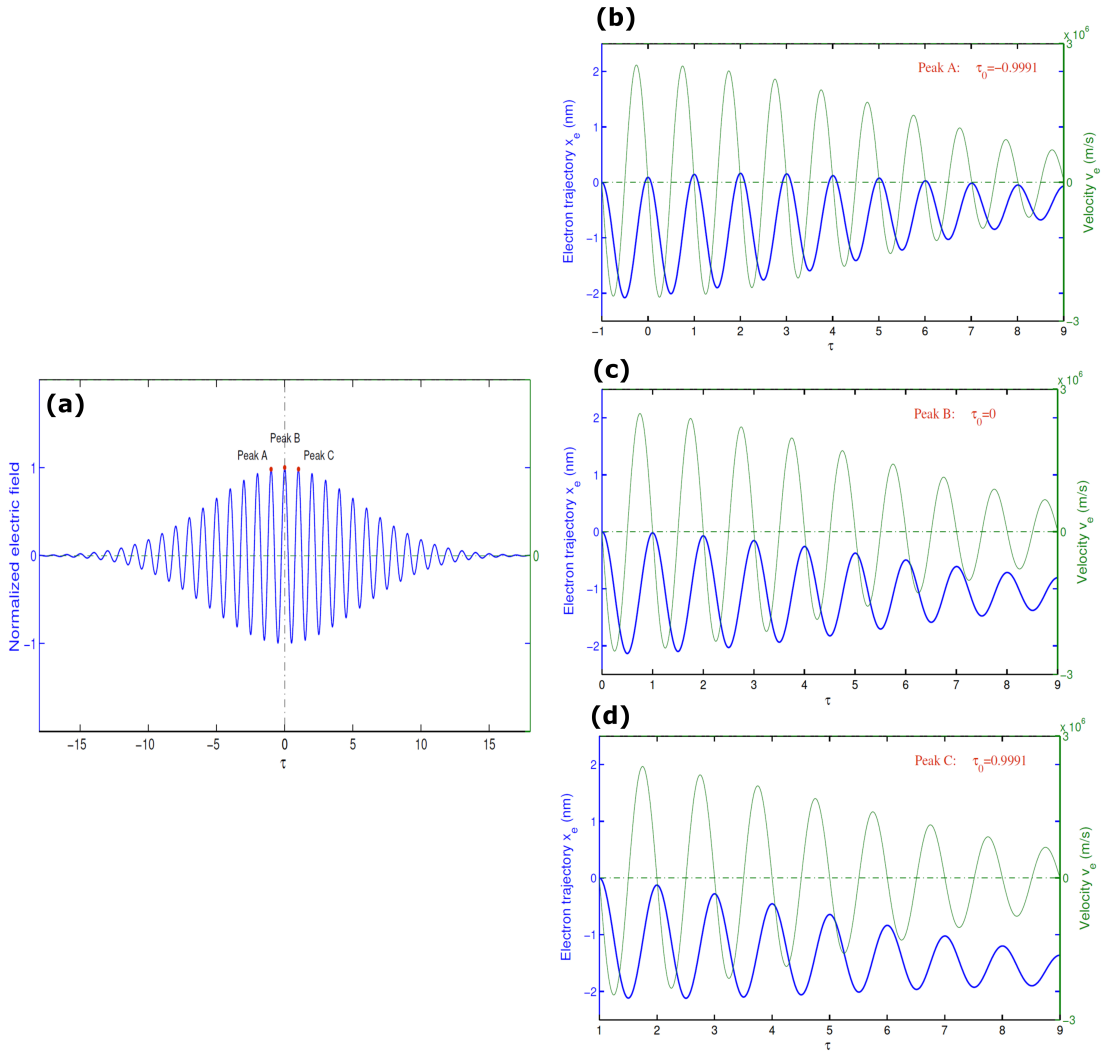

Figure 6.2: Calculated electron trajectory and velocity in laser field for electrons born at three different positions, peak A ($\tau_0 = -0.9991$), peak B ($\tau_0 = 0$) and peak C ($\tau_0 = 0.9991$) respectively.

6.2.3 Electron recollision excitation

For electrons born in some phase interval, it is possible to return back to the parent ion (see Fig. 6.2(b)), resulting in recollision excitation. The transition amplitude a_{XB} from the ground $X^2\Sigma_g^+$ state to the excited $B^2\Sigma_u^+$ state is described by the Schrödinger equation

$$i\frac{da_{XB}}{dt} = V_{XB}(\epsilon_e)\exp(-i\omega_{XB}), \tag{6.8}$$

where $V_{XB}(\epsilon_e)$ is the matrix element of the ion transition to the excited $B^2\Sigma_u^+$ state in a collision with an electron having the energy ϵ_e. In our case this excitation is produced by an electron ionized at the time $t = t_0$ and oscillating around the parent ion in the laser field. The matrix element can be presented as a sum of instantaneous perturbations at the moments of collision t_s, i.e., $V_{XB} = V_1\delta(t - t_s)$ where the index s is an integer

numbering the subsequent collisions. The matrix element V_1 is in general a function depending on the electron energy. For simplicity, we consider it here as a step function

$$V_1 = V_0 H(\epsilon_e - \epsilon_{XB}), \tag{6.9}$$

where $H(x)$ is the Heaviside step function. The V_0^2 can be considered as the probability of ion excitation in a single collision with an electron. Then by integrating Eq. (6.8) over time one obtains the following expression for the transition amplitude:

$$a_{XB} = V_0 \sum_s \mathrm{sgn}(v_e^s) e^{-i\omega_{XB} t_s}, \tag{6.10}$$

where the summation is taken over all collisions where the electron energy verifies the condition $\epsilon_e(t_s) > \hbar\omega_{XB}$. In terms of normalized time units, the probability amplitude can be rewritten as

$$a_{XB} = V_0 \sum_s \mathrm{sgn}(v_e^s) e^{-i2\pi\tau_s \omega_{XB}/\omega_0}, \tag{6.11}$$

where $\mathrm{sgn}(v_e^s)$ is the sign symbol determining the recollision direction at the recollision moment, which equals to ± 1. With the ionization probability being considered and meanwhile taking only the first recollision into account ($s = 1$) due to electronic wavepacket dispersion, the total excitation probability can be given by

$$W_{XB} = |a_{XB}|^2 = V_0^2 \left| \sum_{\tau_0} \mathrm{sgn}(v_e^s) w_{fi}(\tau_0) e^{-i2\pi\tau_s(\tau_0)\omega_{XB}/\omega_0} \right|^2 \tag{6.12}$$

where $w_{fi}(\tau_0)$ is the ionization probability at the moment τ_0, and $\tau_s(\tau_0)$ is the first recollision time for electron starting at τ_0.

From the above total probability formula, we can see that the carrier frequency ω_0 will change with the pump wavelength, which is for sure. The ionization probability ω_{fi} also change with wavelength, but in a slight manner. In addition, the first recollision time $\tau_s(\tau_0)$ and the recollision direction do not depend on the wavelength. Thus, we expect that the total excitation probability depends on the wavelength, mainly through the carrier frequency ω_0.

We have calculated numerically the Eq.(6.12) for varying pump laser wavelength. Figure 6.3 shows the pump wavelength dependence of the simulated total excitation probability of $X^2\Sigma_g^+ \rightarrow B^2\Sigma_u^+$ transition for different durations of pump laser pulses. First we notice that the total excitation probability at resonant wavelength of 782 nm (twice the 391 nm) is zero. This is expected since the excitation probabilities by recollision events from opposite sides exactly cancel each other in the case of resonant wavelength. It is

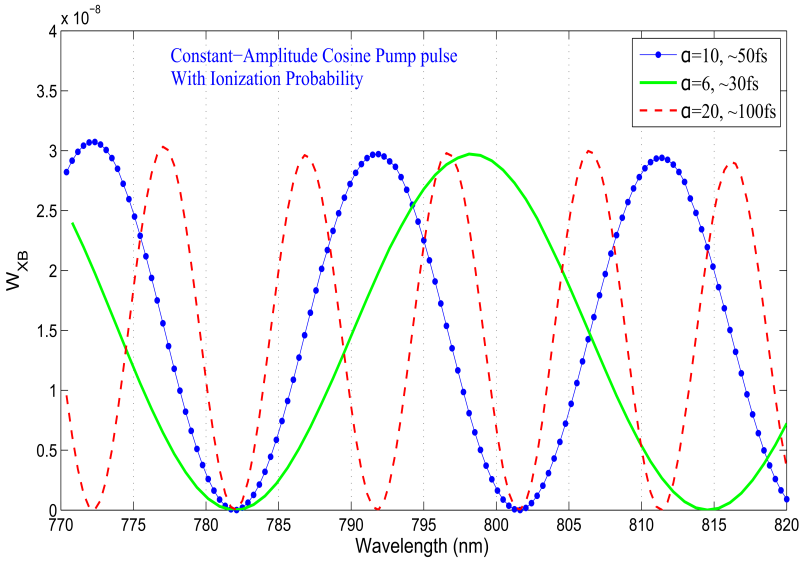

Figure 6.3: Simulated total excitation probability as a function of pump laser wavelength for three different numbers of optical cycles, i.e., $\alpha = 6,\ 10,\ 20$, corresponding to pulse durations of ∼30 fs, ∼50 fs and ∼100 fs, respectively.

in analogy to the fact that there is no even harmonics can be generated in HHG in gas medium. More important, we can see clearly that the total excitation probability shows a periodic dependence on the pump wavelength, and the period depends on the duration. For instance with $\alpha = 10$, the case close to our situation, the wavelength period equals to 20 nm.

6.2.4 Confirmation of recollision excitation: pump laser wavelength dependence

To experimentally confirm the recollision excitation mechanism, we performed an experiment to examine the dependenc of 391 nm lasing emission on pump laser wavelength. This experiment was performed in the group of Anne L'Huillier in Lund University, funded by a collaborative Laserlab project. In the experiments, we focused 1 kHz infrared laser pulses with maximal energy ∼ 1.10 mJ into a gas chamber filled with nitrogen gas, and detected the forward lasing emission after suitable bandwidth filters. The central wavelength of laser pulse can be tuned from 780 nm to 820 nm with an adjustable bandwidth. Figure 6.4 shows the tunability of spectral profile of the laser source.

Figure 6.5 shows the results measured in cases of three different pulse durations, respectively 35 fs, 40 fs and 50 fs. First, it is clearly noted that no 391 nm lasing emission can be detected when the central wavelength decreased down to the limited position around 782 nm in all these measurements, which agrees remarkably with the

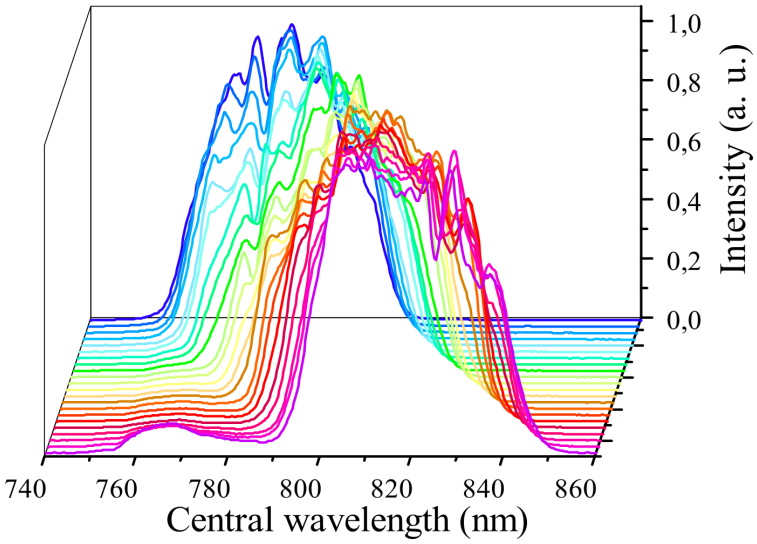

Figure 6.4: Tunability of the central wavelength of the 1 kHz infrared laser source with keeping a bandwidth of about 50 nm and pulse duration of 40 fs. The various colors represent different settings in the laser system.

theoretical prediction (see Fig. 6.3). Secondly, the 391 nm lasing emission shows a periodic dependence on the central wavelength of pump laser pulse. With longer central wavelength, the period becomes shorter. For instance, there are approximately three periods in the case of 50 fs measurement, separated by about 12.5 nm that is averaged for peak positions. For 40 fs measurement, there exists two periods, separated by about 15.5 nm. For 35 fs measurement, the second peak is not reliable because of lacks of data points. So only one period will be considered, which can be estimated as 30 nm. This experimental observation agrees qualitatively with the simulation results shown in Fig. 6.3, namely the periodic dependence and the minimum at resonant wavelength of 782 nm, even though there is difference in the absolute amplitude.

Figure 6.6 shows 391 nm fluorescence signal as a function of central wavelength of pump laser pulse. The fluorescence was generated in gas cell fueled with 9 mbar nitrogen and collected in side direction by a fiber pointer mounted to the gas cell. By contrast to forward lasing emission, the 391 nm fluorescence does not show a significant variation for different wavelengths, indicating that most of the population in the $B^2\Sigma_u^+$ state is actually not relevant to lasing effect. This can be expected from the tunneling ionization process.

According to the simulation results shown in Fig. 6.3, we can notice that the product of pump pulse duration and the wavelength period is a constant $C = 100\ fs \times 10\ nm = 50\ fs \times 20\ nm \approx 30\ fs \times 32\ nm$. Thus, the dependence of total excitation probability on the central wavelength of pump laser pulse can be analytically expressed as

$$f(\lambda) = A\sin^2(\pi\tau_p \frac{\lambda - 782}{C})$$

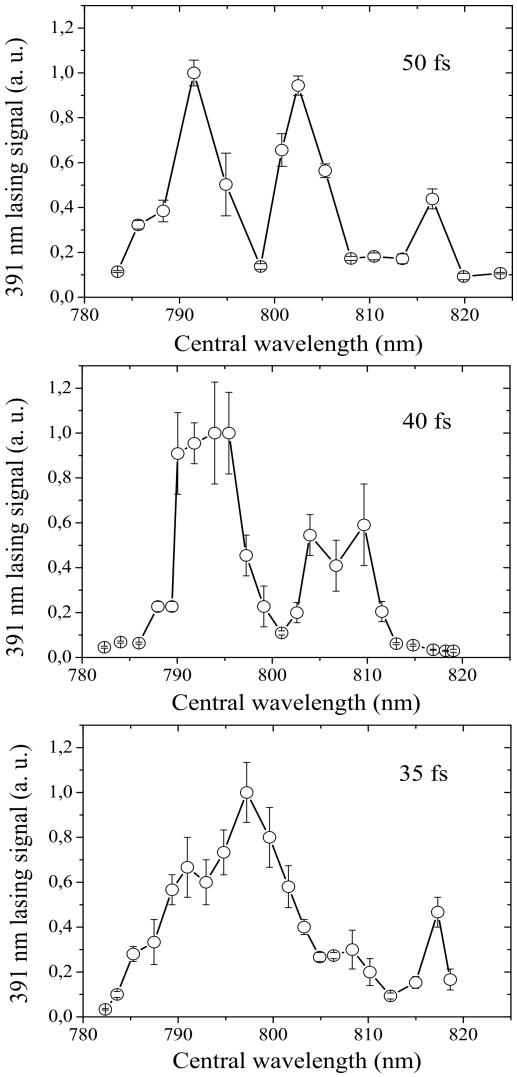

Figure 6.5: Measured forward 391 nm lasing intensity as a function of central wavelength of pump laser pulse for three different pulse durations, respectively 35 fs, 40 fs and 50 fs. In the case of 35 fs duration, the pump pulse energy is about 0.38 mJ and the nitrogen gas pressure was kept at 5 mbar. In the case of 40 fs duration, the pump energy can be maximal as 1.1 mJ and the pressure was kept at 2.5 mbar. In the case of 50 fs, the pump pulse energy is 0.7 mJ and the gas pressure was 5 mbar. The detector we used is a calibrated photodiode.

where A and τ_p represent the amplitude of total excitation probability and the pump pulse duration, respectively. Given $\lambda = 800\ nm$, it gives $f(800\ nm) = Asin^2(\pi\tau_p/55.6)$ which peaks at 27.8 fs.

To confirm that experimentally, the dependence of 391 nm lasing energy on the pump pulse duration was measured while keeping the central wavelength at 800 nm. By varying the laser pulse energies, the laser intensities inside filament were almost fixed at the same value. In this case, other nonlinear effects due to the change of laser intensity can be excluded. The durations of pump laser pulses can be varied from 21.5 fs to 40.2 fs, and the corresponding spectra are shown in Fig. 6.7(a). The measured results under

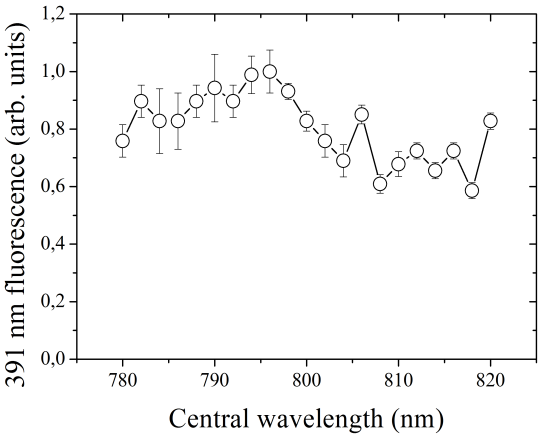

Figure 6.6: The side fluorescence signal at 391 nm as a function of pump laser wavelength. This experiment was performed in gas jet in order to collect the side fluorescence by using a fiber pointer. The pulse duration of pump laser is 35 fs.

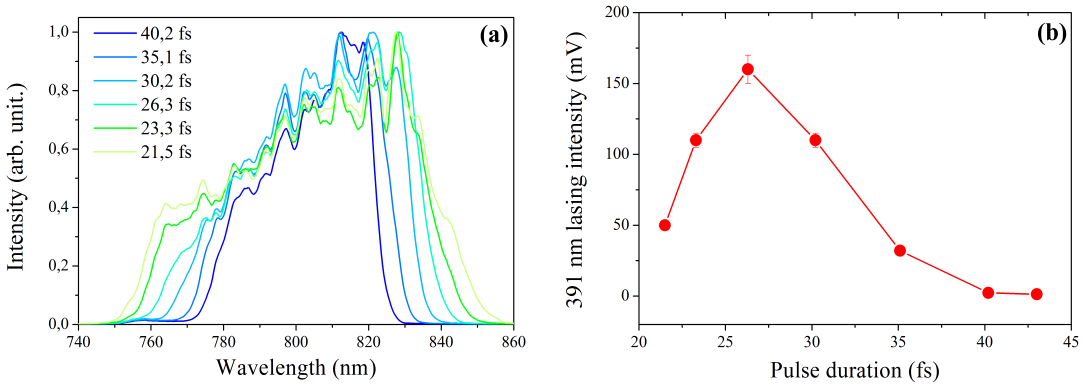

Figure 6.7: (a) The spectra of pump laser pulses with same central wavelength of 800 nm but different durations (or bandwidths) ranging from 21.5 fs to 40.2 fs. The laser intensity in filament for each pulse was kept almost as $8 \times 10^{13}\ W/cm^2$ by assuming the diameter of filament inside gas chamber as 100 μm. (b) The measured 391 nm lasing energy as a function of pulse duration of pump laser. The nitrogen gas pressure is at 5.5 mbar.

5.5 mbar nitrogen is shown in Fig. 6.7(b). It shows a peak at 26.3 fs, quite close to the simulation result of 27.8 fs. Also, it decreases with longer or shorter pulse durations, which agrees with the tendency of $sin^2(\pi\tau_p/55.6)$ function. So, the experiment result is in good agreement with the simulations.

To conclude, the experiment on the pump wavelength dependence of 391 nm lasing intensity shows good agreement with the simulation results, confirming that the recollision excitation is essential to nitrogen ionic lasing in femtosecond filaments.

6.3 Nature of nitrogen ion lasing: superradiance

In previous chapter, we have measured the temporal waveforms of 391 nm lasing pulse in both self-seeding and external-seeding regimes. As we mentioned before, the pressure dependence of temporal profile strongly suggests superradiance (SR). In this section, we first introduce basic concept of superradiance. Then, we extract the duration, the delay with respect to the pump pulse and the peak intensity as a function of gas pressure. It shows very good agreement with the predictions of superradiance theory. Based on that, we concluded that the 391 nm lasing emission in filament plasma is essentially superradiance. Finally, more experimental evidences proving above conclusion will be presented.

6.3.1 Introduction of superradiance

Superradiance refers to the cooperative spontaneous decay of an ensemble of inverted atoms or molecules [51, 66]. It is well known that spontaneous emission results from the interaction between the excited states with the vacuum fluctuations of the electromagnetic field, which yields the usual exponential decay with a characteristic time τ_{sp} as shown in Fig. 6.8(a). The spontaneous decay of the atomic sample is not correlated and therefore its radiation pattern is essentially isotropic. In 1954 Dicke [66] realized that the interaction among the atoms through their common radiation electromagnetic field should result in a correlation between the atomic dipole moments, if the phases of the atomic dipoles are unaffected by random changes owing to other interactions such as collisions, thermal noise etc. In this way, a macroscopic polarization is created which is proportional to the number of atoms N. This multi-atomic system radiates collectively, and the radiation is then coherent. The temporal shape of this collective emission pulse is no longer exponential but has a peak after a certain delay as shown in Fig. 6.8(b). The decay time and duration of this collective emission pulse is proportional to $1/N$, and its peak intensity is proportional to N^2. These are the most characteristic features of superradiance. In reality, superradiance is always in competition with the spurious dephasing effects such as spontaneous emission on other transitions, Doppler dephasing, atomic collisions and so on, which are treated as an ensemble characterized by the dephasing time T_2.

Superradiance was first considered for the unrealistic case where the spatial extent of the inverted medium in any direction is shorter than the transition wavelength λ_0. In practical experiment, this ideal superradiance is very difficult to realize. Most of superradiance experiments were achieved by samples having a volume with dimensions much larger than λ_0. In these samples, despite the dephasing effect, the propagation

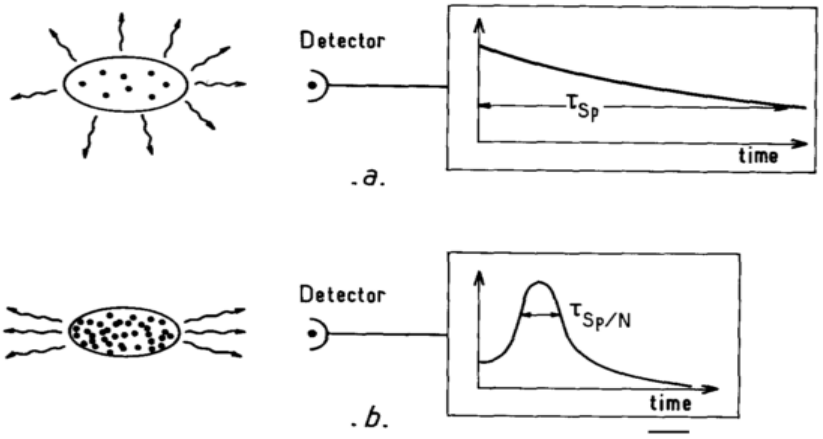

Figure 6.8: Comparison between the general characteristics of spontaneous emission and superradiance. (a) Ordinary spontaneous emission is essentially isotropic with an exponentially decaying intensity (time constant τ_{sp}). (b) Superradiance is anisotropic with an emission occurring in a short burst of duration $\sim \tau_{sp}/N$ where N is the atom number. Courtesy to the literature [51].

and diffraction effects are also needed to be taken into account in the prediction of experimental observations, which makes superradiance is in general a three-dimensional nonlinear problem. An important step in the simplification of this problem is to consider the so-called pencil-shaped sample, from which superradiance has been realized in most experiments so far. It is the "natural shape" for a superradiant medium prepared by a pulsed pump laser beam acting on a gas sample [51]. It has been proved that the superradiance is a one-dimensional problem if the Fresnel number of the pencil-shaped sample

$$F = \pi w^2/l\lambda_0 \approx 1,$$

where w is the transverse radius and l is longitudinal length of the sample. This allow us to describe qualitatively the effects of propagation along the sample and the complications due to the transverse variation of the field being neglected.

Concerning the few-centimeter-long, $100 \sim 200\mu m$-wide filament plasma we created in nitrogen or air by using IR femtosecond laser pulse and the ionic lasing emission at 391 nm wavelength, the Fresnel number can be calculated as $F \sim 1.34$, well matching aforementioned requirements for qualitatively describing the superradiance. For this kind of cylindrical, pencil-shaped sample, the temporal width of superradiance is given by

$$\tau_R = \frac{8\pi}{3\lambda_0^2 \Gamma \rho l}, \tag{6.13}$$

where Γ is the natural decay rate of the transition, ρ the number density of excited atoms or molecules [67]. The τ_R is inversely proportional to the filament length l, and ρ and

therefore the gas pressure p. The delay τ_D with respect to the pump pulse is given by

$$\tau_D = \tau_R \frac{(\ln\sqrt{2\pi N})^2}{4}, \tag{6.14}$$

where $N = \rho V$, and V is the volume occupied by the excited sample.

6.3.2 Experiment evidences of 391 nm superradiance

Now, we will re-examine our experiment results and some results from other groups in the light of superradiance. We will also show that it is possible to coherently control this superradiant emission.

6.3.2.1 Pressure dependence of the temporal profile of 391 nm lasing pulse

Within the pressure range from very low pressure to the optimal pressure, the temporal evolution of 391 nm lasing pulse with the increasing pressure reminds one the features of superradiance (see Fig. 5.8). We extract the peak intensities of 391 nm lasing pulses from measured temporal profiles presented in Fig. 5.8, and plotted them as a function of nitrogen pressure. The radiator number N is proportional to the gas pressure p. Fig. 6.9 shows the result. It is fitted by the expression $\tau = ap^b + c$, where c accounts for arbitrary offset. The fitted exponent is 2.01 ± 0.45, where the errors have been estimated from the variation of χ^2. It is quite well consistent with the deduction of superradiance theory.

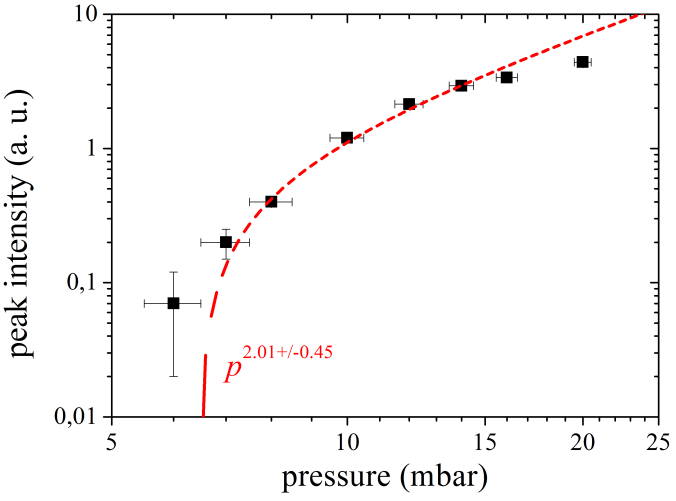

Figure 6.9: The extracted peak intensity from the temporal profiles of 391 nm lasing pulses as a function of nitrogen pressure. The dashed line presents the fitting by expression form $ap^b + c$, where p denotes the pressure.

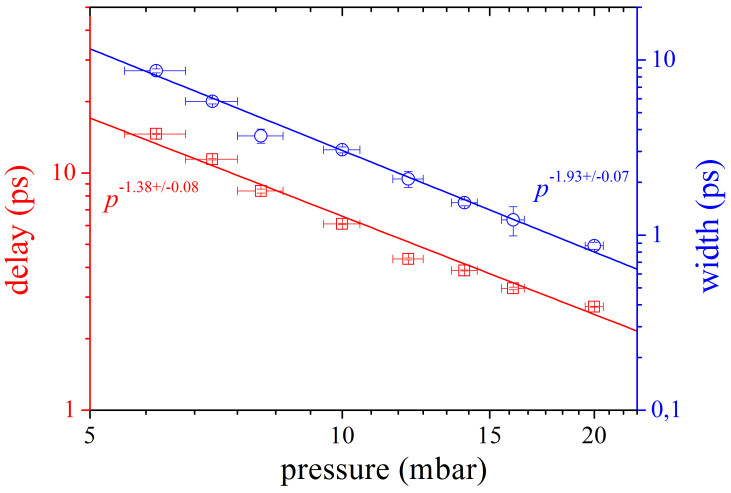

Figure 6.10: Pressure dependence of the pulse width and delay of 391 nm lasing emission in filament plasma in nitrogen.

We also extracted the pulse width and relative delay from measured temporal profiles presented in Fig. 5.8, and plotted them as a function of nitrogen pressure, as shown in Fig. 6.10. They have been well fitted by the expression $\tau = ap^b + c$. The fitted exponents are -1.93 ± 0.07 for the pulse width, and -1.38 ± 0.08 for the delay. These two exponents, however, deviate from the predicted $1/N \approx 1/p$ dependence of superradiance. We believe that this is because of the self-seeded nature of 391 nm lasing emission, where the 391 nm lasing is initiated by weak second harmonics generated inside the filament plasma. The intensity of this weak second harmonic varies with the gas pressure, resulting in a complicated dependence of 391 nm lasing pulse on pressure rather than the $1/p$ dependence.

In the external-seeding regime, we obtained significant enhancement of lasing signal and also improved temporal profile measurements of 391 nm lasing emission (see Fig. 5.14). As we have done before, the pulse width, relative delay and peak intensity of externally-seeded 391 nm lasing pulse were extracted, and plot as a function of nitrogen pressure, as shown in Fig. 6.11. They are also fitted by the expression $\tau = ap^b + c$. The fitted exponents are -1.27 ± 0.03 for the pulse width, -1.41 ± 0.03 for the delay, and 2.39 ± 0.06 for the peak intensity. These values agree well with the prediction of superradiance.

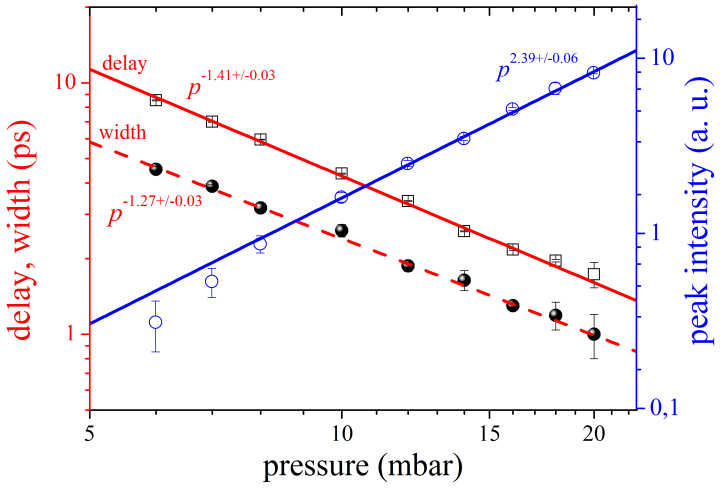

Figure 6.11: Pressure dependence of the pulse width, delay and peak intensity of externally-seeded 391 nm lasing emission. The solid lines are fitting of the form $ap^b + c$ to the extracted delay and width.

6.3.2.2 Filament length dependence of temporal profile of 391 nm lasing pulse

Except our temporal waveform measurements of 391 nm lasing emission, another independent evidence of superradiance has been reported by Li *et al.* in Ref [68]. They have measured the temporal waveforms of 391 nm lasing pulses for different filament lengths, as shown in Fig. 6.12. In their experiment, the filament plasma length can be controlled by two movable thin steel plates mounted in a gas chamber. The length of $l = 0$ mm actually corresponds to an real filament plasma length of ~1.5 mm, the starting length where the cross-correlation signal can be merely measured. We can see that the 391 nm lasing pulse shows gradually oscillation structures when the filament plasma length becomes longer. Thus the "duration" τ_R of 391 nm lasing emission was defined as the duration of the first strongest pulse, as denoted in Fig 6.12. Clearly τ_R becomes shorter while the filament plasma is longer, and in fact inversely proportional to the filament plasma length, which agrees well with the formula 6.13 of superradiance pulse. Besides, an apparent time delay between the 391 nm lasing pulse and the seed pulse can be observed, also indicating superradiance. The oscillation can be understood in the framework of seed-triggered superradiance. The radiant pulse length $L_p = c\tau_R \simeq 1.5$ mm by taking $\tau_R = 5$ ps. When $l > L_p$, the propagation effect will be present and the whole gain medium may undergo re-absorption and re-emission processes, leading to the lasing signal oscillation in the time domain [69].

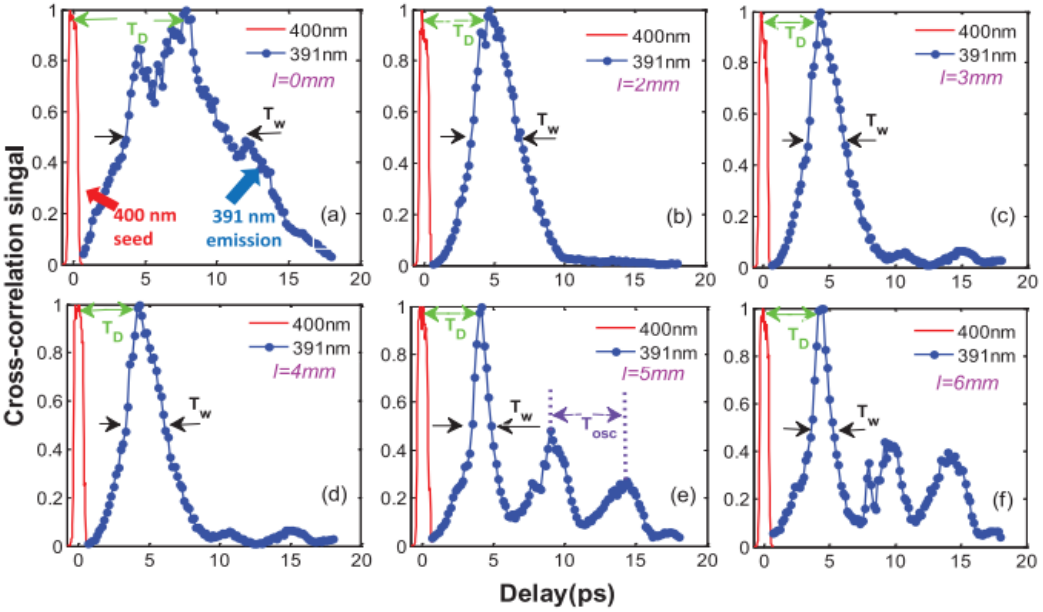

Figure 6.12: Measured temporal waveforms of 391 nm lasing pulses for the plasma channel lengths of (a) 0 mm, (b) 2 mm, (c) 3 mm, (d) 4 mm, (e) 5 mm, (f) 6 mm, respectively. The red solid line represents the cross-correlation signal between the 800 nm and 400 nm seed pulses, pointing the time of the pump pulse. Courtesy to Ref [68].

6.3.2.3 Coherent control of 391 nm lasing emission

Another evidence of 391 nm lasing emission being superradiance was performed by our collaborators A. Li, M. L. Lei and H. B. Jiang in Peking University. An 800 nm pump laser pulse is used to create a filament plasma in nitrogen gas, and then two external 391 nm seed pulses are injected in the same propagation direction of pump laser pulses. The final signal was detected by a sensitive spectrometer. Fig. 6.13 shows the 391 nm emission intensity as a function of relative delay between the two successive seed pulses. The relative delay between two seed pulses is around 2 ps and it was varied nearby with a precision of 40 as (1 as = 0.001 fs). The final 391 nm signal shows a strong oscillation with 1.3 fs period, which corresponds to the period of 391 nm emission. This result can be only well understood in the framework of superradiance. The 800 nm pump laser pulse creates the filament plasma and prepares the gain medium. The injection of first seed pulse triggered the build-up of macroscopic polarization in the gain medium, leading to superradiance (see Fig. 5.14). Then, the interaction between the macroscopic polarization and the delayed second seed pulse must be a phase-dependent process. As a result, the phase-dependent enhancement or reduction of 391 nm emission can be expected.

To summary, based on above three experimental measurements, namely the temporal waveforms of 391 nm lasing pulse for different gas pressure and filament length,

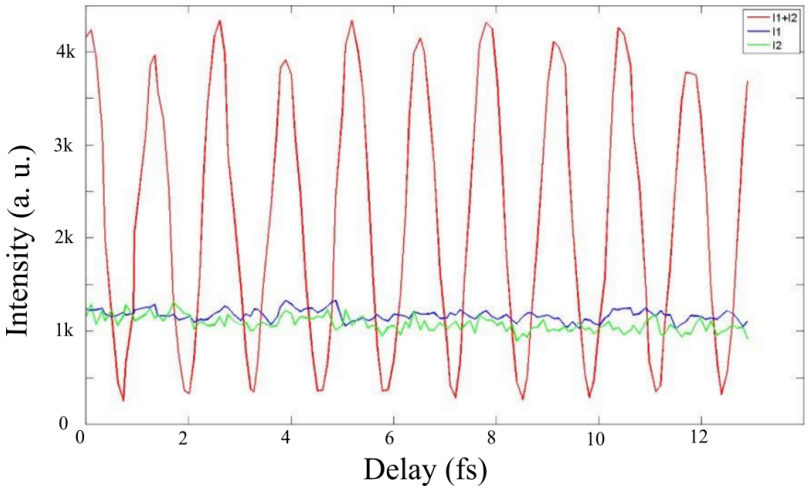

Figure 6.13: Coherent control of the 391 nm lasing emission in double (red line) and single (violet and green lines) seeding scheme. The oscillation period in this figure is about 1.3 fs, the period of 391 nm emission. The nitrogen pressure was 4 mbar.

and direct confirmation of the existence of macroscopic polarization, we conclude that the observed 391 nm lasing emission in filament plasma created by 800 nm femtosecond laser pulse in nitrogen or ambient air is superradiance.

6.4 How is optical gain possible ?

In the above, we have seen that an external injected seed pulse at 391 nm can be significantly amplified in term of its energy. This requires an optical gain. At the mean time, superradiance behavior has been studied theoretically and predicted only in the presence of optical gain. Therefore, it is necessary and important to clarify the origin of the optical gain in our current N_2^+ system, in addition to addressing the populating mechanism of the upper lasing $B^2\Sigma_u^+$ state. In this section, we will first introduce two gain mechanisms that has been proposed in the literature by different groups: population inversion and transient molecular alignment. Later, we discuss our proposal of lasing without inversion. In this part, several characteristic experimental features will be examined in the framework of lasing without inversion.

6.4.1 Proposed gain mechanism I: Population inversion

Superradiance has been widely accepted as the cooperative spontaneous decay of an ensemble of inverted atoms or molecules, i.e. superradiance usually requires population inversion. Naturally, several publications have proposed that there exists population inversion between the ground $X^2\Sigma_g^+$ state and the excited $B^2\Sigma_u^+$ state for 391 nm superradiance. Recently, it was reported that population inversion can be built through

population exchange (also termed as "coupling") between the ground $X^2\Sigma_g^+$ state and the excited $A^2\Pi_u$ and $B^2\Sigma_u^+$ states [62, 63]. As shown in Fig. 6.14, in this theoretical

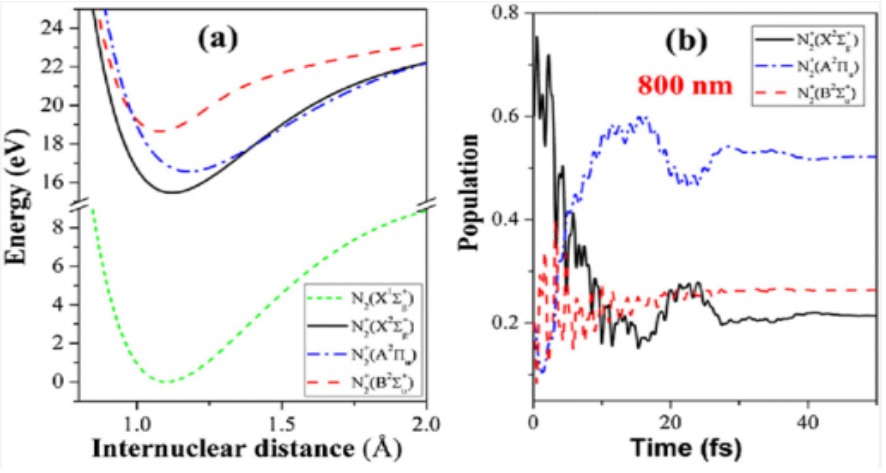

Figure 6.14: (a) Potential energy curves of the electronic states of N_2 and N_2^+ molecules. (b) The temporal evolution of the population distributions in the electronic states of N_2^+ in the 800 nm laser field with an intensity of 2.2×10^{14} W/cm^2. Courtesy to the Ref. [63].

consideration, the population mainly distributes in the ground state after the ionization. The following laser fields cause the population transfer between the ground state and the two excited states, $A^2\Pi_u$ and $B^2\Sigma_u^+$ states via a Rabi oscillation process. At the end of the laser pulse, the population in the $A^2\Pi_u$ state is significantly increased, while that in the $X^2\Sigma_g^+$ state is greatly decreased. As a result, the final population in the $B^2\Sigma_u^+$ state may become larger than that in the ground $X^2\Sigma_g^+$ state.

In the simulations, the time-dependent Schrödinger equation was numerically solved for the nuclear wave function of N_2^+. However, we found out that there are several possible problems in above modeling and numerical simulations. First, in the simulation the off-diagonal elements of the density matrix, which represent the coherence (dipole momentum) between the states, have been neglected. In the case of ultrafast laser pulse pumping (faster than the decoherence time), we should consider the coherence between the interested states rather than only the population distribution. Second, the formula used for off-diagonal elements $\mu_{XB}E(t)$ is only applicable for single photon excitation. However, the single photon excitation from $X^2\Sigma_g^+$ to $B^2\Sigma_u^+$ state is unlikely by using 800 nm laser pulse because the photon energy (~1.5 eV) is much less than the transition energy (~3 eV). Finally, in these numerical simulations, population inversion between the $B^2\Sigma_u^+$ and $X^2\Sigma_g^+$ states is established due to that most of the population is stored in the $A^2\Pi_u$ state. However, a very recent conference report based on fs-CARS technology show that there is no observable population distribution in the $A^2\Pi_u$ state while that in both $X^2\Sigma_g^+$ and $B^2\Sigma_u^+$ state are experimentally observed [70]. All these facts call this population inversion proposal into question.

6.4.2 Proposed gain mechanism II: Transient rotational alignment

Regarding on the gain mechanism of ionic lasing emission, D. Kartashov *et al* proposed an explanation in terms of transient rotational alignment of the ground and excited states leading to optical gain in the absence of population inversion [71]. In their experiments, pump laser pulses at 1.03 μm and 3.09 μm wavelengths were used to generate 391 nm lasing emission. In this circumstance, resonant population transfer from the ground state to excited state was thought of being enabled by absorbing photons from the supercontinuum and the 3^{rd} and 9^{rd} harmonics of the driving laser pulses, respectively. The authors claimed that the optical gain of 391 nm lasing effect is not only determined by the populated numbers of N_2^+ ions in excited state but also by the spatial overlap of the wavefunctions of the excited and ground states. Basically, their idea is following: after the passage of the pump laser pulse, more N_2^+ molecules are in the ground $X^2\Sigma_g^+$ state and few in the excited $B^2\Sigma_u^+$. There is no population inversion. However, the number of aligned N_2^+ molecules in the excited state could be larger than those in the ground state. The probability wavefunction of the $B^2\Sigma_u^+ \rightarrow X^2\Sigma_g^+$ transition is supposed to be proportional to the product of the population and the orientation factor, i.e.

$$W_{down} \propto \langle \cos^2(\theta) \rangle_B P_B$$

where $P_{\mathbf{B}}$ denotes population in the upper state. For up-transition (i.e, absorption), $W_{up} \propto \langle \cos^2(\theta) \rangle_X P_X$. It is possible that $W_{down} > W_{up}$ can be fulfilled even though $P_B < P_X$, in the case that orientation factor compensate the lack of population inversion. As shown in Fig. 6.15, the orientation factors for the ground and excited states evolves differently in time, so that the probability of downward transition prevails the absorption in a transient time window less than 1 ps, which leads to 391 nm emission.

However, this explanation fails to explain the main feature of gain dynamics measurement of 391 nm lasing emission pumped by 800 nm laser pulses (see Fig. 5.19). The measured gain dynamics shows an ultrafast build-up and relatively slow decay of tens of picoseconds that depends on experiment conditions. However, the above hypothesis predicted only a series of narrow (<1 ps) temporal window for optical gain. At the mean time, we would like to point out that the molecular alignment really plays a role for this 391nm lasing, since the signature of molecule alignment revival is observed in both the gain dynamics and temporal profile of the emission. However, it is not the essential factor enabling optical gain.

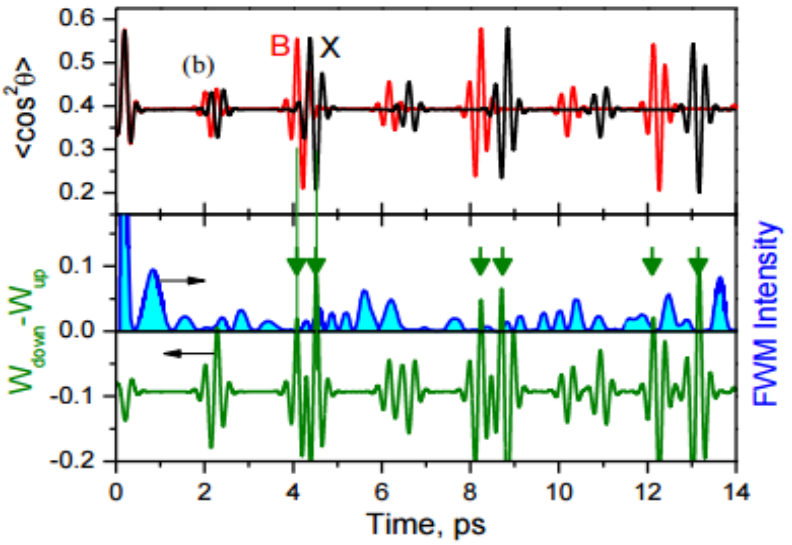

Figure 6.15: Evolution of the rotational alignment factor $\langle\cos^2(\theta(t))\rangle$, calculated probability difference between UV absorption and emission for $P_B = 3/4P_X$, and theoretical UV emission intensity due to four-wave mixing. Courtesy to the ref [71].

6.4.3 Our proposal: Lasing without inversion

Here we propose an explanation for the gain mechanism of 391 nm superradiance, i.e. lasing without inversion (LWI). In the following, the concept of LWI will be first introduced, and then few experimental measurements will be presented and examined to confirm LWI being the gain mechanism of 391 nm superradiance.

It has been know for more than two decades that coherence can enable LWI, which has great potential applications for making lasers in the extreme ultraviolet (EUV) and even x-ray range where population inversion is hard to achieve. LWI has been considered as an interesting quantum mechanical effect and many schemes have been proposed in the literatures [72–82]. In the 1990s, it was proposed that LWI is possible by exploiting the quantum interference between the probability amplitudes of transitions in order to eliminate absorption without disturbing the stimulated emission [83]. For example, in the Λ-scheme shown in Fig. 6.16(a), if $a \rightarrow c$ transition is driven by a laser and the spontaneous decay rate $\gamma_{a\rightarrow c} > \gamma_{a\rightarrow b}$, then coherence between a and b states reaches quasi-steady state and it can yield LWI at the $a \rightarrow b$ transition [75, 84].

Transient LWI has been reported in a resonant V−scheme [85], shown in Fig. 6.16(b). In this scheme, A. Svidzinsky *et al* has demonstrated theoretically a transient amplification of a high-frequency laser field can be achieved by driving a low-frequency transition [84]. They assumed that the strong field ν_d only drives $b \rightarrow c$ transition, while the weak laser field ν_{laser} couples only the $b \rightarrow a$ transition. In such a scheme, one can achieve

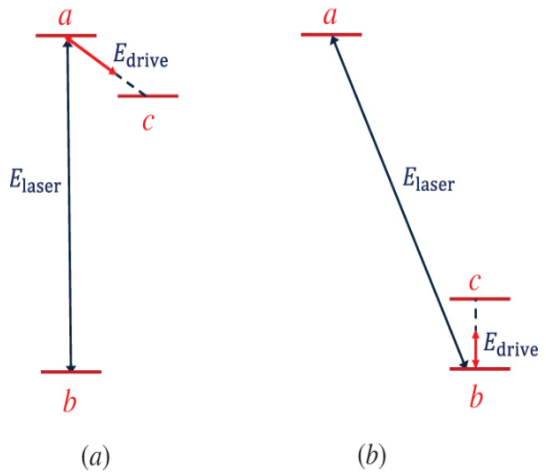

Figure 6.16: Energy level diagram in Λ− and V−schemes. Courtesy to the Ref. [84].

gain at frequencies $\nu_{laser} = \omega_{ac} + m\nu_d$, where $m = \pm 1, \pm 3, ...$ is an odd number, even if there is no population inversion between a and the lower levels b and c. This process can be equivalently interpreted as the transition from the level a to c, which is actually dipole forbidden with emission/absorption of an even number of photons.

We adapt the V−scheme for LWI to our case of 391 nm superradiance of singly ionized nitrogen molecules. The three levels involved corresponds to the upper state $B^2\Sigma_u^+$, the ground state $X^2\Sigma_g^+$ and the lower $A^2\Pi_u$ state of the nitrogen ion. The energy gap between the $A^2\Pi_u$ and $X^2\Sigma_g^+$ state is ∼1.4 eV, which is in near-resonance with the 800 nm (∼ 1.5 eV) pump laser pulse. According to LWI, the coherence between the $A^2\Pi_u$ and $X^2\Sigma_g^+$ states can be driven by the near-resonant 800 nm laser pulse, and it can last much longer time then the duration of 800 nm laser pulse because the collisional decoherence process takes a much longer time, on the order of tens of picoseconds. Therefore, we can expect lasing action between the $B^2\Sigma_u^+$ and $X^2\Sigma_g^+$ state when the $A^2\Pi_u$ and $X^2\Sigma_g^+$ states are strongly coupled by the intense 800 nm laser field with intensity $I \sim 10^{14} - 10^{15}\ W/cm^2$.

6.4.4 Experimental supports of LWI

In the framework of LWI, we are going to reexamine some important experimental results observed by different groups up to now. We will see that this new physics picture can well explain these results.

6.4.4.1 Superradiance nature of 391 nm lasing

We have experimentally confirmed the superradiance nature of 391 nm lasing emission through three different measurements (see Section 6.3). If we compare the temporal profile of the externally-seeded 391 nm superradiance with the simulated result based on LWI model, we find high similarity between them, as shown in Fig. 6.17. In (a), we

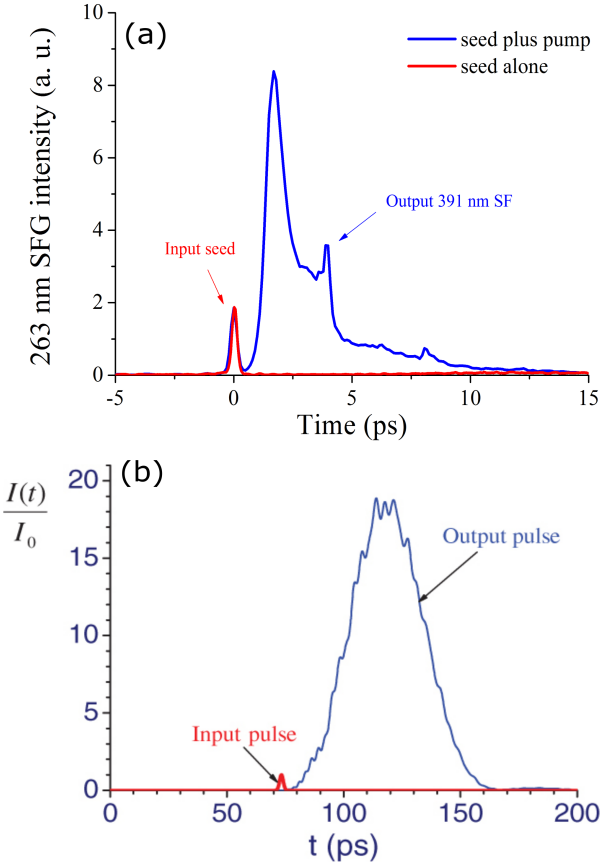

Figure 6.17: (a) Temporal profile of the seeded 391 nm lasing emission after it passes through 3-cm-long filament plasma in 20 mbar nitrogen gas. The red solid line denotes the seed pulse. (b) Simulated temporal profiles of the input and output UV laser pulse after it propagates through 1 cm of He gas driven by an IR coherent field. Courtesy to the Ref. [84].

can see that the input seed pulse triggers a strong wake pulse when it passes through the gain medium prepared by 800 nm femtosecond laser pulse. The simulation result is taken from ref. [84], where it consider the active medium as a gas of helium (He) atoms partially excited in the metastable triplet 2^3S_1 state (level b in the notations) inside He plasma. With a 1083 nm laser pulse to couple the 2^3S_1 and 2^3P_1 (level c in the notations) states, a lasing emission at 388.9 nm wavelength can be generated. This lasing wavelength comes from the $3^3P_1 \rightarrow 2^3S_1$ transition, where 3^3P_1 corresponds to level a in the notations. In (b), the simulated temporal profiles of the input seed laser pulse

and output UV lasing pulse after they pass through the medium are presented. It shows quite similar temporal behavior with our case (see Fig. 6.17(a)), although the temporal scale are different which depends on the experimental parameters.

6.4.4.2 Fast decay of gain dynamics

In the subsection 5.5 in Chapter 5, we have shown the gain dynamics of 391 nm superradiance measured in pump-seed experiment. The lifetime (FWHM) of gain can be few picoseconds, depending on the experiment conditions. It was observed that an increase of the gas pressure leads to significant decrease of the gain lifetime. For this picoseconds decaying process, we have always wondering its origin. In the regime of real population inversion, it should reflect the decay of the inverted population. However, it is somehow counter-intuitive that the population inversion decays in such a short time with few picoseconds. In the new scenario of LWI, this decay lasting for only few picoseconds corresponds to decoherence process of the coupled $X^2\Sigma_g^+$ and $A^2\Pi_u$ states. The decoherence process is mainly due to collisions between the nitrogen ions with electrons, nitrogen ions, neutral nitrogen molecules. Due to the higher velocity of the free electrons compared to neutral or ionic nitrogen molecules, the nitrogen ion-electon collision should dominate this decoherence process. For a simple estimation, in 1 bar air, it is known that the electron-molecule collision time is about 0.3 ps. Thus, for 10 mbar nitrogen gas, the electron-molecule collision time should be close to 30 ps, which is on the same order of magnitude in our experiments. Therefore, we can see that the few-ps time scale of the gain decay of 391 nm superradiance can be well explained in the LWI scenario.

6.4.4.3 Differenece between pumping with 800 nm and mid-IR laser

There is another mystery upon 391 nm lasing effect. It is related to the pump laser wavelength. When 800 nm femtosecond laser is used to be the pump laser, it is now clear that injection of a seeding pulse can lead to significant energy enhancement of 391 nm superradiance (see the subsection 5.4, Chapter 5). This has been confirmed by several groups by using different pulse durations and energies.

However, pumping with mid-IR laser is different. We have performed a collaborative experiments in Peking University (Beijing, China) with 1.35 μm mid-IR femtosecond laser pulses. In the experiment, we focused the laser pulses (165 μ J) with $f = 38$ mm lens into nitrogen gas under pressure of 24.5 mbar and detected the forward emission with spectrometer. The result is shown in Fig. 6.18. A typical Fano asymmetric line shape can be observed. We can see that the injection of external seeding pulse can

not lead to significant energy enhancement. We have tried to vary different experimental parameters to enhance the signal. However, in any case, it can not give rise to a significant enhancement like that pumped by 800 nm laser pulses.

In recent publication [63], the authors in SIOM used 1.75 μm and 1.96 μm mid-IR femtosecond laser pulse to be pump pulse. Only absorption was observed when an external seed pulse centered at 391 nm passed through filament plasma medium. So it is realized that mid-IR pump laser can not lead to substantial optical gain at 391 nm wavelength, although ionic lasing was first reported by pumping with mid-IR laser pulses. So, how should we understand the difference between pumping with 800 nm and mid-IR femtosecond laser pulses ?

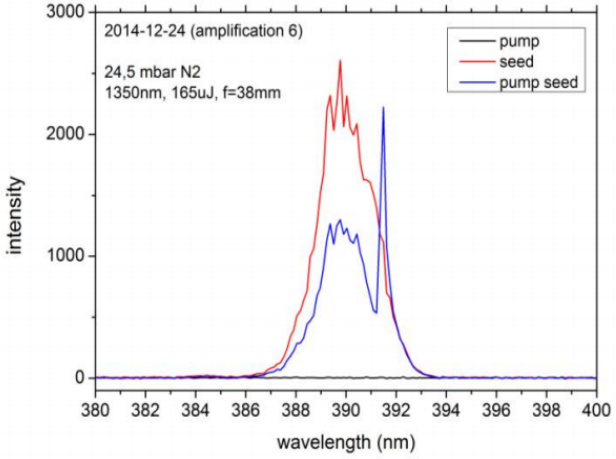

Figure 6.18: Measured spectrum of the seed pulse, spectrum with only 1.35 μm mid-IR pump laser, and that with both the seed and pump pulses. The experimental parameters has been denoted in the figure.

In the framework of LWI, this difference can be naturally explained. In the scenario of LWI, the coupling of the $X^2\Sigma_g^+$ and $A^2\Pi_u$ state through an intense resonant laser field is essential. The optical transition from $X^2\Sigma_g^+$ to $A^2\Pi_u$ state presents several resonant wavelengths at 782 nm, 823 nm, due to the presence of different vibrational levels. Therefore, we found that our femtosecond pulses around 800nm (bandwidth of 40 nm) matches this transition fortuitously. When the mid-IR laser pulse is used, its wavelength is very far from the resonant wavelength of $X^2\Sigma_g^+ \rightarrow A^2\Pi_u$ transition. So the mid-IR laser field can not couple these two states and create coherence between them. As a result, there will be no gain at 391 nm wavelength.

6.4.5 Conclusion

To conclude this section, we have presented three experimental signatures implying that LWI could be the possible gain mechanism of lasing effect of singly ionized nitrogen

molecules. To solidify this proposal, more experimental investigations and numerical simulations are needed, which will be future work on the subject of ionic lasing effect.

6.5 Summary

In summary, we have proposed a new mechanism, namely electron recollision excitation process, for the achievement of population distribution in the upper level of the 391 nm lasing effect in filament plasma. This proposal is supported by two experimental measurements, i.e. pump ellipticity dependence and pump wavelength dependence of 391 nm lasing intensity. Numerical simulation based on the electron recollision excitation model gives rise to good agreement with the experiment observation, solidifying the validity of this electron recollision model.

The 391 nm lasing emission haven been confirmed as superradiance through three independent experiments: 1. pressure dependence of the temporal profile of lasing emission; 2. filament length dependence of the temporal profile of lasing emission; 3. coherent control of 391 nm lasing emission. Particularly, the coherent control measurements directly indicates that there existed a macroscopic polarization in filament plasma, which gives rise to 391 nm superradiance.

Superradiance requires the presence of optical gain, which is normally achieved by population inversion. Here, our experimental observations imply another possibility of gain mechanism, i.e., lasing without inversion. We have discussed three experimental observations, which can be well explained by the LWI model. To further confirm it, more experimental and theoretical efforts are necessary and we are envisaging new experiments in this direction.

General Conclusion

Filamentation of femtosecond laser pulses in nitrogen or air gives rise to a femtosecond filament, during which several nonlinear effects occur and compete each other. One of them is lasing effect, which has been a subject intensively studied in past five years. This thesis devotes to the experimental and theoretical study of two types of lasing effects relating to molecular nitrogen in femtosecond filament.

The first type is lasing effect of neutral nitrogen molecules at 337 nm wavelength, corresponding to vibrational transition from $C^3\Pi_u^+(\upsilon' = 0)$ to $B^3\Pi_g^+(\upsilon = 0)$. It is enabled by using circularly polarized 800 nm laser pulses (40 fs duration, 16 mJ pulse energy) because circular laser field gives rise to more free electrons with high kinetic energy compare to linear laser field. These electrons inelastically collide with neutral nitrogen molecules, excite them from the ground state to the upper $C^3\Pi_u^+(\upsilon' = 0)$ state and build up population inversion, which is the same inversion mechanism with traditional discharge-pumped nitrogen laser.

This lasing effect of neutral nitrogen molecules occurs in both forward and backward directions, and the traveling excitation along with pump laser pulse induces much stronger lasing emission in forward direction than in backward direction. In the presence of optical gain in femtosecond filaments, an injected external seed pulse can be significantly amplified. In both directions, systematical characterizations of lasing pulse have been performed in spatial temporal and spectral domains in this thesis. Specifically, the temporal profile of 337 nm lasing pulse composes of periodic structures due to quantum beats between different branches of above transition. Based on one-dimensional non-adiabatic Maxwell-Bloch equation, numerical simulations on temporal dynamics of lasing effect was performed and the results are in good agreement with the experimental results.

The backward lasing is particularly interesting because it could provide potential applications in atmospheric remote sensing. In ambient air, the lasing effect is significantly prohibited by O_2 molecules through quenching effect. Experiment result shows that backward 337 nm lasing is eliminated when the concentration ratio of oxygen is

larger than 12%. In order to achieve backward lasing from atmospheric air, more effort is needed in future study to find a way of diminishing the influence of O_2 molecules.

The second part of this thesis is devoted to study the lasing effects at 391 nm and 428 nm wavelengths of singly ionized nitrogen molecules in femtosecond filaments in nitrogen gas or ambient air. These two emissions correspond to the transition $B^2\Sigma_u^+(\nu = 0) \rightarrow X^2\Sigma_g^+(\nu' = 0, 1)$ of the first negative band of N_2^+ ion. The 391 nm lasing pulse is normally generated at very low gas pressure under our experimental conditions while the 428 nm lasing pulse is generated at rather high gas pressure. More emphasize was put on 391 nm lasing because these two lasing pulses have similar properties. Different from neutral nitrogen lasing, this ionic lasing effect was only observed in forward direction, despite that a weak backward-propagating seeding pulse can be slightly amplified. Systematical characterizations of 391 nm lasing pulse have been performed in spatial temporal and spectral domains. The temporal profiles of 391 nm lasing pulse suggest that it is fundamentally superradiance, indicating that there exists macroscopic polarization of the aforementioned transition in gain medium.

One important feature of 391 nm lasing effect is that the gain dynamics has an ultrafast gain buildup time less than 300 fs, which is independent of the seed intensity, the gas pressure and the pump pulse energy. As another important feature, this lasing effect sensitively depends on the ellipticity of pump laser pulse, and shows high similarities with HHG of N_2 molecules. Based on these two points, a new mechanism namely the electron recollision excitation process, was proposed to interpret the achievement of population distribution in the upper level of transition. Numerical simulations based on semi-classical electron recollision model suggest that 391 nm lasing effect should periodically varies with the pump laser wavelength, and disappears when the pump laser wavelength is twice 391 nm. It has been confirmed experimentally, strongly supporting that the electron recollision excitation mechanism is at the heart of the lasing effect of N_2^+.

Superradiance requires the presence of optical gain, which is normally achieved by population inversion. However, the expected population level of excitation due to electron recollision process is relatively low, of the order of 1%, which is insufficient for the population inversion. A possible explanation is 391 nm lasing, without inversion enabled by the quantum interference between $X^2\Sigma_g^+ \rightarrow B^2\Sigma_u^+$ transition and $X^2\Sigma_g^+ \rightarrow A^2\Pi_u$ transition, which is closely-resonantly excited by 800 nm pump laser pulse. To further prove it, there needs more evidences and efforts in both experiment and theory.

Appendix A

Laser Systems

A.1 Alpha-100 laser system

The commercial Alpha-100 Ti:sapphire laser system was developed by Thales company. It was installed in Salle Blanche in Laboratory of Applied Optics (Laboratoire d'Optique Appliquée) in 2006, as shown in Fig. A.1. This laser system can provide Gaussian laser pulses at central wavelength of 800 nm, with FWHM duration of 40 fs and pulse energy of 15 mJ, operating at repetition rate of 100 Hz. The transverse size of laser beam is about 7 mm (FWHM). The pulse energy output of laser system has a good stability.

Figure A.1: Photograph of Salle Blanche and Alpha-100 laser system.

A.2 ENSTAmobile laser system

The ENSTAmobile laser system is entirely installed inside a $\sim 3\ m^3$ wheeled container in Salle Blue, making it movable for field experiments. This laser system consists of a Chirped Pulse Amplification (CPA) laser chain from Amplitude Technology. A femtosecond source oscillator (Femtolasers GmbH) provides femtosecond laser pulses, which is then amplified in two successive stages:

I. the laser pulse passes through a regenerative amplifier coupled to a multipass amplifier, which is pumped by a 130 mJ frequency-doubled Nd:YAG laser (CFR200 from Quantel Laser);

II. then the laser pulses are sent to a second multipass amplifier pumped by a 2 J frequency-doubled Nd:YAG laser (PRO6PULSE+ from Amplitude Technologies).

The output laser pulse can reach up to 200 mJ for a duration of 50 fs, operating at repetition rate of 10 Hz. The laser beam has a super-Gaussian profile with a FWHM diameter 35 mm. A photograph of the laser system and Salle Blue is shown in Fig. A.2.

Figure A.2: Photograph of Salle Blue and ENSTAmobile laser system.

Appendix B

Publications

B.1 Publications in peer-reviewed journals

[1] Pengji Ding, Eduardo Oliva, Aurélien Houard, André Mysyrowicz, and Yi Liu, "Lasing dynamics of neutral nitrogen molecules in femtosecond filaments," Phys. Rev. A. **94**(4), 043824 (2016).

[2] Yi Liu, Pengji Ding, Guillaume Lambert, Aurelien Houard, Vladimir Tikhonchuk, and André Mysyrowicz, "Recollision-Induced Superradiance of Ionized Nitrogen Molecules", Phys. Rev. Lett. **115**(13), 133203 (2015).

[3] Sergey Mitryukovskiy, Yi Liu, Pengji Ding, Aurélien Houard, Arnaud Couairon, and André Mysyrowicz, "Plasma Luminescence from Femtosecond Filaments in Air: Evidence for Impact Excitation with Circularly Polarized Light Pulses", Phys. Rev. Lett. **114**(6), 063003 (2015).

[4] Pengji Ding, Sergey Mitryukovskiy, Aurélien Houard, Eduardo Oliva, Arnaud Couairon, André Mysyrowicz, and Yi Liu, "Backward Lasing of Air plasma pumped by Circularly polarized femtosecond pulses for the saKe of remote sensing (BLACK)", Optics Express **22**(24), 029964 (2014).

[5] Sergey Mitryukovskiy, Yi Liu, Pengji Ding, Aurélien Houard, and André Mysyrowicz, "Backward stimulated radiation from filaments in nitrogen gas and air pumped by circularly polarized 800 nm femtosecond laser pulses", Optics Express **22**(11), 012750 (2014).

[6] Guillaume Point, Yi Liu, Yohann Brelet, Sergey Mitryukovskiy, Pengji Ding, Aurélien Houard, and André Mysyrowicz, "Lasing of ambient air with microjoule pulse energy pumped by a multi terawatt IR femtosecond laser", Optics Letters **39**(7), 1725 (2014).

B.2 Book Chapter

[1] Yi Liu, Sergey Mitryukovskiy, Pengji Ding, Guillaume Point, Yohann Brelet, Aurélien Houard, Arnaud Couairon, and André Mysyrowicz, "Backward Lasing of Femtosecond Plasma Filaments", pages 89-103. Springer International Publishing, Cham, 2016. ISBN 978-3-319-23657-5. URL http://dx.doi.org/10.1007/978-3-319-23657-5-5.

B.3 Attended international conferences

[1] PengJi Ding, Eduardo Oliva, Yi Liu, Aurélien Houard, and André Mysyrowicz, "Lasing dynamics of neutral nitrogen molecules in filament," accepted as poster, in 2016, the 6th International Symposium on Filamentation (COFIL2016).

[2] Y. Liu, P. Ding, G. Lambert, A. Houard, V. Tikhonchuk, and A. Mysyrowicz, "Superradiance of Air Plasma Induced by Electron Recollision," in Conference on Lasers and Electro-Optics, OSA Technical Digest (online) (Optical Society of America, 2016), paper FTh3M.7.

[3] P. Ding, S. Mitryukovskiy, A. Houard, E. Oliva, A. Couairon, A. Mysyrowicz, and Y. Liu, "Backward 337 nm nitrogen lasing from filament plasma induced by circularly polarized laser pulse," in 2015 European Conference on Lasers and Electro-Optics - European Quantum Electronics Conference, (Optical Society of America, 2015), paper EE-2-3.

[4] Y. Liu, S. Mitryukovskiy, P. Ding, A. Houard, and A. Mysyrowicz, "Lasing from Plasma Filaments in Air," in CLEO: 2015, OSA Technical Digest (online) (Optical Society of America, 2015), paper SM2N.2.

[5] PengJi Ding, Yi Liu, Guillaume Point, Yohann Brelet, Sergey Mitryukovsiky, Aurélien Houard, and André Mysyrowicz, "Microjoule air lasing pumped by a 4 TW femtosecond laser at 800 nm," poster, in 2014, the 5th International Symposium on Filamentation (COFIL2014).

Bibliography

[1] A. Couairon and A. Mysyrowicz. Femtosecond filamentation in transparent media. *Physics Reports*, 441(2–4):47 – 189, 2007. ISSN 0370-1573. doi: http://dx.doi.org/10.1016/j.physrep.2006.12.005. URL http://www.sciencedirect.com/science/article/pii/S037015730700021X.

[2] S. L. Chin, T. J. Wang, C. Marceau, J. Wu, J. S. Liu, O. Kosareva, N. Panov, Y. P. Chen, J. F. Daigle, S. Yuan, A. Azarm, W. W. Liu, T. Seideman, H. P. Zeng, M. Richardson, R. Li, and Z. Z. Xu. Advances in intense femtosecond laser filamentation in air. *Laser Physics*, 22(1):1–53, 2012. ISSN 1555-6611. doi: 10.1134/S1054660X11190054. URL http://dx.doi.org/10.1134/S1054660X11190054.

[3] A. Braun, G. Korn, X. Liu, D. Du, J. Squier, and G. Mourou. Self-channeling of high-peak-power femtosecond laser pulses in air. *Opt. Lett.*, 20(1):73–75, Jan 1995. doi: 10.1364/OL.20.000073. URL http://ol.osa.org/abstract.cfm?URI=ol-20-1-73.

[4] E. T. J. Nibbering, P. F. Curley, G. Grillon, B. S. Prade, M. A. Franco, F. Salin, and A. Mysyrowicz. Conical emission from self-guided femtosecond pulses in air. *Opt. Lett.*, 21(1):62–64, Jan 1996. doi: 10.1364/OL.21.000062. URL http://ol.osa.org/abstract.cfm?URI=ol-21-1-62.

[5] Z. Jiang C. Y. Chien D. Comtois A. Desparois T. W. Johnston J.-C. Kieffer H. Pepin B. La Fontaine, F. Vidal and H. P. Mercure. Filamentation of ultrashort pulse laser beams resulting from their propagation over long distances in air. *Phys. Plasmas*, 6:1615, Jan 1999. doi: 10.1063/1.873715. URL http://scitation.aip.org/content/aip/journal/pop/6/5/10.1063/1.873715.

[6] G. Méchain, A. Couairon, Y.-B. André, C. D'Amico, M. Franco, B. Prade, S. Tzortzakis, A. Mysyrowicz, and R. Sauerbrey. Long-range self-channeling of infrared laser pulses in air: a new propagation regime without ionization. *Applied Physics B*, 79(3):379–382, 2004. ISSN 1432-0649. doi: 10.1007/s00340-004-1557-8. URL http://dx.doi.org/10.1007/s00340-004-1557-8.

[7] Miguel Rodriguez, Riad Bourayou, Guillaume Méjean, Jérôme Kasparian, Jin Yu, Estelle Salmon, Alexander Scholz, Bringfried Stecklum, Jochen Eislöffel, Uwe Laux, Artie P. Hatzes, Roland Sauerbrey, Ludger Wöste, and Jean-Pierre Wolf. Kilometer-range nonlinear propagation of femtosecond laser pulses. *Phys. Rev. E*, 69:036607, Mar 2004. doi: 10.1103/PhysRevE.69.036607. URL http://link.aps.org/doi/10.1103/PhysRevE.69.036607.

[8] Gadi Fibich and Alexander L. Gaeta. Critical power for self-focusing in bulk media and in hollow waveguides. *Opt. Lett.*, 25(5):335–337, Mar 2000. doi: 10.1364/OL.25.000335. URL http://ol.osa.org/abstract.cfm?URI=ol-25-5-335.

[9] E. L. DAWES and J. H. MARBURGER. Computer studies in self-focusing. *Phys. Rev.*, 179:862–868, Mar 1969. doi: 10.1103/PhysRev.179.862. URL http://link.aps.org/doi/10.1103/PhysRev.179.862.

[10] J.H. Marburger. Self-focusing: Theory. *Progress in Quantum Electronics*, 4:35 – 110, 1975. ISSN 0079-6727. doi: http://dx.doi.org/10.1016/0079-6727(75)90003-8. URL http://www.sciencedirect.com/science/article/pii/0079672775900038.

[11] Joshua E. Rothenberg. Space–time focusing: breakdown of the slowly varying envelope approximation in the self-focusing of femtosecond pulses. *Opt. Lett.*, 17 (19):1340–1342, Oct 1992. doi: 10.1364/OL.17.001340. URL http://ol.osa.org/abstract.cfm?URI=ol-17-19-1340.

[12] G. Fibich and G. C. Papanicolaou. Self-focusing in the presence of small time dispersion and nonparaxiality. *Opt. Lett.*, 22(18):1379–1381, Sep 1997. doi: 10.1364/OL.22.001379. URL http://ol.osa.org/abstract.cfm?URI=ol-22-18-1379.

[13] J. Kasparian, R. Sauerbrey, D. Mondelain, S. Niedermeier, J. Yu, J.-P. Wolf, Y.-B. André, M. Franco, B. Prade, S. Tzortzakis, A. Mysyrowicz, M. Rodriguez, H. Wille, and L. Wöste. Infrared extension of the supercontinuum generated by femtosecond terawatt laser pulses propagating in the atmosphere. *Opt. Lett.*, 25(18):1397–1399, Sep 2000. doi: 10.1364/OL.25.001397. URL http://ol.osa.org/abstract.cfm?URI=ol-25-18-1397.

[14] Jean-Francois Ripoche, Georges Grillon, Bernard Prade, Michel Franco, Erik Nibbering, Rüdiger Lange, and André Mysyrowicz. Determination of the time dependence of n2 in air. *Optics Communications*, 135(4):310 – 314, 1997. ISSN 0030-4018. doi: http://dx.doi.org/10.1016/S0030-4018(96)00675-X. URL http://www.sciencedirect.com/science/article/pii/S003040189600675X.

[15] Q. Luo, W. Liu, and S.L. Chin. Lasing action in air induced by ultra-fast laser filamentation. *Applied Physics B*, 76(3):337–340, 2003. ISSN 0946-2171. doi: 10.1007/s00340-003-1115-9. URL http://dx.doi.org/10.1007/s00340-003-1115-9.

[16] Daniil Kartashov, Skirmantas Ališauskas, Giedrius Andriukaitis, Audrius Pugžlys, Mikhail Shneider, Aleksei Zheltikov, See Leang Chin, and Andrius Baltuška. Free-space nitrogen gas laser driven by a femtosecond filament. *Phys. Rev. A*, 86:033831, Sep 2012. doi: 10.1103/PhysRevA.86.033831. URL http://link.aps.org/doi/10.1103/PhysRevA.86.033831.

[17] Pengji Ding, Sergey Mitryukovskiy, Aurélien Houard, Eduardo Oliva, Arnaud Couairon, André Mysyrowicz, and Yi Liu. Backward lasing of air plasma pumped by circularly polarized femtosecond pulses for the sake of remote sensing (black). *Opt. Express*, 22(24):29964–29977, Dec 2014. doi: 10.1364/OE.22.029964. URL http://www.opticsexpress.org/abstract.cfm?URI=oe-22-24-29964.

[18] Sergey Mitryukovskiy, Yi Liu, Pengji Ding, Aurélien Houard, and André Mysyrowicz. Backward stimulated radiation from filaments in nitrogen gas and air pumped by circularly polarized 800 nm femtosecond laser pulses. *Opt. Express*, 22(11):12750–12759, Jun 2014. doi: 10.1364/OE.22.012750. URL http://www.opticsexpress.org/abstract.cfm?URI=oe-22-11-12750.

[19] Yi Liu, Sergey Mitryukovskiy, Pengji Ding, Guillaume Point, Yohann Brelet, Aurélien Houard, Arnaud Couairon, and André Mysyrowicz. *Backward Lasing of Femtosecond Plasma Filaments*, pages 89–103. Springer International Publishing, Cham, 2015. ISBN 978-3-319-23657-5. doi: 10.1007/978-3-319-23657-5_5. URL http://dx.doi.org/10.1007/978-3-319-23657-5_5.

[20] Jinping Yao, Bin Zeng, Huailiang Xu, Guihua Li, Wei Chu, Jielei Ni, Haisu Zhang, See Leang Chin, Ya Cheng, and Zhizhan Xu. High-brightness switchable multiwavelength remote laser in air. *Phys. Rev. A*, 84:051802, Nov 2011. doi: 10.1103/PhysRevA.84.051802. URL http://link.aps.org/doi/10.1103/PhysRevA.84.051802.

[21] Andriukaitis, G., Möhring, J., Kartashov, D., Pugžlys, A., Zheltikov, A., Motzkus, M., and Baltuška, A. Intense, directional uv emission from molecular nitrogen ions in an adaptively controlled femtosecond filament. *EPJ Web of Conferences*, 41:10004, 2013. doi: 10.1051/epjconf/20134110004. URL http://dx.doi.org/10.1051/epjconf/20134110004.

[22] Jinping Yao, Guihua Li, Chenrui Jing, Bin Zeng, Wei Chu, Jielei Ni, Haisu Zhang, Hongqiang Xie, Chaojin Zhang, Helong Li, Huailiang Xu, See Leang Chin,

Ya Cheng, and Zhizhan Xu. Remote creation of coherent emissions in air with two-color ultrafast laser pulses. *New Journal of Physics*, 15(2):023046, 2013. URL http://stacks.iop.org/1367-2630/15/i=2/a=023046.

[23] Jielei Ni, Wei Chu, Chenrui Jing, Haisu Zhang, Bin Zeng, Jinping Yao, Guihua Li, Hongqiang Xie, Chaojin Zhang, Huailiang Xu, See-Leang Chin, Ya Cheng, and Zhizhan Xu. Identification of the physical mechanism of generation of coherent n2+ emissions in air by femtosecond laser excitation. *Opt. Express*, 21(7):8746–8752, Apr 2013. doi: 10.1364/OE.21.008746. URL http://www.opticsexpress.org/abstract.cfm?URI=oe-21-7-8746.

[24] Yi Liu, Yohann Brelet, Guillaume Point, Aurélien Houard, and André Mysyrowicz. Self-seeded lasing in ionized air pumped by 800 nm femtosecond laser pulses. *Opt. Express*, 21(19):22791–22798, Sep 2013. doi: 10.1364/OE.21.022791. URL http://www.opticsexpress.org/abstract.cfm?URI=oe-21-19-22791.

[25] Wei Chu, Guihua Li, Hongqiang Xie, Jielei Ni, Jinping Yao, Bin Zeng, Haisu Zhang, Chenrui Jing, Huailiang Xu, Ya Cheng, and Zhizhan Xu. A self-induced white light seeding laser in a femtosecond laser filament. *Laser Physics Letters*, 11(1):015301, 2014. URL http://stacks.iop.org/1612-202X/11/i=1/a=015301.

[26] Tie-Jun Wang, Jean-Fran çois Daigle, Jingjing Ju, Shuai Yuan, Ruxin Li, and See Leang Chin. Forward lasing action at multiple wavelengths seeded by white light from a femtosecond laser filament in air. *Phys. Rev. A*, 88:053429, Nov 2013. doi: 10.1103/PhysRevA.88.053429. URL http://link.aps.org/doi/10.1103/PhysRevA.88.053429.

[27] Guillaume Point, Yi Liu, Yohann Brelet, Sergey Mitryukovskiy, Pengji Ding, Aurélien Houard, and André Mysyrowicz. Lasing of ambient air with microjoule pulse energy pumped by a multi-terawatt infrared femtosecond laser. *Opt. Lett.*, 39(7):1725–1728, Apr 2014. doi: 10.1364/OL.39.001725. URL http://ol.osa.org/abstract.cfm?URI=ol-39-7-1725.

[28] Yi Liu, Pengji Ding, Guillaume Lambert, Aurélien Houard, Vladimir Tikhonchuk, and André Mysyrowicz. Recollision-induced superradiance of ionized nitrogen molecules. *Phys. Rev. Lett.*, 115:133203, Sep 2015. doi: 10.1103/PhysRevLett.115.133203. URL http://link.aps.org/doi/10.1103/PhysRevLett.115.133203.

[29] Arthur Dogariu, James B. Michael, Marlan O. Scully, and Richard B. Miles. High-gain backward lasing in air. *Science*, 331(6016):442–445, 2011. doi: 10.1126/science.1199492. URL http://www.sciencemag.org/content/331/6016/442.abstract.

[30] R.S. Kunabenchi, M.R. Gorbal, and M.I. Savadatti. Nitrogen lasers. *Progress in Quantum Electronics*, 9(4):259 – 329, 1984. ISSN 0079-6727. doi: http://dx.doi.org/10.1016/0079-6727(84)90027-2. URL http://www.sciencedirect.com/science/article/pii/0079672784900272.

[31] W. Kim M. S. Bak1 and M. A. Cappelli. On the quenching of excited electronic states of molecular nitrogen in nanosecond pulsed discharges in atmospheric pressure air. *Appl. Phys. Lett.*, 98:011502, Jan 2011. doi: 10.1063/1.3535986. URL http://scitation.aip.org/content/aip/journal/apl/98/1/10.1063/1.3535986.

[32] I. R. Al'miev, O. Larroche, D. Benredjem, J. Dubau, S. Kazamias, C. Möller, and A. Klisnick. Dynamical description of transient x-ray lasers seeded with high-order harmonic radiation through maxwell-bloch numerical simulations. *Phys. Rev. Lett.*, 99:123902, Sep 2007. doi: 10.1103/PhysRevLett.99.123902. URL http://link.aps.org/doi/10.1103/PhysRevLett.99.123902.

[33] Eduardo Oliva, Philippe Zeitoun, Marta Fajardo, Guillaume Lambert, David Ros, Stephane Sebban, and Pedro Velarde. Comparison of natural and forced amplification regimes in plasma-based soft-x-ray lasers seeded by high-order harmonics. *Phys. Rev. A*, 84:013811, Jul 2011. doi: 10.1103/PhysRevA.84.013811. URL http://link.aps.org/doi/10.1103/PhysRevA.84.013811.

[34] H M von Bergmann and V Hasson. Gain, fluorescence and energy extraction characteristics of photostabilised atmospheric pressure uv nitrogen lasers. *Journal of Physics D: Applied Physics*, 11(17):2341, 1978. URL http://stacks.iop.org/0022-3727/11/i=17/a=005.

[35] Tian-Liang Zhao, Yong Xu, Yuan-Hong Song, Xiao-Song Li, Jing-Lin Liu, Jin-Bao Liu, and Ai-Min Zhu. Determination of vibrational and rotational temperatures in a gliding arc discharge by using overlapped molecular emission spectra. *Journal of Physics D: Applied Physics*, 46(34):345201, 2013. URL http://stacks.iop.org/0022-3727/46/i=34/a=345201.

[36] H.L. Xu, A. Azarm, J. Bernhardt, Y. Kamali, and S.L. Chin. The mechanism of nitrogen fluorescence inside a femtosecond laser filament in air. *Chemical Physics*, 360(1–3):171 – 175, 2009. ISSN 0301-0104. doi: http://dx.doi.org/10.1016/j.chemphys.2009.05.001. URL http://www.sciencedirect.com/science/article/pii/S0301010409001487.

[37] M. Kolesik, J. V. Moloney, and E. M. Wright. Polarization dynamics of femtosecond pulses propagating in air. *Phys. Rev. E*, 64:046607, Sep 2001. doi: 10.1103/PhysRevE.64.046607. URL http://link.aps.org/doi/10.1103/PhysRevE.64.046607.

[38] P. H. Bucksbaum, M. Bashkansky, R. R. Freeman, T. J. McIlrath, and L. F. DiMauro. Suppression of multiphoton ionization with circularly polarized coherent light. *Phys. Rev. Lett.*, 56:2590–2593, Jun 1986. doi: 10.1103/PhysRevLett.56.2590. URL http://link.aps.org/doi/10.1103/PhysRevLett.56.2590.

[39] P. B. Corkum, N. H. Burnett, and F. Brunel. Above-threshold ionization in the long-wavelength limit. *Phys. Rev. Lett.*, 62:1259–1262, Mar 1989. doi: 10.1103/PhysRevLett.62.1259. URL http://link.aps.org/doi/10.1103/PhysRevLett.62.1259.

[40] Tatsuo Tabata, Toshizo Shirai, Masao Sataka, and Hirotaka Kubo. Analytic cross sections for electron impact collisions with nitrogen molecules. *Atomic Data and Nuclear Data Tables*, 92(3):375 – 406, 2006. ISSN 0092-640X. doi: http://dx.doi.org/10.1016/j.adt.2006.02.002. URL http://www.sciencedirect.com/science/article/pii/S0092640X06000143.

[41] B. Hafizi D. Gordon P. Sprangle, J. Peñano and M. Scully. Remotely induced atmospheric lasing. *Appl. Phys. Lett.*, 98:211102, May 2011. doi: 10.1063/1.3584034. URL http://scitation.aip.org/content/aip/journal/apl/98/21/10.1063/1.3584034.

[42] B. Hafizi D. Gordon R. Fernsler J. Peñano, P. Sprangle and M. Scully. Remote lasing in air by recombination and electron impact excitation of molecular nitrogen. *J. Appl. Phys.*, 111:033105, 2012. doi: 10.1063/1.3681282. URL http://scitation.aip.org/content/aip/journal/jap/111/3/10.1063/1.3681282.

[43] E. Oliva L. Li M. Berrill L. Yin J. Nejdl B. M. Luther C. Proux T. T. T. Le J. Dunn D. Ros Ph. Zeitoun Y. Wang, S. Wang and J. J. Rocca. Gain dynamics in a soft-x-ray laser amplifier perturbed by a strong injected x-ray field. *Nat. Phot.*, 8:381–384, 2014. doi: 10.1038/nphoton.2014.79. URL http://www.nature.com/nphoton/journal/v8/n5/abs/nphoton.2014.79.html.

[44] O. Larroche, D. Ros, A. Klisnick, A. Sureau, C. Möller, and H. Guennou. Maxwell-bloch modeling of x-ray-laser-signal buildup in single- and double-pass configurations. *Phys. Rev. A*, 62:043815, Sep 2000. doi: 10.1103/PhysRevA.62.043815. URL http://link.aps.org/doi/10.1103/PhysRevA.62.043815.

[45] S. Chandrasekhar. Stochastic problems in physics and astronomy. *Rev. Mod. Phys.*, 15:1–89, Jan 1943. doi: 10.1103/RevModPhys.15.1. URL http://link.aps.org/doi/10.1103/RevModPhys.15.1.

[46] Daniil Kartashov, Skirmantas Ališauskas, Audrius Pugžlys, Mikhail N Shneider, and Andrius Baltuška. Theory of a filament initiated nitrogen laser. *Journal of*

Physics B: Atomic, Molecular and Optical Physics, 48(9):16, 2015. URL http://stacks.iop.org/0953-4075/48/i=9/a=094016.

[47] Sergey Mitryukovskiy, Yi Liu, Pengji Ding, Aurélien Houard, Arnaud Couairon, and André Mysyrowicz. Plasma luminescence from femtosecond filaments in air: Evidence for impact excitation with circularly polarized light pulses. *Phys. Rev. Lett.*, 114:063003, Feb 2015. doi: 10.1103/PhysRevLett.114.063003. URL http://link.aps.org/doi/10.1103/PhysRevLett.114.063003.

[48] H M von Bergmann and V Hasson. Gain, fluorescence and energy extraction characteristics of photostabilised atmospheric pressure uv nitrogen lasers. *Journal of Physics D: Applied Physics*, 11(17):2341, 1978. URL http://stacks.iop.org/0022-3727/11/i=17/a=005.

[49] Strohwald H and Salzmann H. Picosecond uv laser pulses from gas discharges in pure nitrogen at pressures up to 6 atm. *Appl. Phys. Lett.*, 28:272, 1976. doi: 10.1063/1.88732. URL http://scitation.aip.org/content/aip/journal/apl/28/5/10.1063/1.88732.

[50] Bin Zeng, Wei Chu, Guihua Li, Jinping Yao, Haisu Zhang, Jielei Ni, Chenrui Jing, Hongqiang Xie, and Ya Cheng. Real-time observation of dynamics in rotational molecular wave packets by use of air-laser spectroscopy. *Phys. Rev. A*, 89:042508, Apr 2014. doi: 10.1103/PhysRevA.89.042508. URL http://link.aps.org/doi/10.1103/PhysRevA.89.042508.

[51] M. Gross and S. Haroche. Superradiance: An essay on the theory of collective spontaneous emission. *Physics Reports*, 93(5):301 – 396, 1982. ISSN 0370-1573. doi: http://dx.doi.org/10.1016/0370-1573(82)90102-8. URL http://www.sciencedirect.com/science/article/pii/0370157382901028.

[52] Sergey Mitryukovskiy, Yi Liu, Aurélien Houard, and André Mysyrowicz. Re-evaluation of the peak intensity inside a femtosecond laser filament in air. *Journal of Physics B: Atomic, Molecular and Optical Physics*, 48(9):094003, 2015. URL http://stacks.iop.org/0953-4075/48/i=9/a=094003.

[53] P. B. Corkum. Plasma perspective on strong field multiphoton ionization. *Phys. Rev. Lett.*, 71:1994–1997, Sep 1993. doi: 10.1103/PhysRevLett.71.1994. URL http://link.aps.org/doi/10.1103/PhysRevLett.71.1994.

[54] N. H. Burnett, C. Kan, and P. B. Corkum. Ellipticity and polarization effects in harmonic generation in ionizing neon. *Phys. Rev. A*, 51:R3418–R3421, May 1995. doi: 10.1103/PhysRevA.51.R3418. URL http://link.aps.org/doi/10.1103/PhysRevA.51.R3418.

[55] Misha Yu. Ivanov, Thomas Brabec, and Neal Burnett. Coulomb corrections and polarization effects in high-intensity high-harmonic emission. *Phys. Rev. A*, 54:742–745, Jul 1996. doi: 10.1103/PhysRevA.54.742. URL http://link.aps.org/doi/10.1103/PhysRevA.54.742.

[56] M. Kakehata, H. Takada, H. Yumoto, and K. Miyazaki. Anomalous ellipticity dependence of high-order harmonic generation. *Phys. Rev. A*, 55:R861–R864, Feb 1997. doi: 10.1103/PhysRevA.55.R861. URL http://link.aps.org/doi/10.1103/PhysRevA.55.R861.

[57] H. Soifer, P. Botheron, D. Shafir, A. Diner, O. Raz, B. D. Bruner, Y. Mairesse, B. Pons, and N. Dudovich. Near-threshold high-order harmonic spectroscopy with aligned molecules. *Phys. Rev. Lett.*, 105:143904, Sep 2010. doi: 10.1103/PhysRevLett.105.143904. URL http://link.aps.org/doi/10.1103/PhysRevLett.105.143904.

[58] Hua Yang, Peng Liu, Ruxin Li, and Zhizhan Xu. Ellipticity dependence of the near-threshold harmonics of h2 in an elliptical strong laser field. *Opt. Express*, 21(23):28676–28684, Nov 2013. doi: 10.1364/OE.21.028676. URL http://www.opticsexpress.org/abstract.cfm?URI=oe-21-23-28676.

[59] Chu Wei Xie Hongqiang Yao Jinping Li Guihua Qiao Lingling Wang Zhanshan Li Ziting, Zeng Bin and Cheng Ya.

[60] See Leang Chin, Huailiang Xu, Ya Cheng, Zhizhan Xu, and Kaoru Yamanouchi. Natural population inversion in a gaseous molecular filament. *Chin. Opt. Lett.*, 11(1):013201, Jan 2013. URL http://col.osa.org/abstract.cfm?URI=col-11-1-013201.

[61] Daniil Kartashov, Jens Möhring, Giedrius Andriukaitis, Audrius Pugzlys, Aleksei Zheltikov, Markus Motzkus, and Andrius Baltuska. Stimulated amplification of uv emission in a femtosecond filament using adaptive control. In *Conference on Lasers and Electro-Optics 2012*, page QTh4E.6. Optical Society of America, 2012. doi: 10.1364/QELS.2012.QTh4E.6. URL http://www.osapublishing.org/abstract.cfm?URI=QELS-2012-QTh4E.6.

[62] Xu Huailiang, Lotstedt Erik, Iwasaki Atsushi, and Kaoru Yamanouchi. Sub-10-fs population inversion in n2+ in air lasing through multiple state coupling. *Nat Commun*, 6. doi: 10.1038/ncomms9347. URL http://dx.doi.org/10.1038/ncomms9347.

[63] Jinping Yao, Shicheng Jiang, Wei Chu, Bin Zeng, Chengyin Wu, Ruifeng Lu, Ziting Li, Hongqiang Xie, Guihua Li, Chao Yu, Zhanshan Wang, Hongbing Jiang, Qihuang

Gong, and Ya Cheng. Population redistribution among multiple electronic states of molecular nitrogen ions in strong laser fields. *Phys. Rev. Lett.*, 116:143007, Apr 2016. doi: 10.1103/PhysRevLett.116.143007. URL http://link.aps.org/doi/10.1103/PhysRevLett.116.143007.

[64] X. M. Tong, Z. X. Zhao, and C. D. Lin. Theory of molecular tunneling ionization. *Phys. Rev. A*, 66:033402, Sep 2002. doi: 10.1103/PhysRevA.66.033402. URL http://link.aps.org/doi/10.1103/PhysRevA.66.033402.

[65] E. P. Benis, J. F. Xia, X. M. Tong, M. Faheem, M. Zamkov, B. Shan, P. Richard, and Z. Chang. Ionization suppression of cl_2 molecules in intense laser fields. *Phys. Rev. A*, 70:025401, Aug 2004. doi: 10.1103/PhysRevA.70.025401. URL http://link.aps.org/doi/10.1103/PhysRevA.70.025401.

[66] R. H. Dicke. Coherence in spontaneous radiation processes. *Phys. Rev.*, 93:99–110, Jan 1954. doi: 10.1103/PhysRev.93.99. URL http://link.aps.org/doi/10.1103/PhysRev.93.99.

[67] J. C. MacGillivray and M. S. Feld. Theory of superradiance in an extended, optically thick medium. *Phys. Rev. A*, 14:1169–1189, Sep 1976. doi: 10.1103/PhysRevA.14.1169. URL http://link.aps.org/doi/10.1103/PhysRevA.14.1169.

[68] Guihua Li, Chenrui Jing, Bin Zeng, Hongqiang Xie, Jinping Yao, Wei Chu, Jielei Ni, Haisu Zhang, Huailiang Xu, Ya Cheng, and Zhizhan Xu. Signature of superradiance from a nitrogen-gas plasma channel produced by strong-field ionization. *Phys. Rev. A*, 89:033833, Mar 2014. doi: 10.1103/PhysRevA.89.033833. URL http://link.aps.org/doi/10.1103/PhysRevA.89.033833.

[69] Marlan O. Scully and Anatoly A. Svidzinsky. The super of superradiance. *Science*, 325(5947):1510–1511, 2009. ISSN 0036-8075. doi: 10.1126/science.1176695. URL http://science.sciencemag.org/content/325/5947/1510.

[70] Roland Ackermann, Ioannis Makos, Marita Kerstan, Robert Kammel, Stefan Nolte, and Andreas Tünnermann. Analysis of laser induced plasma in air using broadband femtosecond coherent anti-stokes raman scattering. In *Conference on Lasers and Electro-Optics*, page SF1O.4. Optical Society of America, 2016. doi: 10.1364/CLEO_SI.2016.SF1O.4. URL http://www.osapublishing.org/abstract.cfm?URI=CLEO_SI-2016-SF1O.4.

[71] Andrius Baltuska and Daniil Kartashov. Transient inversion in rotationally aligned nitrogen ions in a femtosecond filament. In *Research in Optical Sciences*, page HTh4B.5. Optical Society of America, 2014. doi: 10.1364/HILAS.2014.HTh4B.5. URL http://www.osapublishing.org/abstract.cfm?URI=HILAS-2014-HTh4B.5.

[72] S. E. Harris. Lasers without inversion: Interference of lifetime-broadened resonances. *Phys. Rev. Lett.*, 62:1033–1036, Feb 1989. doi: 10.1103/PhysRevLett.62.1033. URL http://link.aps.org/doi/10.1103/PhysRevLett.62.1033.

[73] A. Imamo˘lu. Interference of radiatively broadened resonances. *Phys. Rev. A*, 40: 2835–2838, Sep 1989. doi: 10.1103/PhysRevA.40.2835. URL http://link.aps.org/doi/10.1103/PhysRevA.40.2835.

[74] S. E. Harris and J. J. Macklin. Lasers without inversion: Single-atom transient response. *Phys. Rev. A*, 40:4135–4137, Oct 1989. doi: 10.1103/PhysRevA.40.4135. URL http://link.aps.org/doi/10.1103/PhysRevA.40.4135.

[75] A. Imamolu, J. E. Field, and S. E. Harris. Lasers without inversion: A closed lifetime broadened system. *Phys. Rev. Lett.*, 66:1154–1156, Mar 1991. doi: 10.1103/PhysRevLett.66.1154. URL http://link.aps.org/doi/10.1103/PhysRevLett.66.1154.

[76] Marlan O. Scully, Shi-Yao Zhu, and Athanasios Gavrielides. Degenerate quantum-beat laser: Lasing without inversion and inversion without lasing. *Phys. Rev. Lett.*, 62:2813–2816, Jun 1989. doi: 10.1103/PhysRevLett.62.2813. URL http://link.aps.org/doi/10.1103/PhysRevLett.62.2813.

[77] Ernst E. Fill, Marlan O. Scully, and Shi-Yao Zhu. Lasing without inversion via the lambda quantum-beat laser in the collision-dominated regime. *Optics Communications*, 77(1):36 – 40, 1990. ISSN 0030-4018. doi: http://dx.doi.org/10.1016/0030-4018(90)90456-4. URL http://www.sciencedirect.com/science/article/pii/0030401890904564.

[78] Olga Kocharovskaya and Paul Mandel. Amplification without inversion: The double-Λ scheme. *Phys. Rev. A*, 42:523–535, Jul 1990. doi: 10.1103/PhysRevA.42.523. URL http://link.aps.org/doi/10.1103/PhysRevA.42.523.

[79] G. S. Agarwal. Dressed-state lasers and masers. *Phys. Rev. A*, 42:686–688, Jul 1990. doi: 10.1103/PhysRevA.42.686. URL http://link.aps.org/doi/10.1103/PhysRevA.42.686.

[80] Olga Kocharovskaya. Amplification and lasing without inversion. *Physics Reports*, 219(3):175 – 190, 1992. ISSN 0370-1573. doi: http://dx.doi.org/10.1016/0370-1573(92)90135-M. URL http://www.sciencedirect.com/science/article/pii/037015739290135M.

[81] Marlan O. Scully. From lasers and masers to phaseonium and phasers. *Physics Reports*, 219(3):191 – 201, 1992. ISSN 0370-1573. doi: http://dx.doi.org/10.1016/

0370-1573(92)90136-N. URL http://www.sciencedirect.com/science/article/pii/037015739290136N.

[82] S. Ya. Kilin, Kishore T. Kapale, and Marlan O. Scully. Lasing without inversion: Counterintuitive population dynamics in the transient regime. *Phys. Rev. Lett.*, 100: 173601, Apr 2008. doi: 10.1103/PhysRevLett.100.173601. URL http://link.aps.org/doi/10.1103/PhysRevLett.100.173601.

[83] J Mompart and R Corbalán. Lasing without inversion. *Journal of Optics B: Quantum and Semiclassical Optics*, 2(3):R7, 2000. URL http://stacks.iop.org/1464-4266/2/i=3/a=201.

[84] Anatoly A Svidzinsky, Luqi Yuan, and Marlan O Scully. Transient lasing without inversion. *New Journal of Physics*, 15(5):053044, 2013. URL http://stacks.iop.org/1367-2630/15/i=5/a=053044.

[85] J Mompart, C Peters, and R Corbalán. Interpretation of transient v scheme amplification without inversion. *Quantum and Semiclassical Optics: Journal of the European Optical Society Part B*, 10(2):355, 1998. URL http://stacks.iop.org/1355-5111/10/i=2/a=009.

université PARIS-SACLAY | ÉCOLE DOCTORALE Ondes et Matière (EDOM)

Titre : Effet Laser dans Filaments Femtoseconde dans l'Air

Mots clefs : Effet laser, Filamentation, Plasma filamentaire, Molécule d'azote, L'air

Résumé : La filamentation laser femtoseconde dans l'air est un phénomène qui implique un grand nombre d'effets optiques non linéaires. L'effet laser dans les filaments a émergé comme un phénomène nouveau en 2011. Il a été activement étudié au cours des cinq dernières années, non seulement en raison de ses applications potentielles dans les techniques de télédétection mais aussi pour la riche physique à son origine. Cette thèse est consacrée principalement à l'étude de deux types d'effets laser à partir du plasma filamentaire généré dans l'air ou l'azote par des impulsions laser femtoseconde à 800 nm. Le premier est l'émission spontanée amplifiée des molécules d'azote neutre à la longueur d'onde de 337 nm, qui est bidirectionnelle et activée uniquement par des impulsions polarisées circulairement. Le mécanisme d'inversion de population est attribué aux collisions inélastiques électrons-molécules entre les électrons énergiques et les molécules d'azote neutre dans l?état fondamental. La caractérisation complète de l?impulsion laser à 337 nm émise vers l'avant et vers l'arrière est réalisée. En particulier, les mesures de profil temporel sont comparées à des simulations numériques basées sur l'équation de Maxwell-Bloch à une dimension, qui se révèlent être en bon accord.
Un autre type d'effet laser est lié aux ions azote N_2^+, émettant à 391 nm et 428 nm. Ce type d'effet laser est observé avec une pompe laser polarisée linéairement. Il est caractérisé systématiquement dans le domaine spatial, temporel et spectral. Les mesures du profil temporel prouvent que l'émission laser ionique est un mécanisme de superradiance. Un nouveau mécanisme, à savoir le processus d'excitation par recollision d'électrons, est proposé pour expliquer la distribution de population dans le niveau supérieur de la transition. Il est conforté par deux mesures expérimentales consistant en la dépendance de l?émission laser à 391 nm à l'ellipticité et la dépendance à longueur d'onde du laser de pompe. Des simulations numériques sont en bon accord avec les observations expérimentales.

Title : Lasing effect in Femtosecond Filaments in Air

Keywords : Lasing effect, Filamentation, Filamentary plasma, Nitrogen molecule, l'Air

Abstract : Femtosecond laser filamentation in air is a phenomenon that involves a rich family of nonlinear optic effects. Lasing effect from filaments has emerged as a new phenomenon in 2011. It has been actively studied in recent 5 years not only because of its potential applications in remote sensing but also the fruitful physics involved. This thesis is devoted to study of two types of lasing effects from filaments generated by 800 nm femtosecond laser pulses in air or nitrogen. The first is 337 nm bidirectional lasing of neutral nitrogen molecules, only enabled by circularly-polarized pulses. The population inversion mechanism is attributed to inelastic electron-molecule collisions between energetic free electrons and neutral nitrogen molecules. Full characterization of both forward and backward 337 nm lasing pulse is conducted. Particularly, the temporal profile measurements is compared to simulations based on one-dimensional Maxwell-Bloch equations, which turns out to be in good agreement.
Another type of lasing effect is related to excited nitrogen ion N_2^+, emitting at 391 nm and 428 nm wavelengths. This type of lasing effect can only be observed with linearly-polarized pump laser. It is systematically characterized in spatial, temporal and spectral domains. The temporal profile results prove that ionic lasing emission is fundamentally superradiance. A new mechanism, namely the electron recollision excitation process, is proposed for the achievement of population distribution in the upper level of transition. It is supported by two experimental measurements consisting of pump ellipticity dependence and pump wavelength dependence of 391 nm lasing intensity. Numerical simulations give good agreement with the experimental observation.

Université Paris-Saclay
Espace Technologique / Immeuble Discovery
Route de l'Orme aux Merisiers RD 128 / 91190 Saint-Aubin, France